NORTHWESTERN UNIVERSITY

E-740

THE D0 DETECTOR
FORWARD DRIFT CHAMBER
PERFORMANCE AND PHYSICS CAPABILITY
IN THE 1990 FNAL TESTBEAM RUN

A DISSERTATION

SUBMITTED TO THE GRADUATE SCHOOL
IN PARTIAL FULFILMENT OF THE REQUIREMENTS

for the degree

DOCTOR OF PHILOSOPHY

Field of Physics and Astronomy

By

Jeffrey W. Bantly

EVANSTON, ILLINOIS

June 1992

ABSTRACT

THE D0 DETECTOR FORWARD DRIFT CHAMBER PERFORMANCE AND PHYSICS CAPABILITY IN THE 1990 FNAL TESTBEAM RUN

Jeffrey W. Bantly

One of the D0 Detector's two Forward Drift Chambers was placed in a testbeam at the Fermi National Accelerator Laboratory in 1990. Two experiments were performed involving a series of data runs using a π^- beam interacting with targets from beryllium to lead, a wide range in atomic mass A. Calibration tests were performed with the chamber, measuring spatial resolution, tracking efficiency, double track resolution, and ioniziation. The testbeam setup allowed for precision tests in a controlled environment. These calibrations were used in the two different experiments. The first used the Forward Drift Chamber to measure charged track multiplicity as a function of s, the center of momentum energy, at 10, 50, and $150\,GeV/c$ incident beam momenta. The second examined single track data to obtain the target nucleus A dependence of the elastic diffraction nuclear slope parameter.

Acknowledgements

The DØ Collaboration has grown even larger during my five and a half years as a graduate student member. It has allowed me to meet and make friends with a broad cross section of the field of high energy physics. Many thanks to the many people who contributed to the process by which I obtained data, results, and a degree. Special thanks to those who made the NWA testbeams from 1987 to present work.

Particularly extensive help came from the collaborators closest to the FDC. Rob Avery organized the Northwestern team at NWA and made sure we had all the equipment we needed besides putting a lot of effort into the calibration analysis. Sue Blessing made the online analysis program work and spent her time trying to improve the track reconstruction software to the point where it really works even in the most complicated of circumstances. Srini Rajagopalan, my partner in crime, always kept the data acquisition and online calibration working despite the best efforts of others to change the rules of the game with system upgrades every couple of days. I'm glad to see that he's getting out at the same time as I am. Bob Tilden kept the computer cluster up and running with high efficiency despite our best attempts to tie up all the disk space, run tape drives into the ground, and generally treat the machines like rented cars.

I am very fortunate to have had two advisors who were involved in the experiment and my development from the first day I joined the group. Dave Buchholz and Bruno Gobbi are not afraid to be excellent teaching professors and dynamic researchers. Having attended classes by both, I only wished they were my instructors in some of the other classes I had to take. I would have learned a lot more. Bruno, an individual who can work 20 hours a day, has a broad experience in nuclear and high energy physics that is put to good use in his ability to design and build particle detection chambers seemingly overnight. I can only hope that some of his attention to detail and exacting standards has rubbed off on me. Dave, who managed to proofread two dissertations and do dozens of other things at once, couples an understanding of computers and electronics with the needs of the experiment much to our advantage. Despite the fact that he will always require a spellchecking program, his suggestions and help were always valuable be it physics or phrasing and available no matter how busy he was. I will surely miss working with these two high energy physicists.

Gerard Garino and Daniel Claes made life a lot more fun both during work and in the off hours. The birthday parties and comic books will be sorely missed. The NU Aikido Club was an excellent way to stay in shape and make many friends including Andre Moreau, Harvey Hensley, and Taku Tokuyasu who were also fellow graduate students. Domo arigato gozaimasu.

Fran and I will be celebrating our 9th anniversary this June just days before we both graduate with our doctoral degrees. I can not thank her enough for putting up with an absent-minded physicist type for these many years. Inspiration and support for all that I do comes from our life together.

Finally, I would like to thank my parents who have supported me in all of my endeavors with loving concern and warm affection.

Contents

List of Figures

List of Tables

1 The 1990 NWA Testbeam Run using the DØ Forward Drift Chamber

1.1 Introduction

This thesis describes the procedure and results of two physics studies performed using the DØ Forward Drift Chambers at the Fermi National Accelerator Laboratory during the 1990 Fixed Target Run. Charged track multiplicities are determined for beam momenta of $10\,GeV/c$, $50\,GeV/c$, and $150\,GeV/c$. The elastic diffraction scattering nuclear slope is determined for a series of targets nuclei of atomic mass A from beryllium ($A = 4$) to lead ($A = 207.2$).

1.2 Experimental Motivation

The DØ Detector is a colliding beam experiment (E-740) located at the DØ interaction point of the Fermilab Tevatron. The detector and its main goals have been described in detail elsewhere [1] [2] [3] [4] [5] [6] so only a summary is given here. The project will study the physics of p-$\bar{p}$ interactions at $\sqrt{s} = 1.8\,TeV$. Towards this goal, its main features are excellent identification and measurement of electrons and muons, good measurement of quark-gluon jets at large p_T through highly-segmented, good energy resolution calorimetry, and a controlled measurement of missing transverse energy ($\not{E}_T$). Typically new objects and phenomena have sizable branching ratios into states with leptons and jets while the dominating QCD backgrounds have small leptonic branching ratios. Better capabilities at studying quark-gluon jets allow closer approximation to the underlying physics processes than emphasis on the subsequent particles from the hadronization process. The DØ detector has three major detector components. The central feature is hermetic, thick, radiation-hard calorimetry which has unit gain, a small inner radius, and is based on detection of ionization in liquid argon [7]. The muon detection system has thick magnetized iron absorbers for

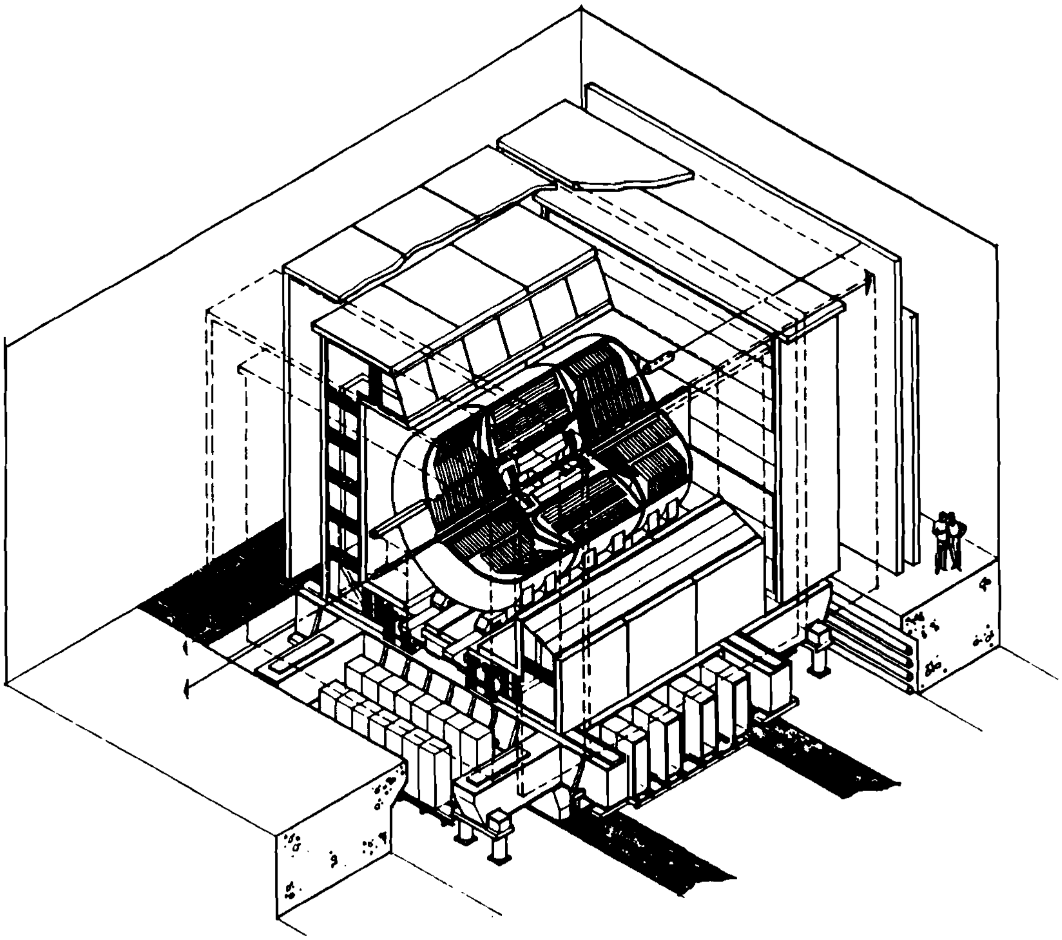

Figure 1: The DØ Experiment

momentum measurement and reduction of hadron punchthrough backgrounds [8]. The innermost volume contains a non-magnetic tracking volume within an $r = 75\,cm$ with good spatial resolution and a suppression of backgrounds to electrons [9]. This is achieved by use of minimal material to aid gamma conversions and the presence of a transition radiation detector in the central region. The overall DØ design has almost complete 4π coverage by all three sub-systems where the only gaps are the beampipes and the calorimeter supports that block some muon coverage.

The DØ Forward Drift Chambers (FDCs) [10] are two sets of gas drift chambers whose task will be to perform charge particle tracking in the high eta or 'forward' regions of the DØ Detector.

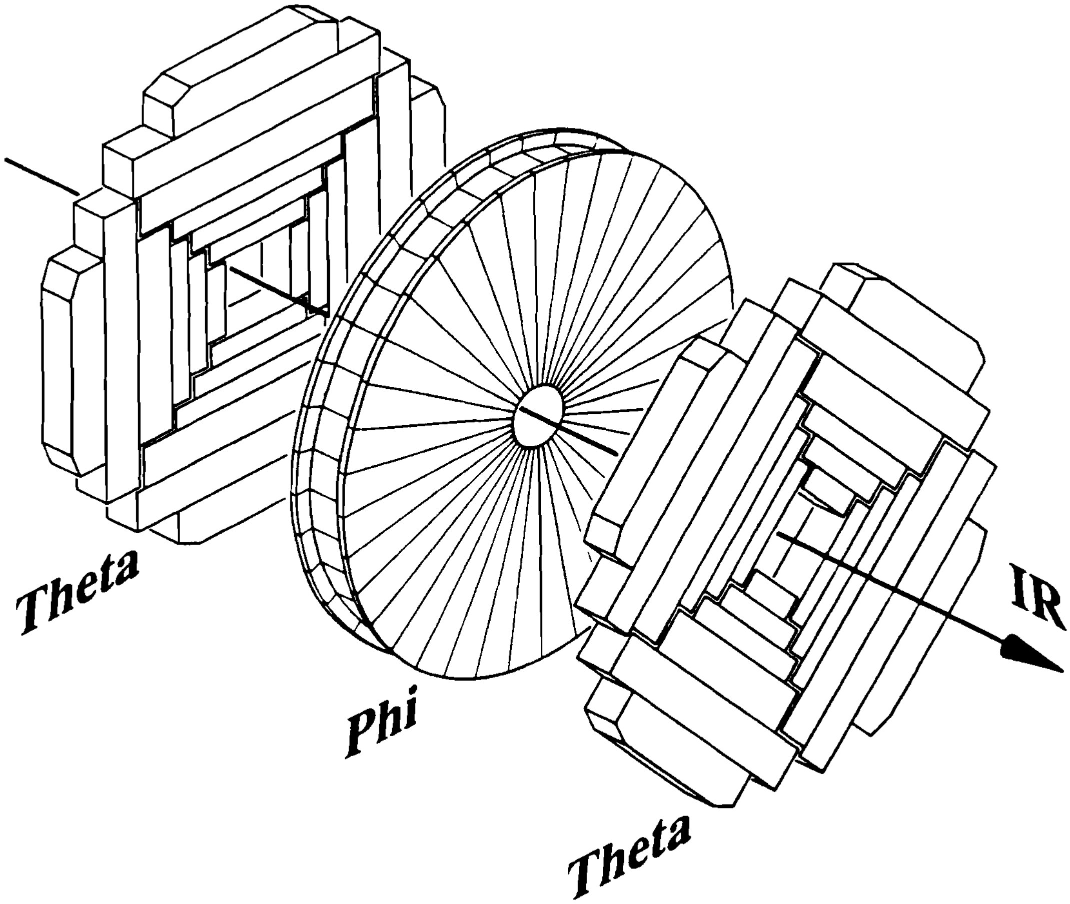

Figure 2: One D0 Forward Drift Chamber

One chamber is positioned at each end the D0 Central Tracking volume which itself rests inside the Central Calorimeter.

Drift chambers use the drift time and quantity of ionization electrons in a gas to measure spatial position and energy loss by ionizing (charged) particles. An important goal of the experiment was to measure the chamber performance in four categories. Spatial resolution, tracking efficiency, double track resolution, and ionization are these important qualities. This thesis will not directly address the measurements of ionization as that will be covered elsewhere [11]. These four basic results were the essential calibration for the two studies presented here.

A wide variety of data-taking runs were taken to be used for calibration. Spatial resolution and efficiency were measured using single track data runs with a primarily pion beam passing through the chamber as it was aligned perpendicular to the beam and at various angles to the beam. Also, a series of data runs were taken at different values of the drift field voltage and the sense wire voltage. Results presented here include uniformity of drift velocity with track angle and drift distance. Hit resolution and hitfinding efficiency were determined versus track angle and drift distance. Double track resolution was determined using simple two hit resolutions and a set of photon conversion runs in which a number of e^+e^- pairs were measured.

The DØ experiment is a colliding beam experiment and will create a multi-track environment in which the FDCs have to operate. For the purposes of this study, a fixed target beamline environment was necessary. The experimental area used was located at the end of the Neutrino West beamline. During normal operations, beams of mainly pions and electrons of momenta ranging from 10 GeV/c to 150 GeV/c were delivered. One DØ Forward Drift Chamber was placed in the beam for the purposes of calibration and studying the chamber's capabilities. In order to simulate this environment, targets were placed in the NWA beamline just upstream of the FDC. The FDC was rotated in such a way that the particles emerging from collisions in the target would enter the chamber at an angle approximating those coming from the DØ interaction region. Thus, multi-track events under realistic laboratory conditions were generated and could be analyzed. A range of targets from Be to Pb was used at beam momenta of 10 GeV/c, 50 GeV/c, and 150 GeV/c. These runs were used in two different ways. An analysis of multi-track events looked at charged track multiplicities at each beam momentum. The results follow the expected trend and compare well with data from previous experiments. An analysis of single-track events examined the diffractive scattering portion of the elastic cross section. The nuclear slope parameter was determined for each target and followed the expected trend of $A^{2/3}$ where A is the atomic mass of the target nucleus.

A discussion of the basic design and configuration of the Forward Drift Chambers is followed by a detailed discussion of the experimental setup, data acquisition, and readout electronics. A summary of event reconstruction and chamber calibration studies is given in preparation for their use in the two analyses of the target data runs.

2 The DØ Forward Drift Chamber in NWA

The basic requirements of a good drift tracking chamber are collecting as many ionizing electrons in as short a time interval as possible while disturbing the original particles as little as possible.

2.1 DØ Forward Drift Chamber

The DØ Forward Drift Chambers (FDCs) provide charged particle tracking coverage over a θ range of 27° down to 5° with respect to both emerging beams ($1.4 < \eta < 3.1$). There are two identical sets of chambers; one set located at each end of the Central Tracking barrel. Their radius is somewhat less than the large angle tracking chambers to allow the myriad cables to pass out from the interior chambers ($r = 65cm$ vs $r = 75cm$). Each FDC half consists of three separate layers: one Φ layer whose sense wires are arranged like spokes on a wagon wheel measuring the ϕ coordinate sandwiched between two Θ layers whose sense wires are positioned to measure (approximately) the θ coordinate. The angle θ is the angle of emission or scatter from the beam direction which lies along the z coordinate axis. The angle ϕ measures the angle about the z coordinate axis.

2.1.1 Phi Chamber

The Φ layers, one at each end, are single chambers with 36 sectors over the full azimuth and 16 anode sense wires along the z-coordinate in each sector. The sense wires are centered in each sector and thus electrons can drift in from both sides. Two $66.04\,cm$ radius, $1.07\,cm$ thick Kevlar-coated Nomex honeycomb supports sandwich the 36 sectors between them. An aluminum inner hub and an outer wall enclose the gas volume at radii of $11\,cm$ and $61.29\,cm$ with a thickness between the honeycomb supports of $14.06\,cm$.

The Φ chamber electrostatics are determined by single grounded guard wires located between and alternating with the anode sense wires. The guard wires lie on a plane bisecting each sec-

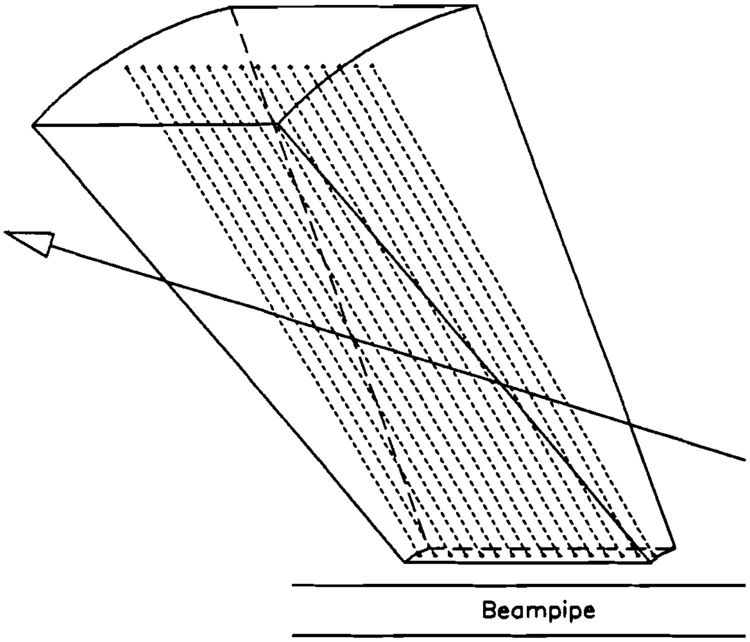

Figure 3: Typical Φ Sector

tor. The sense wires are staggered perpendicular to the guard wire plane by alternately $+200\,\mu m$ then $-200\,\mu m$ for use in resolving the left-right ambiguity. A left-right ambiguity occurs when ions can drift in towards the wires from both the left and the right. In order to determine which side the ions came from, adjacent wires are staggered in the drift direction causing the ions to arrive at the near plane of wires earlier than the alternate plane of wires. During event reconstruction, the wire signals can be shifted to re-align the hits. The hits will line up on their original side of the drift sector but will be double staggered on the wrong side. A simple line fit would yield a much larger error for the wrong side fit and would allow a cut on the fit to correctly resolve the left-right ambiguity. The wires are mounted on pins that pass through the inner hub wall and the outer wall. The electronics for readout and wire voltages or grounds are located outside the outer wall. The inter-sector septums are $0.005\,in$ thick G-10 etched with $0.001\,in$ thick aluminum strips to act as cathodes for the field voltage. The front and back honeycomb supports have a Kapton layer with copper traces. G-10 boards are mounted just inside the outer wall to distribute the field voltage to the copper traces on the Kapton layers. These combine to surround each sector volume with field-shaping electrodes which provide a uniform field for ion drift over the entire radius of the volume. The field voltage is set high enough to be well into the saturated gas drift velocity region (see Section 4.4.1).

2.1.2 Theta Chamber

The Θ layers, two at each end, each consist of four mechanically separate quadrants. Each Θ quadrant contains six rectangular sectors at increasing radius. The quadrants come in two varieties, type A and type B. The type A quadrants have somewhat longer sectors than the type B quadrants but the sector widths are the same for both types. This was done in order to assemble the quadrants together as tightly as possible to leave a minimum of dead space. This jigsaw puzzle-like method leaves only a $0.125\,in$ clearance between quadrants. Each sector in a quadrant has a longer length than its inner neighboring sector except for the outermost sector which is shortened with slanted outer edges because of the limiting radius. See Figure 2.

Each sector contains 8 anode sense wires along the z-coordinate. The inner three sectors have only half the width ($5.3\,cm$) in the radial direction and are built with their sense wires near to one wall thus allowing electrons to drift in only one direction across the sector volume. This removes any left-right ambiguity for these inner sectors. The outer three sectors are full width ($10.6\,cm$) and are built with their sense wires along the centerline of the chamber. Each sector has a delay line embedded in the sector back which is positioned towards the Φ chamber for all sectors. The delay lines propagate signals induced from the nearest neighboring sense wire which has been shifted from a centered position to a position closer to the delay line to enhance the induced signal. Each

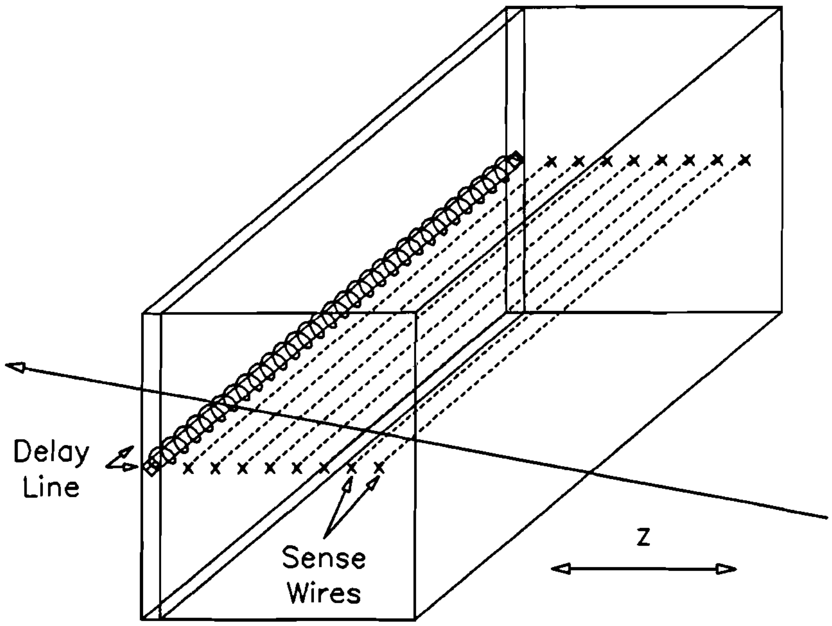

Figure 4: Typical Full-Width Θ Sector

inductive delay line is made by winding a coil on a carbon fiber epoxy core. Propagation velocities are $\approx 2.35\,mm/ns$ along the coil and have a ratio of delay time to risetime of about 32:1.

The Θ chamber electrostatics are determined by single grounded guard wires in the half-width sectors and by two grounded guard wires in the full-width sectors located between each anode sense wire. The guard wires are located $4\,mm$ away from the centerline of the sector, one on each side of the centerline for the full-width sectors. There is an additional guard wire located on the centerline plane between sense wire 0 and sense wire 1 to additionally isolate sense wire 0 and provide maximum signal height on the delay line. The sense wires in the full-width sectors are staggered perpendicular to the centerline plane by alternately $+200\,\mu m$ then $-200\,\mu m$ for use in resolving the left-right ambiguity. The electronics to readout and set the voltages and grounds for the wires and delay lines are located on the outer face of each quadrant facing away from the

Φ chamber when mounted. The intersector side walls are 0.008 inch aluminum foil on Nomex honeycomb and act as cathodes. The walls adjacent to the sense wire planes in the half-width sectors are grounded. The front and back surfaces are Kevlar-coated Rohacell with copper traces on a Kapton sheet forming the field-shaping electrodes. This combination provides a uniform drift field for the ions.

2.1.3 Full Assembly

When each Forward Drift Chamber half is assembled, each of the four Θ quadrants comprising a Θ layer are attached by six bolts and three alignment pins to the Φ chamber. The inner Θ layer is rotated 45° with respect to the outer Θ layer. Thus, the outer Θ sense wires are parallel to the x- and y-coordinate axes while the inner Θ sense wires are at 45° degrees to the x- and y-coordinate axes. This rotation minimizes the overlap of any dead regions and improves the accuracy of a fit to a track.

The FDC is operated with a gas mix composed of Ar(93%)CH_4(4%)CO_2(3%). At typical operating field voltages, the drift field is approximately $943\,V/cm$ in the drift volumes with a drift velocity of about $35\,\mu m/ns$. The standard voltage on each anode sense wire is $1.50\,kV$ but the sense wire closest to each delay line has an elevated standard setting of $1.60\,kV$ to induce larger pulses on the delay lines.

3 The NWA Testbeam Line and Test Area Setup

The NWA testbeam area is located at the end of the FNAL Fixed Target Neutrino West beamline. Its beamline is capable of delivering beams of pions and/or electrons at a controlled momentum which could be set from about $10\,GeV/c$ up to $150\,GeV/c$ and still yield reasonable particle rate. The Forward Drift Chamber was placed directly in the beamline in the NWA testbeam experimental area. A subset of the full D0 data acquisition system was used to read out the chamber and perform electronics calibrations. Details of the beamline and the experimental setup will be discussed below.

3.1 NWA Beamline Characteristics

The NW beamline starts at the NW1W dipole where 800 GeV/c primary protons are extracted from the Tevatron and directed towards an aluminum production target in the NW3 enclosure [12]. See Figure 5. The maximum beam rate allowed on the target is 5×10^{12} protons per 20 second spill to limit radiation in the area and thermal damage to the target. The secondary beamline mainly consists of four horizontal bend plane magnets formed by the NW4W, NW6E, NW7W, and NW9E dipole magnets. The beam bends west at NW4 and NW7 and east at NW6 and NW9. There are vertical trim magnets in enclosures NW4, NW6, and NW9 to steer the beam in the vertical plane. The quadrupole focussing elements in NW4 and NW8 focus the beam just before NW7 and NWA. Additional elements in the beamline are the sweeper magnet NW4S, horizontal and vertical collimators NW4CH, NW4CV, NW6CH, NW6CV, and target wheels NW4PB, NW6PB, NW7PB which have lead plates of different thicknesses mounted in them. A hadron and an electron mode of operation are available. The hadron mode is achieved by inserting the thin lead plates of the NW6PB and NW7PB wheels into the beam. Since lead has an interaction length of $194\,gm/cm^2$ and a radiation length of only $6.37\,gm/cm^2$, electrons are preferentially scattered by these plates thus greatly diminishing their beam content.

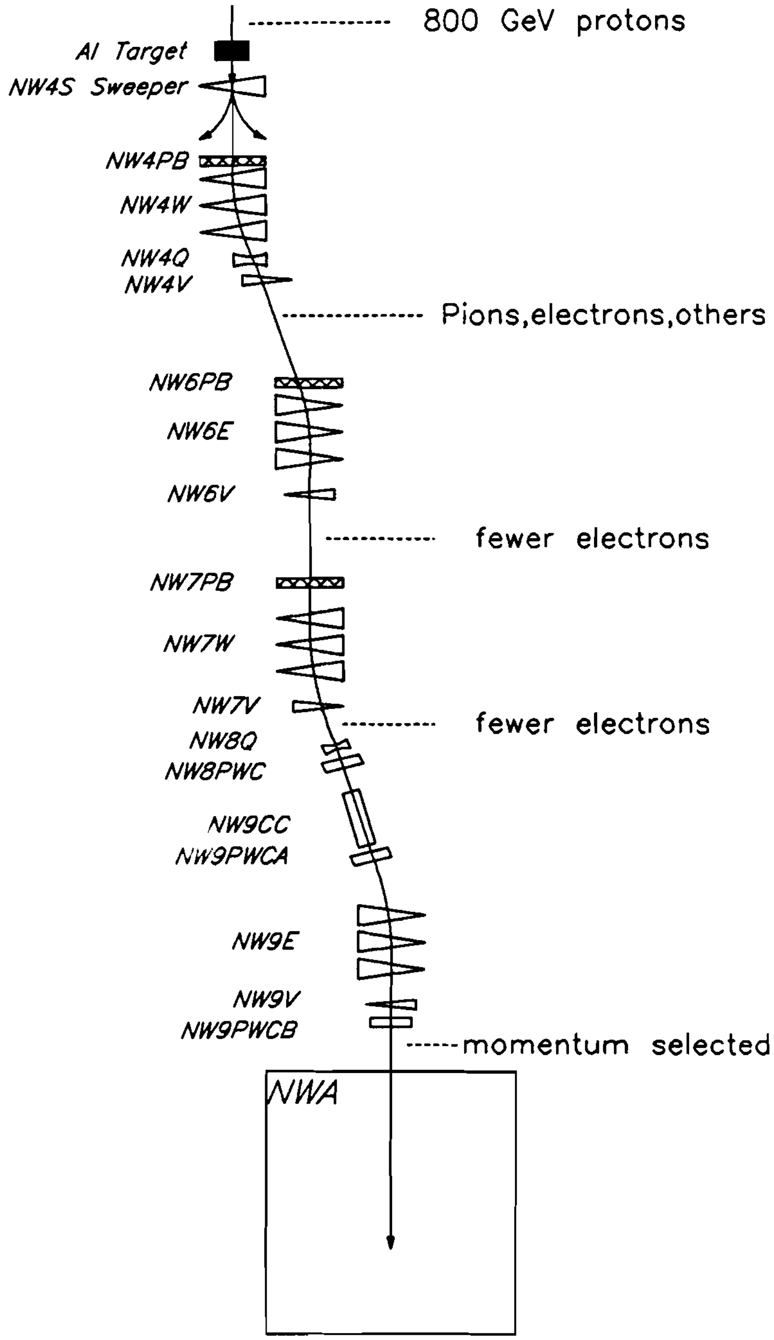

Figure 5: The NWA Beamline in 1990

However, the pion content is also reduced by a factor of 20. Below a momentum of $25\,GeV/c$, only NW7PB was inserted so as not to overly reduce the pion intensity which is already falling with energy.

The electron mode is achieved by turning on the sweeper magnet NW4S and sweeping all charged particles out of the secondary beam leaving only neutrals, principally photons, in the beam. The lead target NW4PB was inserted into the beam which would convert photons in the beam into electron-positron pairs. Only the electrons survive transport to the test area as the positrons are swept off the beam path by subsequent magnets. The NW6PB and NW7PB lead plates are removed from the beam path in this mode.

The beamline transport was controlled by the EPICURE system, a user-interactive beamline element control program. This system allowed beamline users to adjust magnet currents, zero scalars, adjust the Čerenkov counter gas pressure, and output readings taken by the intrumentation for the portion of the beamline serving the users' area. Details of the EPICURE system are available from the Fermilab Accelerator Division.

3.2 NWA Beamline Instrumentation

The NWA beamline was instrumented to measure beam rates and position [12] [13]. Several scintillators were placed in the beam at various points to measure beam intensity along its path. SWICs (segmented wire ionization chambers) were used to monitor the beam profile. Two Helium Čerenkov counters, one between NW8 and NW9 and the other between NW9 and NWA, were used to measure the particle content of the beam. PWCs (proportional wire chambers) [14] were also placed just after NW8, before and after NW9, and before and after the FDC in NWA. In NWA, there were three scintillation counters whose coincidence became the primary trigger. There was a hole veto scintillation counter to reject particles in a central $2\,in$ by $4\,in$ area. This primary coincidence was used to measure the rates in NWA. Additional scintillator counters were used in conjunction with the primary coincidence to form specialized triggers. Several of the beamline instruments were entered into the EPICURE database for purposes of monitoring the beam. In addition, EPICURE-based programs were written to read out some of the information during beam spills and this information was written to disk.

Beam momentum measurement was accomplished by measuring the magnetic field of the last bending magnet NW9E by insertion of a Hall probe. PWC stations located upstream and downstream of the magnet provided tracking. A short calculation yielded the beam momentum for a particular voltage setting of the magnet.

$$p(GeV/c) = \frac{B \cdot L}{1313.24 \cdot \phi} \tag{1}$$

where

B is the NW9E magnetic field in kilogauss,

L is the magnet length in inches, and

ϕ is the nominal bend angle of the beam in radians which is 28.68 mr for NW9E.

A study of the beam momentum was made [12] to calibrate the Hall probe mounted in the NW9E magnet and to measure the beam momentum spread. It was found that for a typical gaussian beam with a sigma of 1 in in horizontal profile, the momentum profile is a gaussian with $\sigma(p)/p = 1.8\%$. A narrow beam at the entrance to the NW9E magnet should have a direct correlation to the beam momentum as a function of horizontal position at the FDC. However, this is smeared by the effects of angular divergence of the beam before entering the magnet.

3.3 Beam Particle Rates and Content

Particle rates at NWA were dependent on beam momentum and upstream beamline limitations. The maximum proton rate allowed on the primary target as stated above is 5 x 10^{12}. Pion yields [12] at NWA per incident primary proton were 9 x 10^{-6} at pion momentum of $150\,GeV/c$, 3 x 10^{-6} at $50\,GeV/c$, and down to 8 x 10^{-8} at $10\,GeV/c$. Rates are down by a factor of 20 at 150 and $50\,GeV/c$ with the electron scatterers in the beamline. At $10\,GeV/c$, the pion rate is down by over a factor of 200.

3.4 Forward Drift Chamber in the Beam

3.4.1 Rail Mount Inline Position

A rail mounted frame was available in NWA for horizontal and vertical movement of the FDC. All motion was perpendicular to the beam direction. When mounted in the frame, the FDC could be moved by remote control and the actual distance moved was measured by a pair of spring tensioned multiturn potentiometers with an accuracy of $\approx$ 1%. This setup was used for straight through track studies such as scans along the length of various sectors in the chamber as well as for the high statistics data runs including the half-sector and full-sector data runs.

3.4.2 Off Rail Angled Positions

The frame could also be dismounted and taken off the rail lines. This allowed the angling of the FDC with respect to the beamline. Data runs were taken to study single tracks through the chamber at angles ranging from 0° to 35°. For the multiple-track target data runs, the chamber was placed at $\approx$ 20° to the beamline and positioned to maximize the cross-section of charged particles passing through the sections of the FDC connected to the readout electronics.

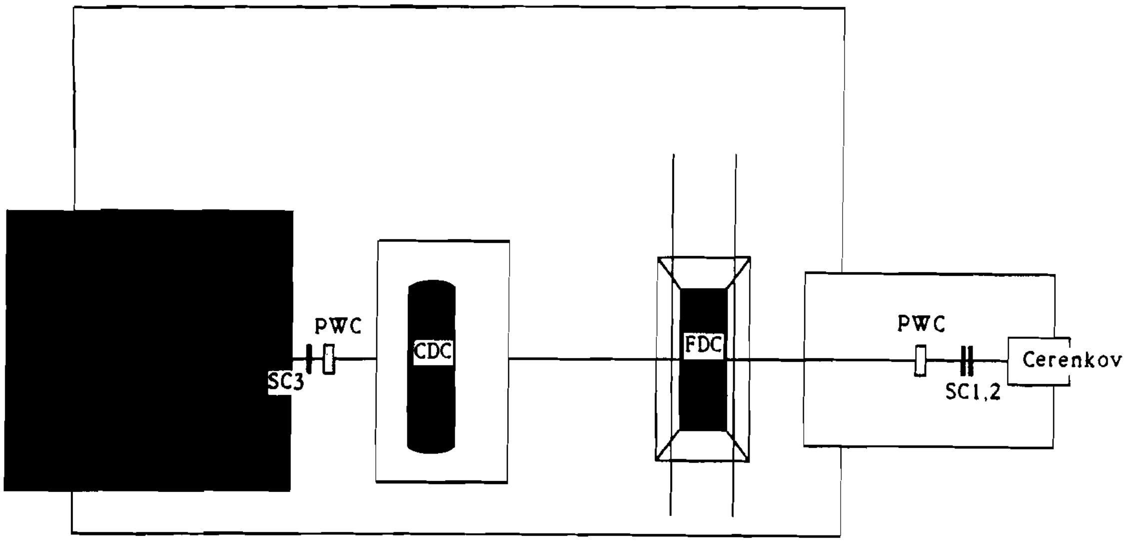

Figure 6: FDC on Rail Mount Inline Setup

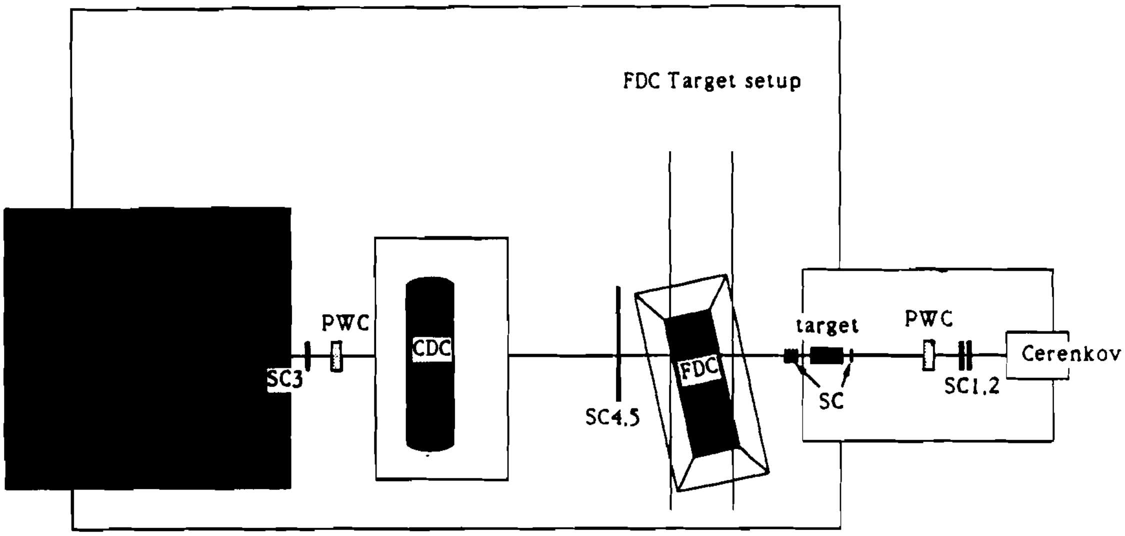

Figure 7: FDC Off Rail Angled Position Setup

3.5 Upstream Beamline Instrumentation

3.5.1 PWCs

There were nine planes of proportional wire chambers (PWCs) mounted along the beamline. Each plane measured either vertical(Y) or horizontal(X) coordinates. There was one X chamber downstream of the NW8 magnet, one X and one Y chamber pair both upstream and downstream of the NW9 magnet. These chambers had 64 wires with $1\,mm$ wire spacing. There were X and Y pairs of PWCs at both the upstream end of NWA and downstream of the FDC setup area. These chambers had 96 wires spaced $1\,mm$ apart. The chambers were all centered on the nominal beamline position both horizontally and vertically. The PWCs were read out for each data event and the information included as each event was written to storage. The total path length along the beam covered by the PWCs was $124.63\,m$. The two pairs of PWCs located in NWA were separated by $6.94\,m$. A software package was provided that performed track reconstruction using the PWCs [15].

The beam profile SWICs were PWCs read out by integrating over many particles generating a profile histogram. These were useful to center the beam in the magnets along the line before reaching the momentum selecting NW9 magnets.

3.5.2 Čerenkovs

There were two Čerenkov detectors in the NWA beamline. Helium filled both the $70m$ counter in NW9 and the $30m$ counter in NWA. Standard run conditions had the Čerenkov pressure settings just below the pion threshold to maximize the efficiently of tagging electrons in the beam [13]. These counters had not been calibrated in time for the target runs. However, they were properly set for the photon conversion runs and were used to tag electrons in the original beam and veto electrons still remaining in the photon beam.

3.6 Data Acquisition and Readout

The data acquisition and readout was a subset of the system to be used at the D0 experiment. Arrays of scintillators provided the triggers for individual data events and set in motion the readout electronics. Signals from the chambers were shaped, digitized, and stored (eventually) on magnetic tape. Many of the results in subsequent chapters are measurements of the capabilities of the electronics as well as being measurements of the chambers' capabilities.

3.6.1 Level 1 Triggers

The triggers used to start the data acquisition and readout depended upon arrays of scintillators connected to phototubes whose signals were passed through discriminators. The basic trigger consisted of signals from three large scintillators and no signal from a hole veto counter. The SC1 and SC2 scintillators were located at the entry to the NWA experimental area and the SC6 hole veto counter was positioned after the first NWA PWC. The SC3 scintillator was located after the FDC in the beamline. A charged particle centrally located in the beam path would pass through the SC1, SC2, and SC3 scintillators while passing through the hole in the veto counter. A table of scintillator sizes are listed in Table 1 and their layout is shown in Figure 8. For the target trigger used in data runs with a target placed into the beam, two additional sets of scintillators were placed into the beam path. One set consisted of five small scintillators AND'ed together. One counter was placed before the target, a Forward scintillator, and four were placed after the target labelled Up, Down, East, and West. The directions correspond to the position of their attached phototubes. These scintillators defined the beam path more narrowly so that a charged particle passing through the scintillators would necessarily pass through the targets placed in between them. The second set, SC4 and SC5, were larger scintillators placed one above and one below the beam path centerline. These counters cover a much wider area than the beam size so as to include any scattered particles.

The photon beam trigger consisted of the SC1 and SC2 counters used as a veto, the Up, Down, East, and West counters used as a tag, and the SC4 scintillator counter as a tag before the Pb glass calorimeter.

The trigger logic for the basic trigger was

$$SC1 \cdot SC2 \cdot SC3 \cdot \overline{SC6} \tag{2}$$

This trigger was used for the chamber diagnostic runs such as drift time versus drift distance. The target trigger logic was

$$(SC1 \cdot SC2) \cdot [F \cdot (U \cdot D \cdot E \cdot W) \cdot (SC4 \cdot SC5)] \tag{3}$$

This trigger required the beam particle to pass through the target and then through the FDC. The discriminators attached to the Up, Down, East, and West scintillators had thresshold levels set higher than the other counters' $30mV$ level. Set at about $140mV$, this level lowered the number of non-interacting beam particles that were accepted. The photon beam trigger logic was

$$(\overline{SC1 \cdot SC2}) \cdot (U \cdot D \cdot E \cdot W) \cdot Calor \tag{4}$$

This required a neutral particle before the target, hopefully a photon, and at least one charged particle after the target entering the lead glass. Once the trigger logic is satisfied, a signal is sent to the trigger framework which in turn starts the event readout sequence. A delayed trigger signal is also inserted directly into one of the FADC channels to become the timing pulse.

3.6.2 Preamplifiers

The preamplifiers are based on the Fujitsu MB43458 [16] quad common base amplifier in a surface mount package. These are mounted in groups of eight channels together with input protection circuitry on a hybrid circuit that fits into a regular 28-pin DIP socket. The hybrid also contains

	Sizes	
Scintillator	HxW(in)	Thickness(in)
SC1,SC2,SC3	4x4	0.25
SC6 veto hole	2x4	0.25
Forward	1.5x1.5	0.03125
Up,Down,East,West	1.75x1.75	0.03125
SC4,SC5	10x20	0.25
Calor	2x2	0.125

Table 1: Scintillator Counter Sizes

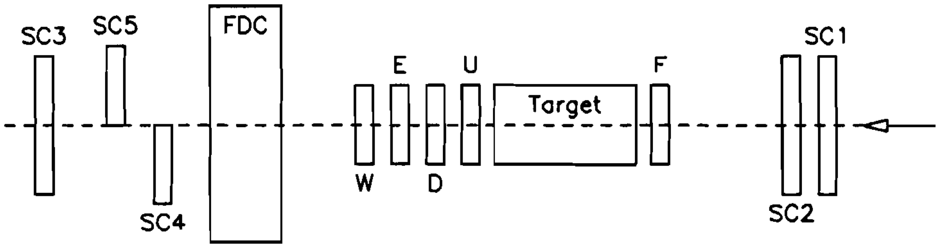

Figure 8: The Target Trigger Components - Side View

small coupling capacitors to inject test charges onto each channel which can be used to test the integrity of the entire electronics chain.

3.6.3 Shaper Boards

The signals from the preamplifiers are carried over 65 *nsec* of coaxial cables to the shaper circuit boards [17]. These boards contain a video amplifier, a two zero-three pole shaping circuit, and a cable compensation driving circuit. The gain and shaping components are mounted on separate printed circuit boards for each channel so that the shaping can be easily modified to accomodate the different types of channels (sense wire and delay line) being read out.

3.6.4 Flash ADC Boards

The shaped signal pulses are carried to the digitizing circuitry by $238.4\,nsec$ of coaxial cables. The digitizers are Sony 8-bit flash analog to digital converters (FADC) operated at $106\,MHz$. After passing through a bilinear amplifying network, each channel was sampled and digitized 512 times per data event, once every $9.434\,nsec$. The data for each channel is passed through a zero-suppression circuit before being buffered for readout.

Bilinear Response A bilinear amplifying network with programmable gain precedes the FADC to extend the effective range of the digitizers from 8 bits to 9.5 bits [18]. A one-to-one map was later used to reset the digitized values to their equivalent pre-conversion digitized values.

Zero-suppression The size of the data from one FADC channel's output is 512 samples per event. With 1056 channels per FDC half, the size of the data would be very large ($\approx 500\,MBytes$) and readout time would be too long. To reduce the data size to acceptable levels, the digitizer also contains a Fermilab designed zero suppression chip and memory to sparsify the data in real time as it is collected [19]. The zero-suppression chip has programmable thresholds which can be used to look for certain patterns in the digitized signal and the first difference of the digitized signal. The algorithm recognizes the leading edge (LE) and the trailing edge (TE) of the pulse cluster by using a combination of slopes and/or thresholds as shown below. B_i is the FADC value at bin i and D_i is the difference $B_i - B_{i-1}$.

$$C1 = (B_{i-2} > T1) \cdot (B_{i-1} > T1) \cdot (B_i > T1)$$

$$C2 = (B_{i-2} > T2) \cdot (B_{i-1} > T2) \cdot (B_i > T2)$$

$$C3 = (B_{i-2} < T3) \cdot (B_{i-1} < T3) \cdot (B_i < T3)$$

$$C4 = (B_{i-2} < T4) \cdot (B_{i-1} < T4) \cdot (B_i < T4)$$

$$C5 = (D_{i-1} > S1) \cdot (D_i > S1)$$

$$C6 = (S2 < D_{i-1} < S3) \cdot (S2 < D_i < S3)$$

$$LE = C1 \cdot C5 + C2$$

$$TE = C3 \cdot C6 + C4$$

Tl, T2, T3, T4, Sl, S2 and S3 are the zero-suppression parameters and are preset during the initialization for each data-taking run. Successful recognition causes the data to be retained until a second set of patterns are found that turns off retention. An example of non-zero-suppressed data and zero-suppressed data are shown in Figures 9 and 10.

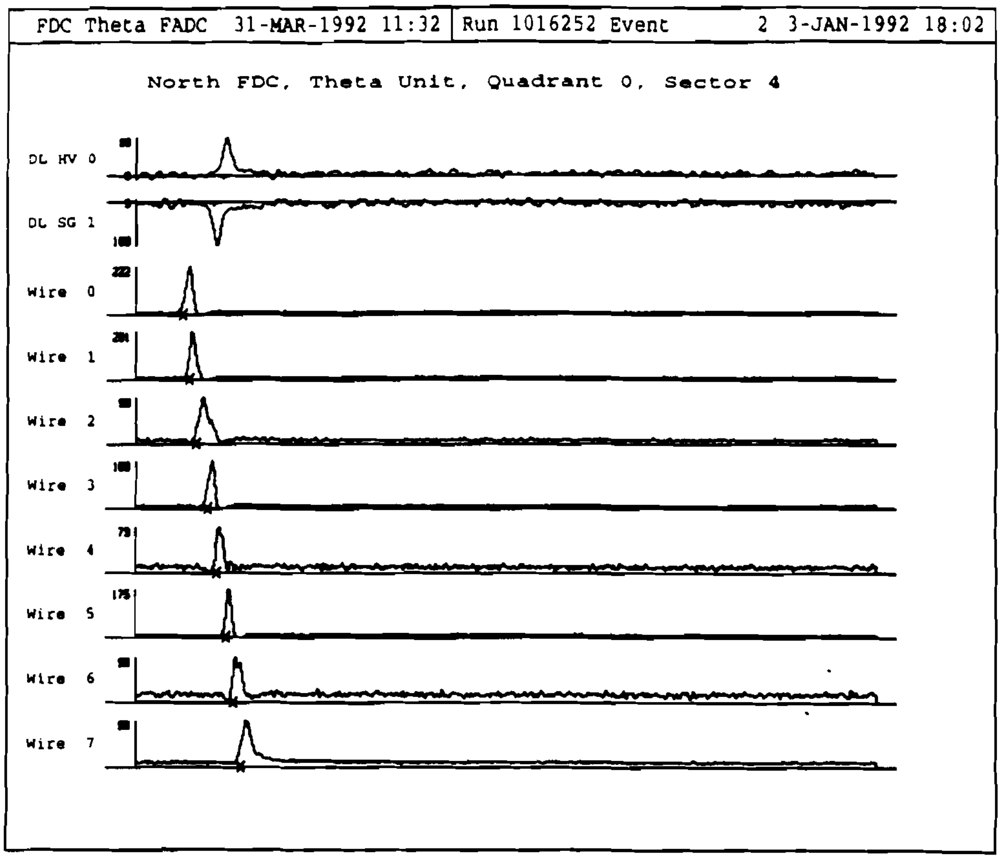

Figure 9: Sample Non-zero-suppressed Flash ADC Output

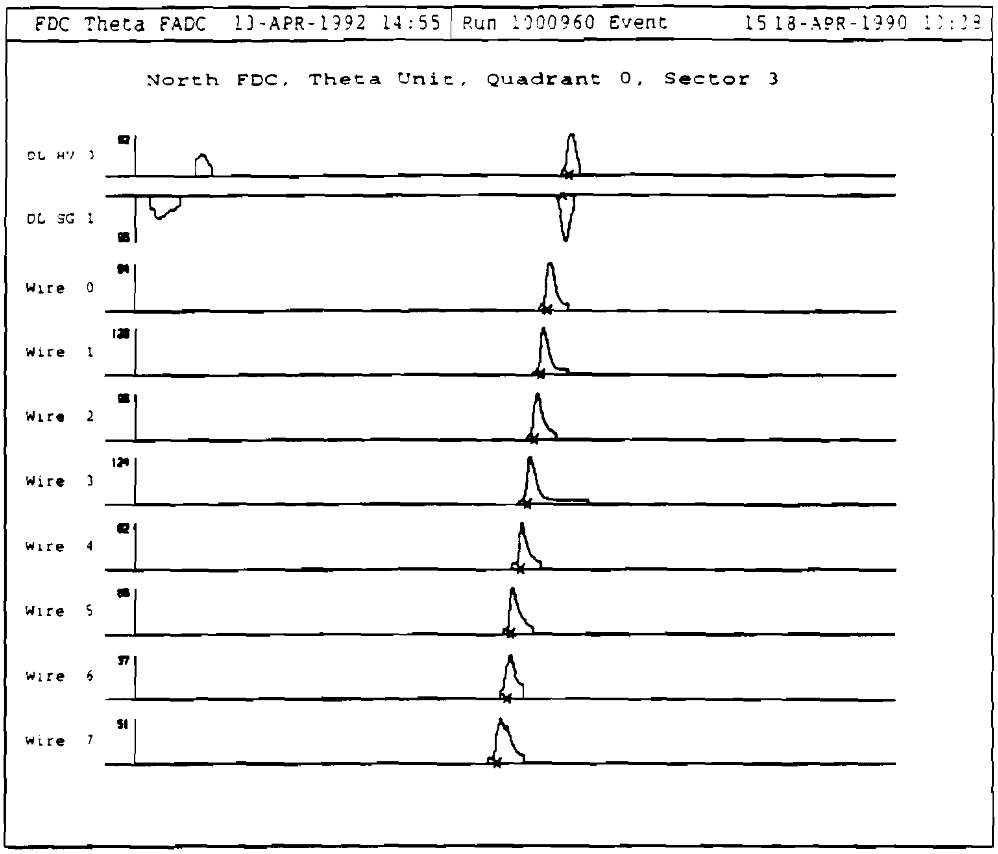

Figure 10: Sample Zero-suppresed Flash ADC Output

3.6.5 Level 2

The Level 2 system read out the crates of FADCs and CAMAC crates and assembled the data into a Zebra-structured event which could be passed on to storage devices of hard disks and magnetic tapes.

3.6.6 FDC Timing Pulse

The Level 1 trigger was passed through a delaying circuit and fed directly into one of the readout channels at its shaping circuit board. This was used as a timing pulse for determining the time the trigger particles traversed the drift chamber. The FADCs were set to start digitizing at regular clock intervals of $5\,\mu secs$. A trigger was accepted if it landed at least $150 nsec$ after the start digitize but not more than $2.5\,\mu sec$ after the start digitize. This guaranteed that all signals from the shortest to the longest drift times, roughly $0\,nsec$ to $1600\,nsec$, would be recorded in the available 512 FADC bins in each channel. The timing pulse marked the time of the start of an event. Because of the above method of starting the FADCs digitizing, a triggered event did not start at the first FADC time bin but somewhere between the $16th$ bin and the $280th$ bin. The event start timing pulse, or t_0, was a short spike whose time could be determined to within $\approx\ 2\,ns$. The FADCs were designed for use in a colliding beam environment where the beam crossing time is known in advance. The start digitization had to be adapted to this situation where the time of arrival of a particle is not known ahead of its arrival.

3.7 Electronics Calibration

3.7.1 CALIB

CALIB was a user-oriented computer program that would make measurements of the electronics readout chain in three areas. Background noise level and variation were measured to determine the pedestal of the FADC output signal and the variation of signals caused by noise. The time for a signal to pass through the entire readout chain for each channel could be measured with respect to each other and proper offsets to realign the signals in time were stored. Thirdly, the electronic gain could be measured by injecting a known charge into the preamp and measuring the size of the output pulse in the FADC.

3.7.2 Pedestals

Pedestal measurements were obtained by collecting 150 data events through the data acquisition. These events were non-zero-suppressed and the average digitized signal level and sigma about that level was histogramed for each channel in each event. The means of the pedestal, t_0, and gain distributions were stored by channel in a permanent, time-stamped database. These levels were available for both online and offline data analysis of subsequent data runs.

3.7.3 T-Zeros

The different path lengths of the electronics readout chain required time offsets to be used to resynchronize each electronics readout channel with the trigger time. Data runs were taken making use of the pulsers that will insert a measured amount of charge into each preamp channel. Insertion was simultaneous across all the tested channels. Analysis of the output signal delay provided an offset time (t_0) for each channel.

3.7.4 Electronic Gain

The electronic gain for each channel was obtained by using the pulser to insert a known amount of charge into each preamp and histogramming the area under the output pulse that was above the pedestal level. The mean of the pulse area distribution divided by the original input charge provided an electronic gain.

The gain set on a chamber's electronics is a compromise determined by four goals: what is to be measured, the counting rate, the limits of the electronics, and long term stable operation. Whereas precision position measurement prefer high gas gain like 10^5, the dE/dx measurement requires proportional operation and long lifetimes prefer lower gas gains. For the FDC, a determination of the electronic gain and gas gain was made [20]. The electronic gains in both the shaper boards and the FADC boards were adjusted to levels that allowed the individual pulses from collected charge from track ionization to be large but not saturate the electronics. The measurements of the two gains is done by comparing the amount of charge put into the readout system versus the corresponding FADC pulse area. The electronic gain measurement was made by injecting a known charge directly into the preamp and histogramming the area under the output pulse above pedestal in the corresponding FADC channel. The electronic gain was calculated using

$$Q_{inject} \cdot Gain_{elect} = Area(fadc\ counts) \tag{5}$$

The electronic gain measured was $3.5\,x\,10^{15}\,fadc\ counts/C$ for the inner Θ sense wires (1-6) and $4.4\,x\,10^{15}\,fadc\ counts/C$ for the Φ sense wires. The gas gain measurement was made by histogramming the area under the output pulse above pedestal of pulses originating from the ionization electrons left by cosmic rays. The number of electrons left in the chamber gas per pulse was

$$Q_{MIP} \cong (29.4\,e^{-}/cm - Ar) \cdot (0.8\,cm) \cdot (1.6\,x\,10^{-19}\,C/e^{-}) \tag{6}$$

$$Q_{MIP} \cong 3.76\,x\,10^{-18}\,C \tag{7}$$

The gas gain was calculated using the electronics gain and the relation

$$Q_{MIP} \cdot Gain_{gas} \cdot Gain_{elect} = Area\,(fadc\ counts) \tag{8}$$

The gas gain was $2.3\,x\,10^4\,C/wire\ pulse$ for the inner Θ sense wires, $5.3\,x\,10^4\,C/wire\ pulse$ for the Θ sense wire 0s, and $3.6\,x\,10^4\,C/wire\ pulse$ for the Φ sense wires. Recall that the Θ sense wire 0s are set at a higher voltage to increase the delay line efficiency.

3.8 Summary

The overall NWA setup was a microcosm of the setup for the real DØ Experiment. From the chamber to the storage medium, the data taking and event processing was an excellent test of the experiment to come. The variety of data taking runs that were obtained with the FDC provided an excellent source of information about the chamber under a wide range of circumstances. Details of the chamber study are available in the next chapter and results of the physics studies are in Chapter 5.

4 Data Reduction and Chamber Calibration

The raw event data was processed using an offline reconstruction package designed and used by the D0 collaboration. The portion used here is a sub-package called FTRAKS written at Northwestern University that only processes data read out from the Forward Drift Chambers. The first step is to perform hitfinding on the FADC output for every active channel. Hits in individual sectors are associated together to form segments. Each segment is formed from the set of hits left by a charged particle as it passed through a sector in one layer. Also, it was possible to reconstruct segments that crossed sector boundaries before leaving the layer. Tracks are formed by matching segments from different layers in one FDC half. At various stages of the reconstruction, corrections are applied to the hits based on results mentioned below.

4.1 Hitfinding

4.1.1 Corrections to FADC Output

Each channel of FADC output is analyzed separately. The original data is zero-suppressed by default and packed 4 bytes to a 32 bit word. However, at the beginning of analyzing a particular sector, all of the channels are unpacked and stored for subsequent use. Each channel of output can contain one or more clusters of zero-suppressed pulses. Each FADC sample of each cluster is converted back (linearized) to the original value it had before passing through the bilinear converter circuit of the FADC. Additionally, the digitized value in each FADC sample is adjusted for crosstalk by the magnitude of the values of the same samples on adjacent wires. If the FADC sample value on an adjacent wire is greater than a predetermined minimum, then the current FADC sample value is reduced by a fraction of that adjacent wire's FADC value. Crosstalk from large pulses on adjacent wires in the Θ chambers decreased the FADC sample value by 5.0% of the adjacent FADC sample value and in the Φ chambers by 7.0%.

After fetching the adjusted FADC output for a particular channel, the values of the pedestal, time zero offset, drift velocity, and gain for the channel are retrieved from the CALIB-filled database. Hitfinding thresholds are set using pre-selected multiples of the standard deviation of the pedestal value. The first differences are calculated and used as slope values for each sample where the first difference of the ith sample is the FADC value of the ith sample minus that of the $(i-1)$th sample.

4.1.2 Basic Algorithm

Each cluster is processed for pulses. Pulses are found using a method similar to the zero-suppression chip mentioned earlier. It is a technique similar to the one used at the OPAL experiment [21]. First, two successive first differences above a threshold must occur. The next FADC value must exceed the pedestal plus the threshold. Then, either the next first difference exceeds the threshold or both of the current two first differences must exceed a much larger threshold. If these tests are passed then a pulse has been found. The beginning of the pulse is set to be the FADC sample before the first difference that satisfied the cuts. The leading edge of each pulse is calculated by weighting the sample values for each sample starting at the beginning of the pulse and ending at the sample where the pulse starts to decrease. This decrease is determined by two successive negative first differences. The weight used is 0.6 raised to the nth power where n is the number of samples from the start of the pulse. This weighting sets the leading edge near the beginning of the pulse as opposed to close to the peak of the pulse which favors the arrival time of the first drift electrons. The leading edge is used to calculate the drift time of the pulse. It is adjusted by the timing pulse sample value which has been corrected first for its own delay. If the drift time of the leading edge or the pulse search goes beyond a predetermined limit then the search for pulses in a channel is stopped as the pulse would have been outside the sector's physical walls by over 25%

of the maximum drift distance. The peak height is the FADC value of the sample that started the two successive falling (negative) first difference values. The pulse tail endpoint is found by reversing the pulse finding method; succesive falling samples below a threshold and a sample below the pedestal plus a threshold. Two successive samples below the pedestal level, a new rising edge, or simply too long a tail are also used as cutoffs.

Pulse area is calculated as the sum of the FADC sample values from the first sample to the tail sample of the pulse less the pedestal level. A cut is also made on the pulse area to eliminate small pulses due to noise that occasionally satisfy the pulse threshold cuts. Risetime is the number of samples the pulse takes to rise from 10% to 90% of the peak height value above pedestal. Falltime is similar but is sought over the samples following the peak.

The information stored for each pulse is the drift time in nanoseconds obtained by multiplying the adjusted sample position of the leading edge by 9.434, the number of nsec per sample. The pulse width in nanoseconds is the tail sample less the first sample multiplied by 9.434. The pulse area and peak pulse height are also stored but only after being multiplied by the channel gain. Also, risetime, falltime, and overshoot can be stored upon request at analysis time.

As an option, the cluster FADC sample values can be passed through a pulse shape subtractor. This function subtracts off a standard pulse shape normalized to the current pulse area from the FADC sample values. This technique is useful to resolve two pulses that occur almost simultaneously [22]. Pulses that peak within a few FADC samples of each other add together so that the intervening samples fill in and wash out the falling edge of the first and the leading edge of the second. If the pulse finding algorithm fails to find the falling tail of the first pulse and can not find a leading edge for the second, two pulses are treated as one very large pulse. Using pulse shape subtraction, the first pulse on average can be removed leaving behind the second pulse which by itself is easy to find. The NWA testbeam data, unfortunately, contained many pulses with extremely long tails lasting more than 100 FADC samples. The pulse shape subtraction method when applied to these lengthy and slowly falling pulses could not adequately subtract off the long tail. The sample values remaining were of the proper size and value for the hitfinding to find a new pulse where one did not actually exist. This can be repeated several times for a very long tail. These false hits can be reconstructed as segments if there are enough wires in one sector with long tails. This process is also very time consuming for the analysis (mostly because of the false hits) and was used only on selected occassions.

4.1.3 Processed Hits

After the pulses are found for all of the channels in a given sector, the information is stored for processing. This processing converts each pulse's data to more useful information. Drift times are multiplied by drift velocity to yield drift distances in centimeters from the sense wires. For sectors with possible left-right ambiguity, the possible drift distance on each side of the wire is stored. For the sectors without left-right ambiguity, the position on the back side of the sense wire plane is stored only if it is small enough ($< 0.42\,cm$) to be within the volume of the physical sector. Errors in drift distance are set at $0.036\,cm$ for Θ hits and at $0.024\,cm$ for Φ hits. The higher value for the Θ hits is due to a larger resolution which will be shown in Section 4.4.2. Pulse area is multiplied by a conversion factor to obtain the number of MIPs (minimum ionizing particle equivalents) of ionization. This processing is done first for each sense wire in a sector and then stored by sector for use in making tracks.

4.1.4 Delay Line Hits

Once all of the hits for the sense wires of a sector are processed, the delay line pulses are processed. Since the delay lines are read out at both ends, there are two pulses, one on each channel for every hit on the adjacent sense wire 0. Each pulse on sense wire 0 is compared with every possible pair of delay line hits, one from each delay line end. The sense wire drift time is subtracted from the pair of delay line pulses. The remainder of each of the two times is converted to a distance using the velocity of pulses along the delay line. The two distances are added together and this should correspond to the actual length of the delay line. The best combination from amongst all the possible pairs is selected if it matches the total delay line length within 15.0 *cm*. If successful, a calculation locates the delay line position of the successful pair by taking half the difference of the distances. This information is then stored with the corresponding sense wire 0 processed hit. Additional sense wire 0 hits are matched with remaining delay line hits until there are no remaining delay line hit pairs within the window or until all the sense wire 0 hits are matched. Optionally, after all pairs are used or rejected, single delay line hits can be associated with sense wire 0 hits if the distance is less than the total length of the delay line. This is not used as the default method. The error on the delay line position is set at 0.50 *cm* if both delay ends are used to determine the hit position and at 2.00 *cm* if only one delay line end was used to determine the hit position.

4.2 Segment Building

A segment is the portion of a charged particle track that lies within a single layer, either a Θ or a Φ layer, of one FDC Half. Segment building proceeds by accepting hits from each wire within a narrow spatial aperature (roads). These hits are fit to a straight line and saved if the χ^2 per degree of freedom is less than a predetermined value.

4.2.1 Basic Algorithm

The hits on the outermost wires of the sector are used to locate roads. For example, in a Θ sector, sense wire 0 and sense wire 7 are used at the start. Each hit, both left and right possibilities, on sense wire 0 is matched to a hit on sense wire 7. For each pair, a road of constant radius (0.16 *cm*) is determined using the two hits as the end points. Hits on intervening sense wires are checked to see if they are in the road. It is possible for more than one hit per wire to be located in the road. However, there must be a minimum number of wires contributing to the segment road, 6 of 8 for the Θ sectors and 10 of 16 for the Φ sectors. Every possible combination of hits in the road at one hit per wire becomes a segment candidate. If more than a preset number (5000) of possible combinations has been made, then the road is thrown out and the processing goes on to the next road. A large number of combinations in a single road can greatly slow down the processing of many events. After all hits have been selected, a straight line fit is made to each possible combination of hits, one only per wire. A chi-squared per degree of freedom is calculated for each fit using the hit errors as given above. The combination with the lowest χ^2_n/dof is stored as a segment if the χ^2_n/dof is less than 5.0. Its hits are marked so that they are not used on another segment. In the situation where two segments are trying to use the same hits, then the priority goes to the segment that points back to the interaction region (as if the chamber were at DØ). The priority was used for testbeam runs in which the FDC chamber was rotated but was not used for runs in which the FDC chamber was aligned with the beam. Once selected, the segment is prepared for storage and later use in tracking. After the roads defined by sense wires 0 and 7 are evaluated, other outer sense wire combinations are used to define roads. For example, roads could be determined by hits from sense wire 0 to 6, 1 to 7, and 1 to 6. All combinations are tried until there would be too few wires in the road to yield the minimum number of hits for a good segment. In addition, if the segment does not have a sense wire 0 hit then a search is made in the adjacent sector if the segment could have extended into it. If a hit lines up with the segment then the hit and its delay line information, if any, are stored with the segment. The positions of all the hits are adjusted by a correction based on the slope of the segment. Angled segments have their pulses arriving early due to geometry effects of the drift volume and the wire position. The effect is greater the higher

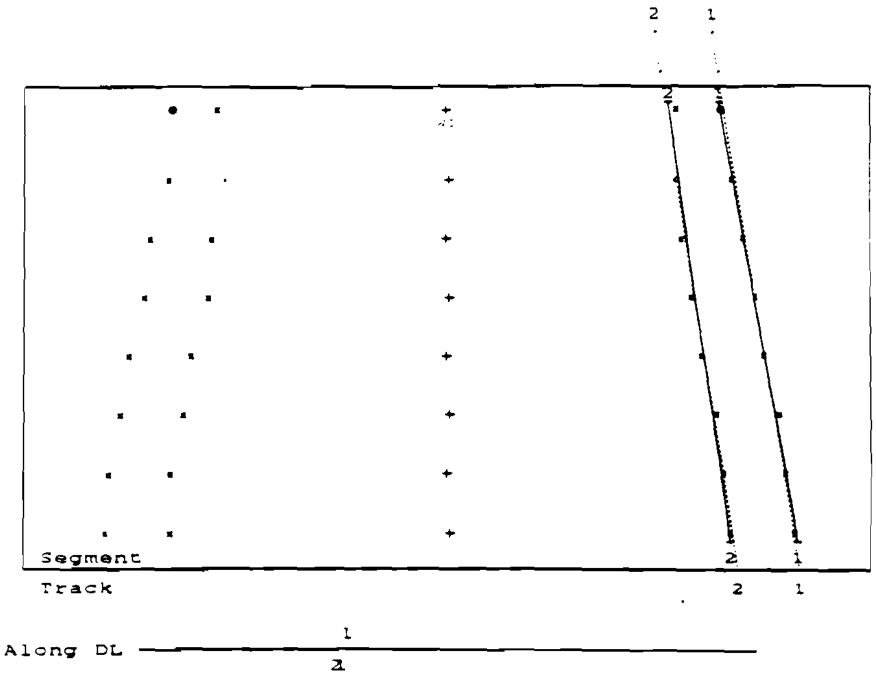

Figure 11: Sample Reconstructed Segments

the angle of the segment. Thus, the hit errors are reset to $0.036 + 0.046 * slope^2\,cm$ for Θ hits and $0.024 + 0.031 * slope^2\,cm$ for Φ hits. The adjustment is small for low angles but in the Θ sectors, the slope of the segment can exceed 0.57 ($\approx 35^\circ$) which would be $0.015\,cm$ to a Θ hit. A sample reconstructed segment is shown in Figure 11. The solid lines show the fitted segments and the dashed lines show the tracks to which they belong. Also shown in the sector are the ambiguity hits on the other side of the sense wire plane. Along the bottom is the matchup between the delay line position as found only for segment 1 and the track positions along the delay line.

4.2.2 Near-wire and Cross-wire Segment Algorithms

The left-right ambiguity can cause a large increase in the number of segment hit combinations when the segment is close to the sense wires. This is a particular problem in the Φ sectors which extend to within 11 *cm* of the beam. A pair of charged particles could pass close to the sense wire plane, for example a photon conversion pair. Each hit will be on either side of the sense wire so it effectively doubles the possibilities for each hit. Factor in two hits close to each other near the wire plane and 16 wires worth of hits in a Φ sector and the number of possible segment candidates can reach over 4 billion. The same situation in a Θ sector generates only about 65000 combinations. For roads located near the sense wires, a radius of 0.16 *cm* is used for the Θ sectors and a radius of 0.06 *cm* is used for the Φ sectors. The Θ road is the same width as is normally used because the problem is not as bad with the lower number of wires involved. Combined with a preset maximum number of combinations allowed of 5000, this problem is controlled adequately enough that the overall event analysis rate will not plummet to zero. In the target data runs at NWA, there were sectors of both types that contained roads of more than 5000 combinations of segment candidates occurring at a rate of one every five events in the higher incident beam momenta runs.

4.2.3 Cross-sector Segment Algorithms

The Θ chamber inter-sector walls are necessarily positioned in a way that intercepts some of the charged particles coming from the interaction region of the DØ Detector. Also, particles from secondary vertices can enter the chambers at non-central angles and pass through inter-sector walls. Thus, a segment could have some of its hits in one sector and the remainder in an adjacent sector of the same layer. It is desirable to reconstruct all segments. All single sector segments are found first thus leaving far fewer unused hits in each sector. These unused hits are treated as candidates for cross-sector segments. Each sector is examined for its remaining hits and compared with its neighboring sectors. If the current sector has some hits starting from near sense wire 0 and a neighbor has some leftover hits starting from near sense wire 7, an attempt is made to fit a cross-sector segment.

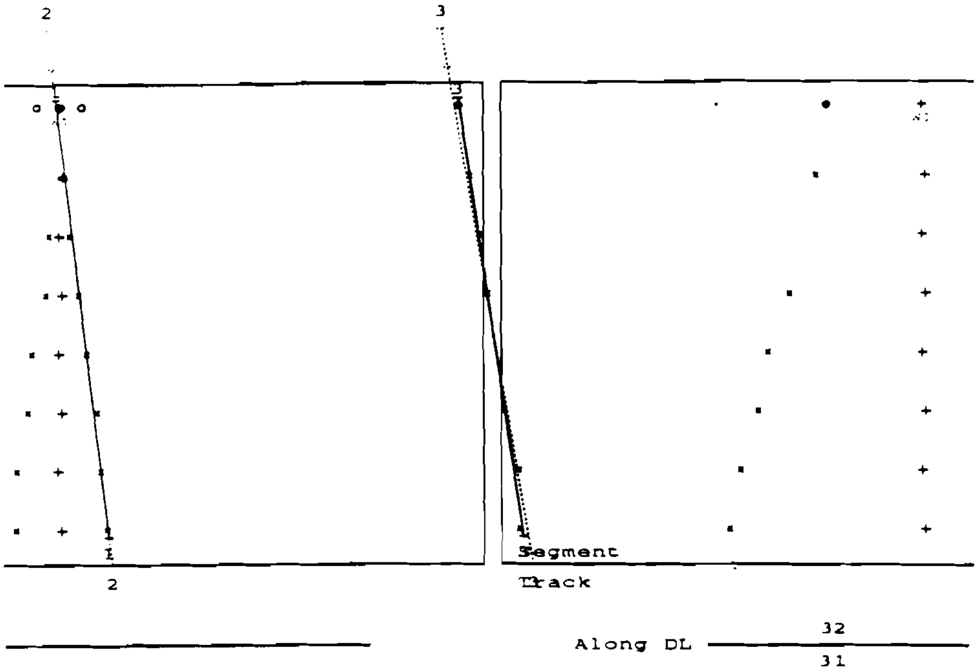

Figure 12: Sample Reconstructed Cross-Sector Segments

Since adjacent Θ sectors have the same distance between corresponding sense wires in adjacent sectors along the entire wires' lengths, the drift distance of the adjacent sector's sense wire hits are easily converted into distances from the starting sector's sense wires. From the pool of available hits, roads can be formed and segment combinations tested. Roads are made extra wide ($0.30\,cm$) to make allowances for the additional errors incurred and possible multiple scattering of the original particle due to passing through the wall. Segments are saved if their χ^2_n/dof is less than 50.0, a larger limit than allowed for normal segments.

Cross-sector segments in the Φ chamber must be formed using a different method. The corresponding sense wires in adjacent sectors separate as the radius increases and the hits do not have a radius associated with them. Therefore, it is not possible to translate a hit position from one sense wire plane to an adjacent sector's sense wire plane. A strategy that can be used is called the link-and-tree method [23]. Chains of hits are built in a starting sector and an adjacent sector. The pairs of chains in the two sectors can be combined into a full segment combination. An advantage of crossing the sector boundary is that the largest drift time hits on each side of the septum wall yield a rough determination of the radius of the segment. This information is used to translate the hits in the adjacent sector to the starting sector coordinates and a line fit is applied. Segments are saved if their χ_n^2/dof is less than 100.0, a larger limit than allowed for normal segments. Sample cross-sector segments are shown in Figure 12.

4.3 Track Building

Tracks are assembled from the segments built in the Θ and Φ layers. A segment of hits from each layer is used in a 3-dimensional track fit. If the fit passes quality cuts, it becomes a reconstructed track whose basic parameters and fit information are then stored for later use.

4.3.1 Basic Algorithm

The initial step is to assemble a set of three segments, one from each layer, to form a track candidate. This set is referred to as a ladder. Ladders are formed starting with segments in the inner Θ layer. Each segment is matched up with segments in the outer Θ and the Φ layers using the theta and phi angles of each segment. First, inner and outer Θ segments are matched if the theta angles match within a tolerance of $0.06\,rads$. Depending on the presence of delay line hits, a match in phi angle is made within a difference of $0.15\,rads$ for both delay line hits present and wider if one or both delay line positions are missing. Matches are disallowed when the inner layer Θ sector is more than two sectors farther out than the outer Θ sector. In the DØ Detector, this cut would eliminate possible tracks due to particles back scattering off the substantial amount of material behind the FDCs. It is not yet known how much of a problem this will be for the reconstruction package. In the testbeam, it would eliminate tracks made from particles rebounding off the various supports and material behind the FDC. The information from two matched Θ segments is then used to calculate an approximate radius from the center of the FDC. Possible Φ segment candidate phi angles are adjusted using their drift distance at the approximate radius and this is matched to the average phi angle of the two Θ layer segments to within a tolerance of $0.15\,rads$. If all these cuts are passed then a three-layer track ladder is formed. Matches are also retained for any two layer combinations that match in theta and phi that do not have a match in the third layer. This allows for tracks that pass through non-active regions of one layer but pass through active regions of the other two layers. Track fitting is performed on the three-layer track candidates first then the two-layer track candidates. Leftover segments are assembled into two-layer ladders if their sectors overlap in a view projected from the interaction region. This is a last chance to assemble candidate ladders. A final round of track fitting is performed on these candidates.

When a ladder is passed to the track fitting routines, an initial track fit is made using the segment fit information and the delay line hits. If the Φ sector segment is a cross-sector segment, then a fit is made using all the hits individually. A normalized chi value for the track fit is calculated from the track χ^2 to be

$$\chi_n^2/dof = \sqrt{2*\chi^2} - \sqrt{2*(dof-4)-1} \tag{9}$$

The χ_n^2/dof should have a distribution mean of 0.0 and s standard deviation of 1.0 for a fit made with more than $\approx$ 30 degrees of freedom. If the distribution is off-center, the errors on the hit positions are too small for a mean greater than zero or too large if the mean is less than zero. Here, if the fit has a normalized chi value of less than 20.0 or it is a two-layer track, the candidate track is passed through a checking routine that calculates the sectors the track is supposed to have passed through given the fit results. This must match the list of sectors to which the segments belong. If it is a two-layer track, checks are made to make sure there was a valid reason for the third layer to have been missed. Tracks passing through intersector boundary regions, a crowded environment, or outside the chamber in the missing layer are all valid reasons and the track will be accepted. Next, the track is passed on to a full track fit using all the hit information. The full fit must have a normalized chi value of less than 10.0 for three-layer tracks or a segment fit normalized chi value of less than 4.0 for two-layer tracks. A full fit must be used for two-layer tracks in which one is a Φ cross-sector segment. Two-layer tracks must be treated more harshly because of the increased likelihood of making a mismatch between segments from two different tracks which are close together. The stored χ_n^2/dof for the track is always the one used to make the final decision. If it is a two-layer track then it is projected into the third layer to find a segment. All segments in the sector in the third layer that it passes through are tried in a segment fit. If a fit passes all the aforementioned checks and cuts then it is retained as a successful three-layer candidate.

All tracks that have passed the checks and cuts above are compared and selected according to a four level hierarchy. Within each level, the tracks are chosen by the lowest normalized chi being selected first. Three-layer tracks pointing toward the DØ interaction region are chosen first. Three-layer tracks not pointing towards the DØ interaction region are chosen second. Two-layer tracks with at least one delay line hit and pointing towards the DØ interaction region are third and two-layer tracks with at least one delay line hit and pointing away from the DØ interaction region are last. All two-layer tracks must have at least one delay line hit involved in the fit. The maximum number of times a segment can be used on a track is twice and any further tracks that use the segment are rejected. Successful tracks have their basic fit parameters saved along with the fit results for the individual hits.

4.4 Chamber Calibration

The accuracy with which a track can be measured depends on the accuracy of several calibration measurements that affect the position of the hits on the track. Electronics calibration was covered in Section 3.7. The chambers require their own calibration to understand the processes that occur between the time and place a track leaves behind charged ions to the time that a signal enters the electronic readout chain. An accurate drift distance to drift time relationship must be measured and monitored. A detailed knowledge of the chamber geometry is necessary as well as an understanding of the electrostatic drift field. The effects of the electronics chain include the electronic noise, individual channel delays, cross-talk, and pulse shaping. Finally, the software reconstruction hitfinding optimization also contributes.

4.4.1 Drift Distance and Drift Velocity

This relation is very critical to the use of the FDCs considering the maximum drift distance is $5.3\,cm$ for which a 1% error in measured distance is $500\,\mu m$. The desired operating resolution of the FDCs is $200\,\mu m$ or less and therefore requires precise knowledge of many factors. The drift velocity in the gas is affected by the field voltage, the gas temperature, pressure, and composition. Also, corrections have to be made for track angle and distance from the wire.

The variation of drift velocity with field voltage was measured with the FDC Canary test cell. This test cell is a single sector of the same size and operation as a Θ sector 3 and whose electronics readout chain is identical to that used for the FDC chambers themselves. Using the FDC Canary test cell, a plot of the drift velocity versus field voltage per centimeter was obtained and it shows that the FDC operating field voltage is well past the peak and out along the slow-changing tail of the distribution typical for saturated gases. Some measurements using the FDC directly are also included. See Figure 13. This indicates that the FDC should be insensitive to reasonably small

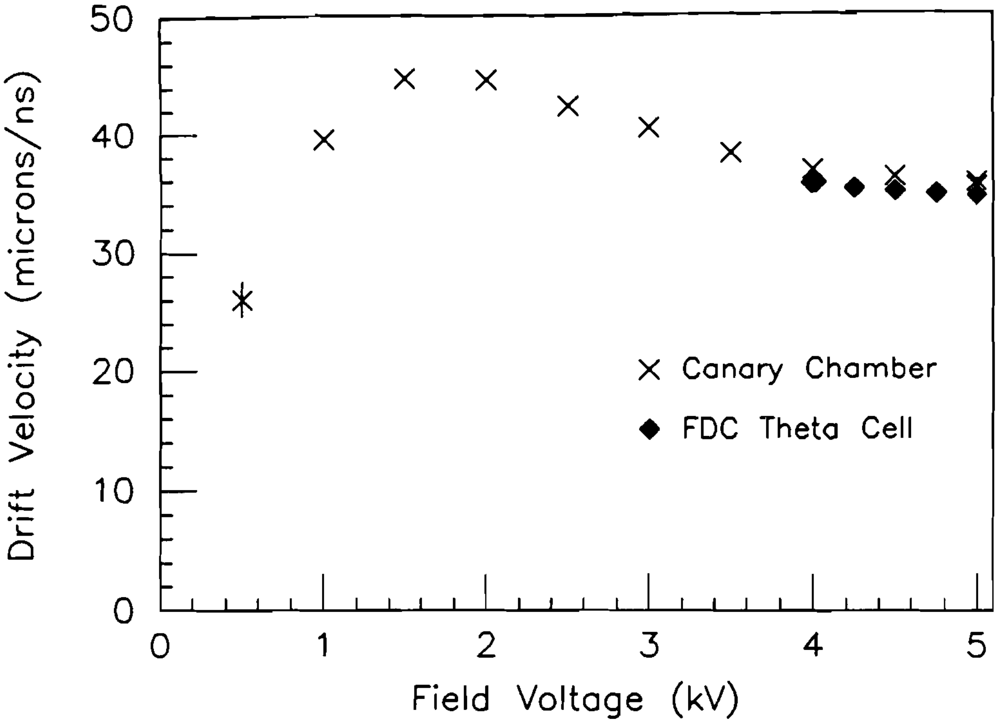

Figure 13: FDC Canary Gas Drift Velocity vs Field Voltage

deviations (±200 V) from the nominal operating field voltage of 5.0 kV. That is 962 V/cm of drift in the Θ sectors and 943 V/cm in the Φ sectors. Ambient temperature and pressure were recorded for each data taking run. The effects of changes in temperature and pressure eventually will be mapped using the Canary chamber but are not available at this time.

To understand the other corrections, the drift distance versus drift time measured was plotted where the drift distance to the wire plane is measured externally by the PWC track. The resultant distributions for a Θ half-sector show a linear relation over most of the drift volume with a typical velocity of 34 $\mu m/nsec$. See Figure 14. Distributions for a Θ full-sector over its full width and near the wire plane are shown in Figures 15 and 16 [24]. The only difference comes in the region close to the wire plane (±0.5 mm) at which point the actual measurement accuracy of the PWCs effectively smears out a more accurate result. Also, this is the gain region of the drift field due to

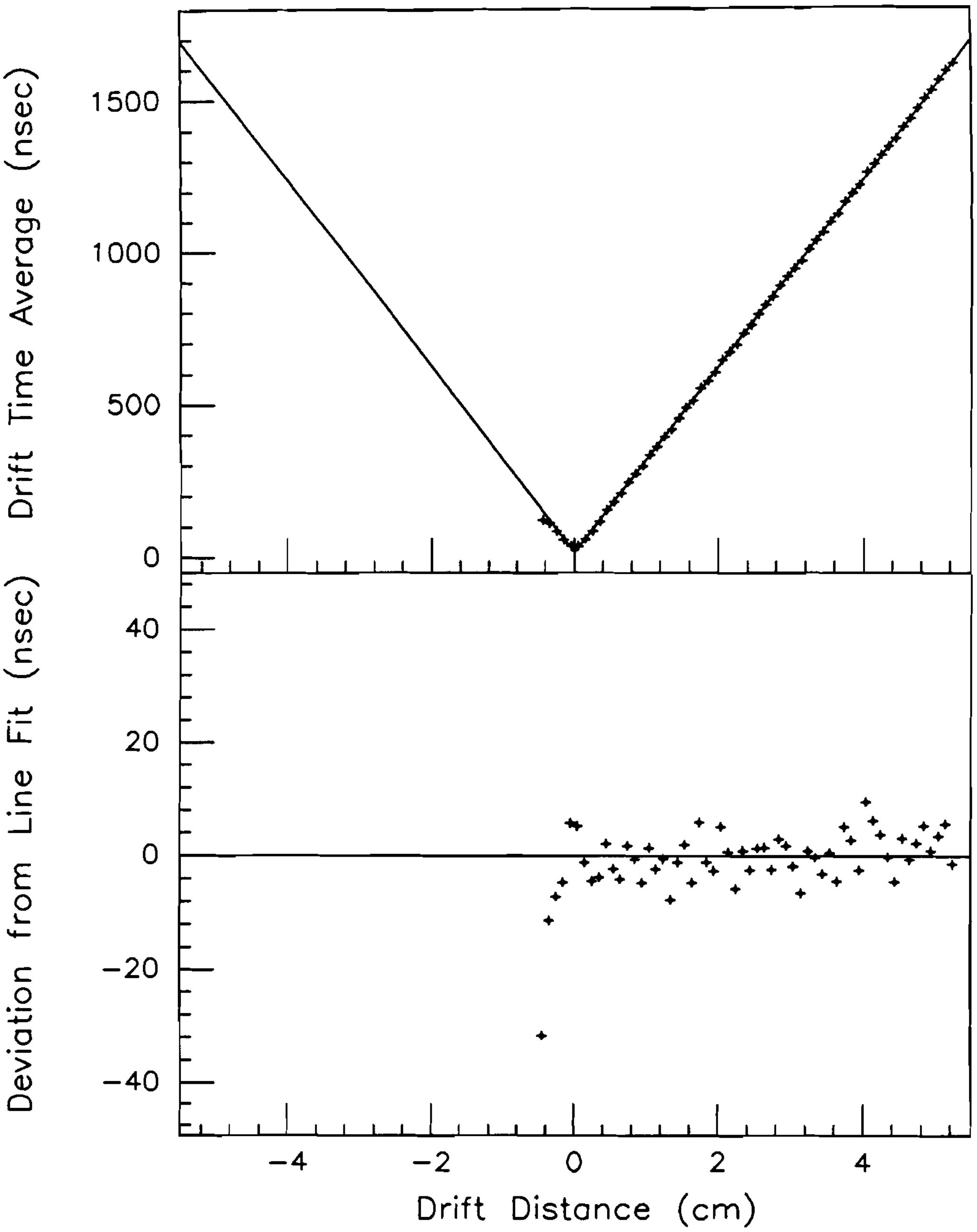

Figure 14: Typical Drift Time vs Drift Position Distribution for Θ Half Sector

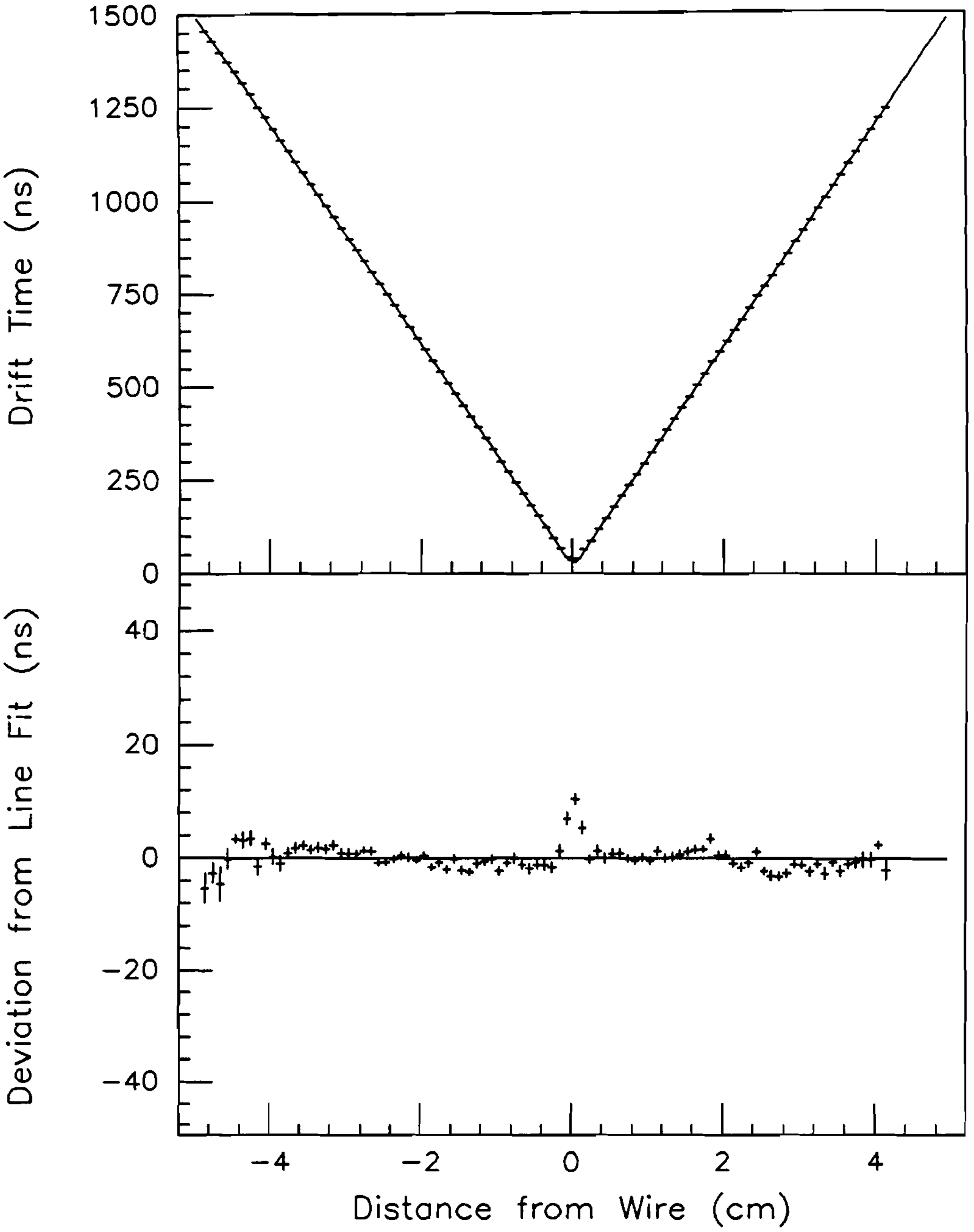

Figure 15: Typical Drift Time vs Drift Position Distribution for Θ Full Sector

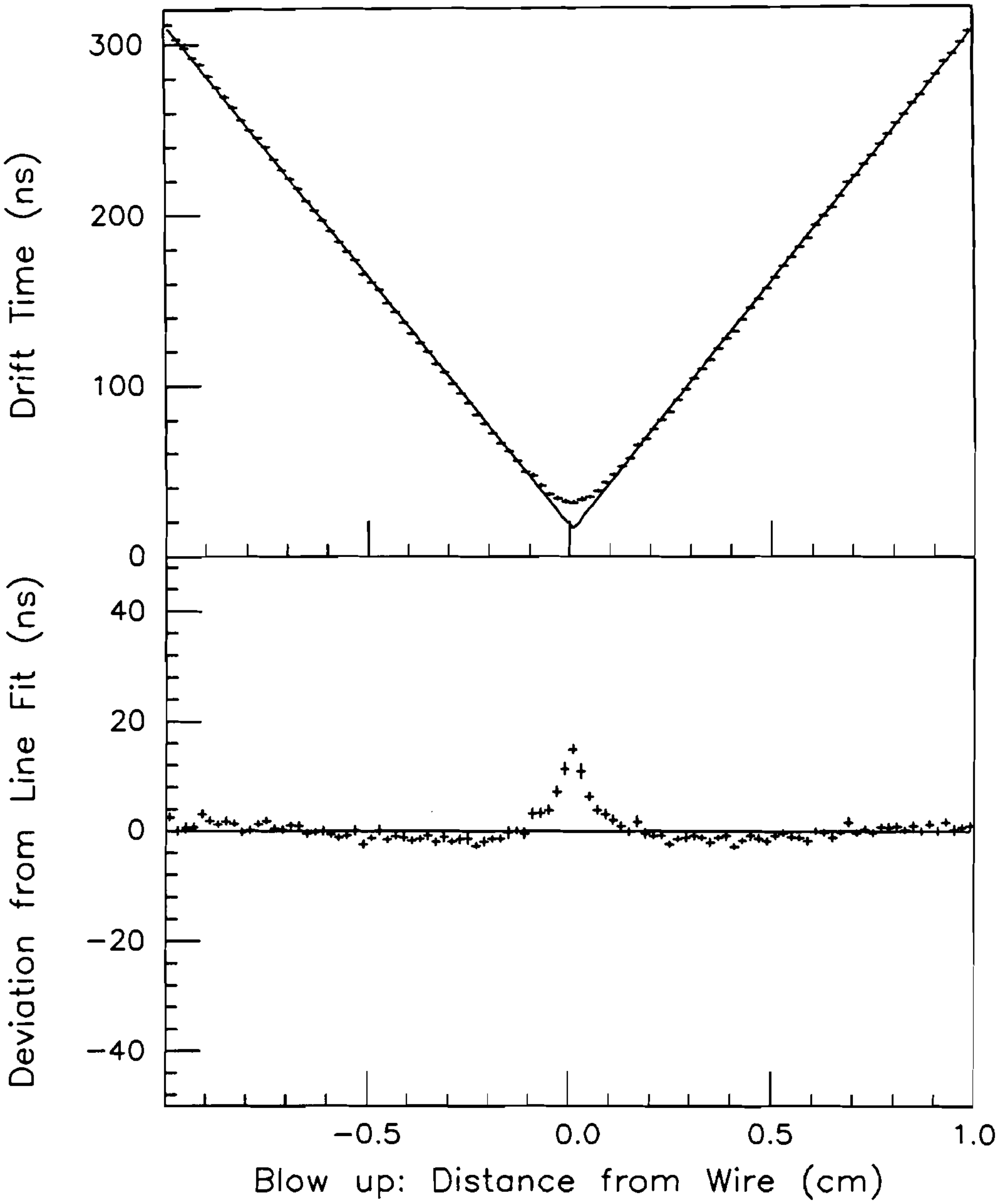

Figure 16: Typical Drift Time vs Drift Position Distribution for Θ Full Sector - Innermost 1 *cm* of Drift

the anode wire field and is non-linear. The linear region extends from 1 *mm* out to the full sector width. For the full sectors, the data can be fit separately on both sides of the sense wire plane. The typical difference in drift velocities between the two sides is 0.1% for tracks parallel to the sense wire planes. For the half-sectors, the drift velocity of the small region behind the wires is treated as if it had the same drift velocity as the large drift region. There is no field voltage there, just the anode wire field, but the maximum drift is only 0.40 *cm* and the fit to the short stub in the distance versus time plot is reasonably close in slope to the velocity in the main volume. Also, there is a small wire-to-wire variation in the drift velocity which is less than 1% but is not understood at better than the 1% level. The Φ sectors behave similarly to the Θ full sectors however the innermost and outermost sense wires have a slightly higher drift velocity in general.

It is also possible to measure the drift velocity online by looking at cross-sector segments. It can be determined, given the chamber geometry how far the sector walls are from the sense wire planes and therefore how far the crossover hits are from the sense wire planes. That is, the last hit in the first sector and the first hit in the adjacent sector must drift close to the maximum drift distance. Using all of the hits on the segment on both sides of the inter-sector wall, a more accurate determination of these two hit positions is possible. This calculated distance is then divided by the drift time for the hit yielding a drift velocity. The velocity is assumed to be uniform over the drift region given the findings above. This technique allows all sectors of the FDCs to be tested on a continual basis. Another technique usable online, during data collection, divides the width of the drift time distribution by the maximum drift distance to obtain an approximate drift velocity. The overall findings for the FDCs using all of the methods mentioned above show a fairly constant (within 1%) velocity for all the sectors in a Θ quadrant and similarly for a Φ unit. The velocity changes parallel the division of the high voltage and gas feeds to the various detector sub-units.

4.4.2 Hit Resolution and Efficiency

Hit resolution and efficiency is determined by looking at reconstructed tracks. The track fit can be redone for each hit, excluding the hit from the fit, and then the distance of the hit to the track is stored as the hit residual. The standard deviation of the hit residual distribution is the hit resolution. Wire hit efficiency is determined by accumulating the number of times a track passing through a particular wire volume has a hit on that wire.

vs Drift Distance The single wire resolution versus drift distance in typical sectors is shown in Figure 17. The overall trend follows a general theoretical model in which three major effects are at work [25]. There is a contribution from electronic noise which adds to the resolution independently of the drift distance. Added on to this are near-wire effects due to complicated effects of primary electron statistics and the highly non-linear drift velocity region near the anodes. Near-wire effects fall off exponentially with distance. The third major contributor is the physical diffusion of the electron swarm along the drift direction. This effect increases as the square root of the drift distance. The hit resolution over the full drift distance has a minimum of $150\,\mu m$ at $0.7\,cm$ and rises to about $200\,\mu m$ at $4\,cm$ for a typical Φ sense wire. The hit resolution over the full drift distance has a minimum of $163\,\mu m$ at $0.9\,cm$ and rises to about $240\,\mu m$ at $5\,cm$ for a typical Θ sense wire.

vs Track Angle The hit resolution versus track angle was measured in a set of data runs taken with the FDC at preset angles to the beam from 0° to 32.7°. Tracks through the Φ layer did not go beyond an angle of 17.8° because of the orientations possible in the testbeam setup. In the DØ experimental area, the track angles are not expected to exceed these values for both layers due to the orientation of the chambers to the beamline. However, secondary interactions could produce charged particles with higher angle tracks in the chambers. The results, shown in Figure 18, show

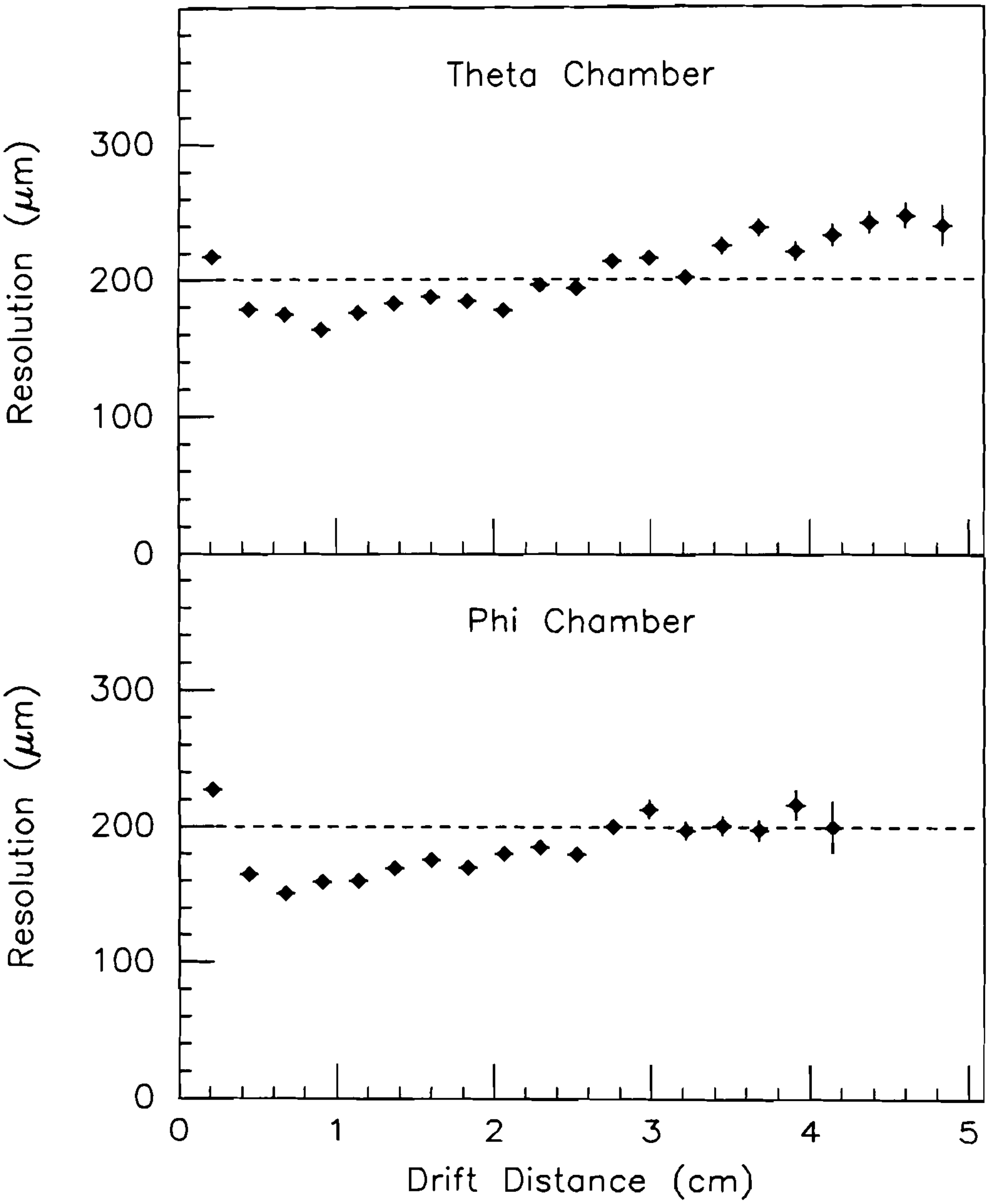

Figure 17: Hit Resolution and Efficiency vs Drift Distance for typical single wires, one in a Φ sector and one in a Θ sector

less than a 10% degradation in resolution until the track angle goes beyond 25° for the average hit resolution in Θ of $210\,\mu m$ and in Φ of $170\,\mu m$. The higher the angle of the track with respect to the wire plane, the more spread out along the drift direction is the electron swarm. Thus, the electrons arriving first at the sense wire are much fewer in number than for a track parallel to the wire plane. This makes the resolution much more susceptible to the fluctuations that can occur for each electron passing into the gain region of the sense wire. Fewer electrons don't allow statistics to average out the fluctuations.

vs Sense Wire High Voltage Setting the high voltage of the anode wire requires a compromise between the desire for perfect hitfinding efficiency with good hit resolution and the limitation of maintaining a high voltage on a thin wire in a hostile environment. For the Φ sense wires, the balance was reached at $+1500\,V$ where the hitfinding efficiency reached 96.5% and the resolutions are as stated above. See Figure 19. For the Θ sense wires, a slightly higher sense wire voltage of $+1550\,V$ was chosen for a hitfinding efficiency of 95%. See Figure 20. These were the most reasonable values for the sense wire voltages given the need to limit breakdowns that would trip off the voltage to the chamber from occurring more than once every few days. If one looks at the pulse height divided by the standard deviation of the pedestal level in the FADCs, a signal to noise ratio is obtained. It averages between 400 and 500 for the Φ sense wires and between 200 and 300 for Θ sense wires. The Θ delay lines have a signal to noise ratio of ≈ 145. This lower value is due to greater fluctuations due to noise in the pedestal of the FADCs and the smaller pulse heights obtained from the delay lines. Signal to noise results are shown in Figure 21.

for Θ Half Sectors Hit resolution in the Θ half sectors is complicated by the small region on the back side of the sense wire plane which has no linear drift region. Using the drift velocity obtained from the full drift side of the wires, the hits occurring on the back side could be used on tracks and

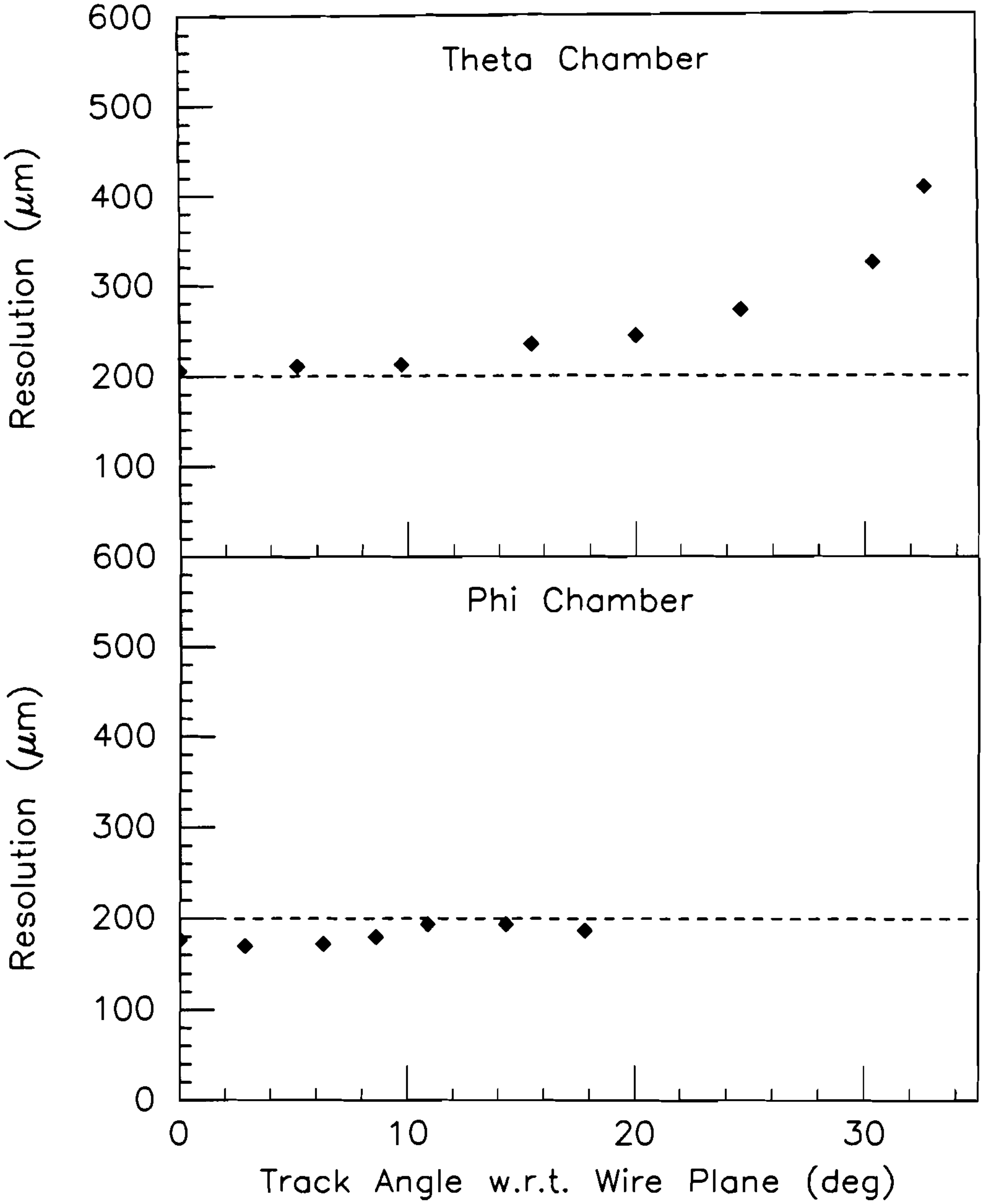

Figure 18: Hit Resolution and Efficiency vs Track Angle for typical single wires, one in a Φ sector and one in a Θ sector

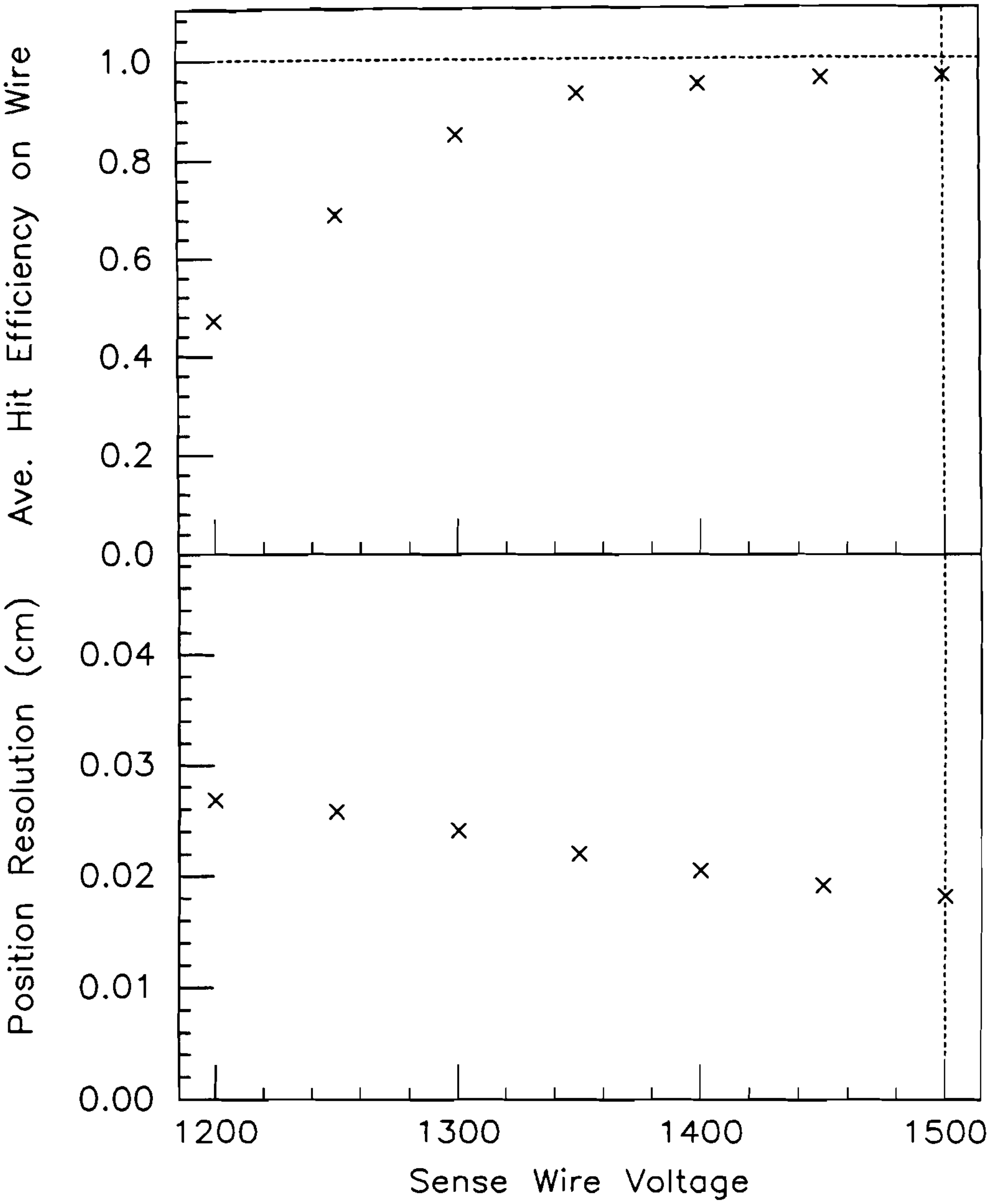

Figure 19: Hit Resolution and Efficiency vs Sense Wire High Voltage for typical single wire in a Φ sector.

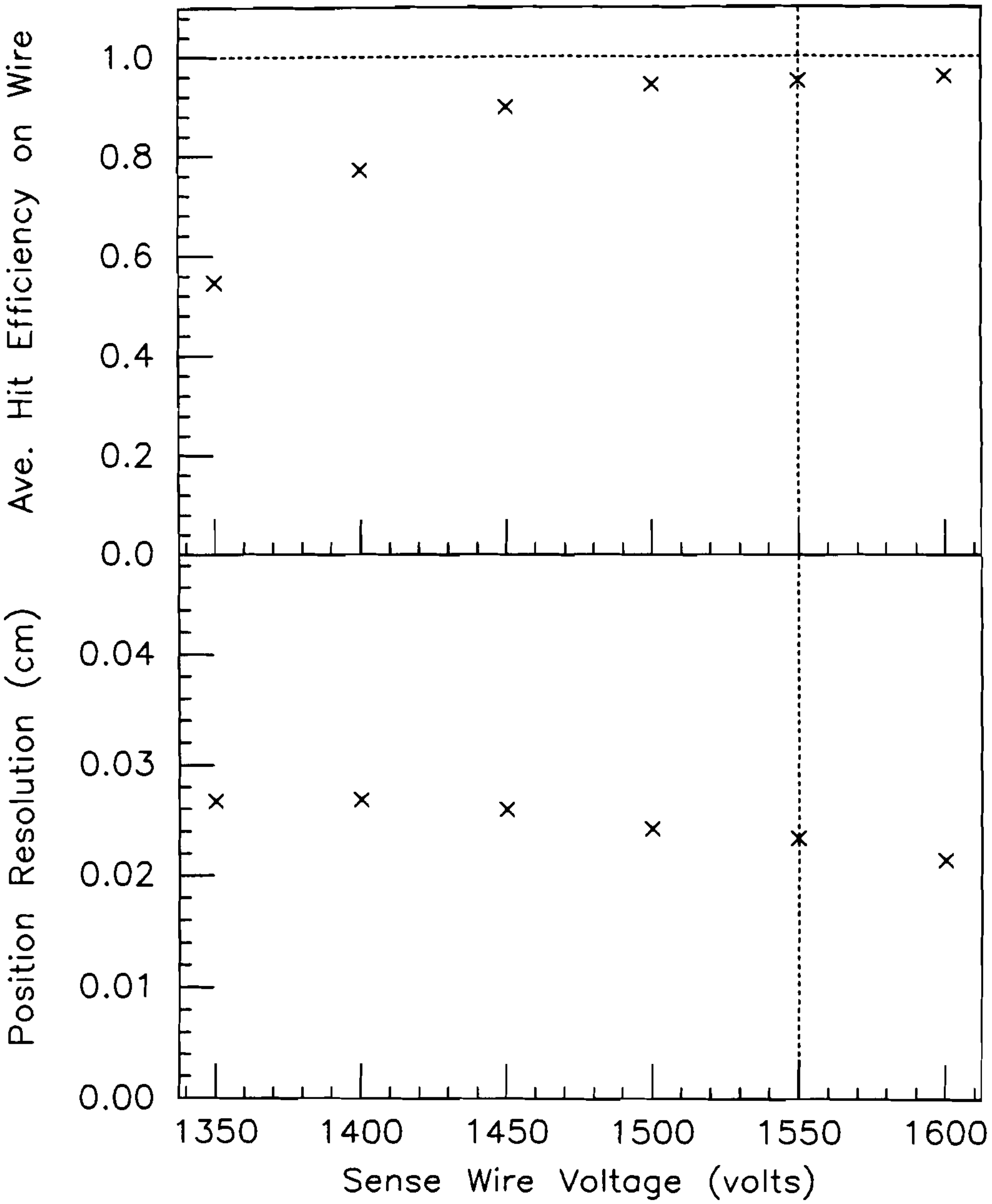

Figure 20: Hit Resolution and Efficiency vs Sense Wire High Voltage for typical single wire in a Θ sector.

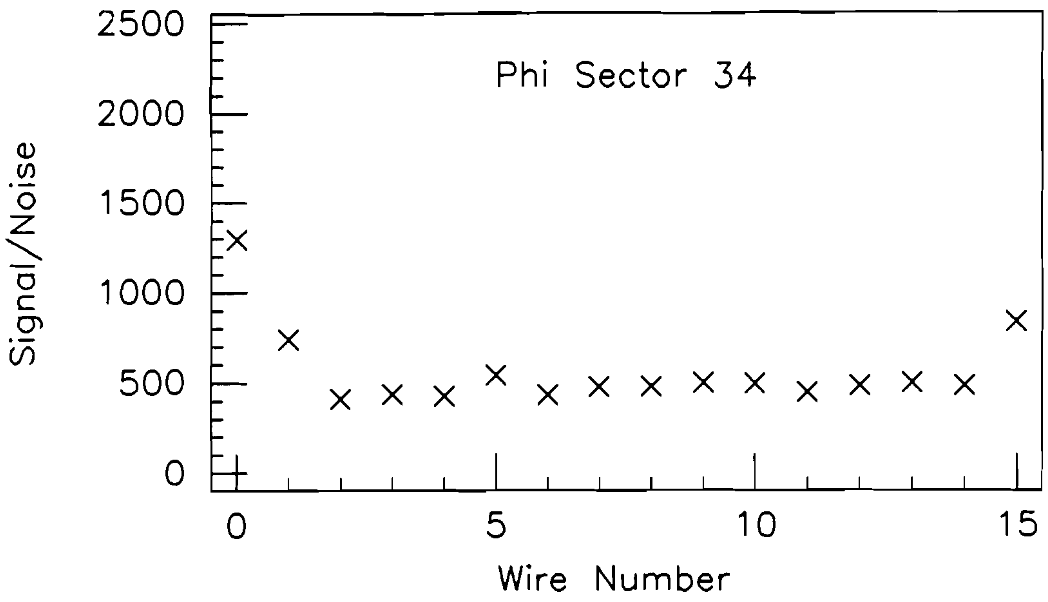

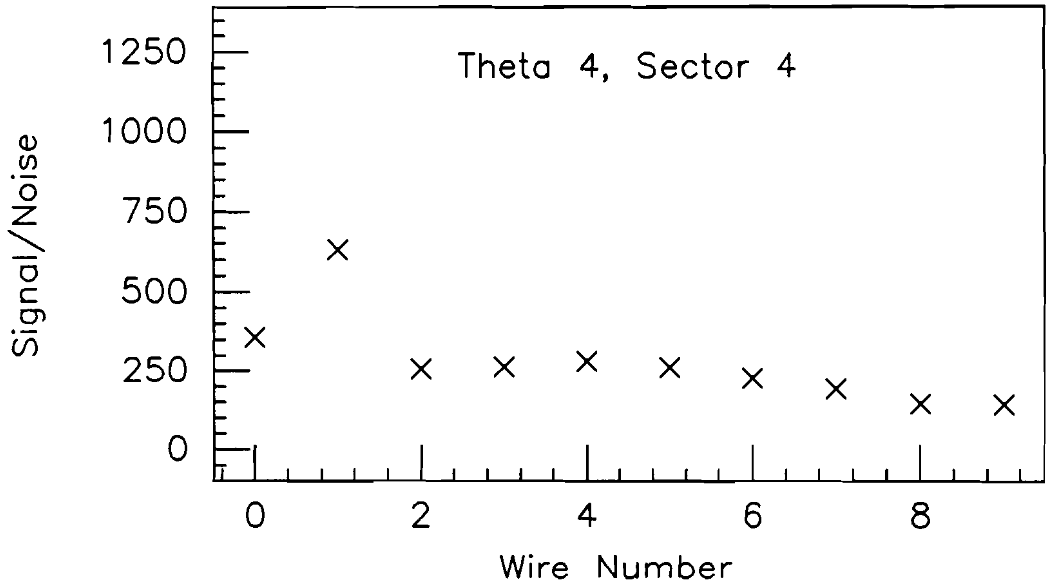

Figure 21: Signal to Noise ratios for a typical Φ sector and a typical Θ sector. Note that wire 8 and 9 in the Θ sector are the delay line ends.

hit resolutions determined. The average resolution at $210\,\mu m$ is almost identical to that of hits on the full drift side. See Figure 22.

4.4.3 Pulse Risetime and Pulse Width

The pulse risetime and pulse width distributions versus drift distance follow the same trends as the hit resolution and for similar reasons. Near-wire effects dominate at small drift distances but fall off quickly and dispersion effects of the electron swarm increase slowly with drift distance. Risetime is determined by the time it takes the pulse to rise from 10% to 90% of its peak value above pedestal. For most drift distances this value averages $10\,nsec \pm 5\,nsec$. See Figures 23 and 24. The pulse width is determined by the time it takes the pulse to rise from 10% to its peak and fall back down to 10%. For data taken with the old shapers, the pulse width ranges between 165 and $180\,nsec$ $\pm 35\,nsec$ for Φ sectors and between 155 and $170\,nsec$ $\pm 30\,nsec$ for Θ sectors.

4.4.4 Pulse Height

The pulse height is very good for the purposes of using the FDC as a sampling tracking chamber. This can be seen in the results given above of hitfinding efficiencies under various conditions. The signal to noise ratios show this quite clearly. The pulse height is also adequate to determine dE/dx for charged particle tracks. Each track has a calculated truncated mean pulse height per hit determined by the average of the smallest 75% of the hits. The resolution of the truncated mean pulse height of single pion tracks is 13.3% and the distribution is shown in Figure 27. Much greater detail is given elsewhere [11].

4.4.5 Delay Lines

The hit resolution and efficiency are directly related to the pulse height that is achieved on the adjacent sense wire for a hit. As the Θ sense wire 0 high voltage is raised increasing the sense wire

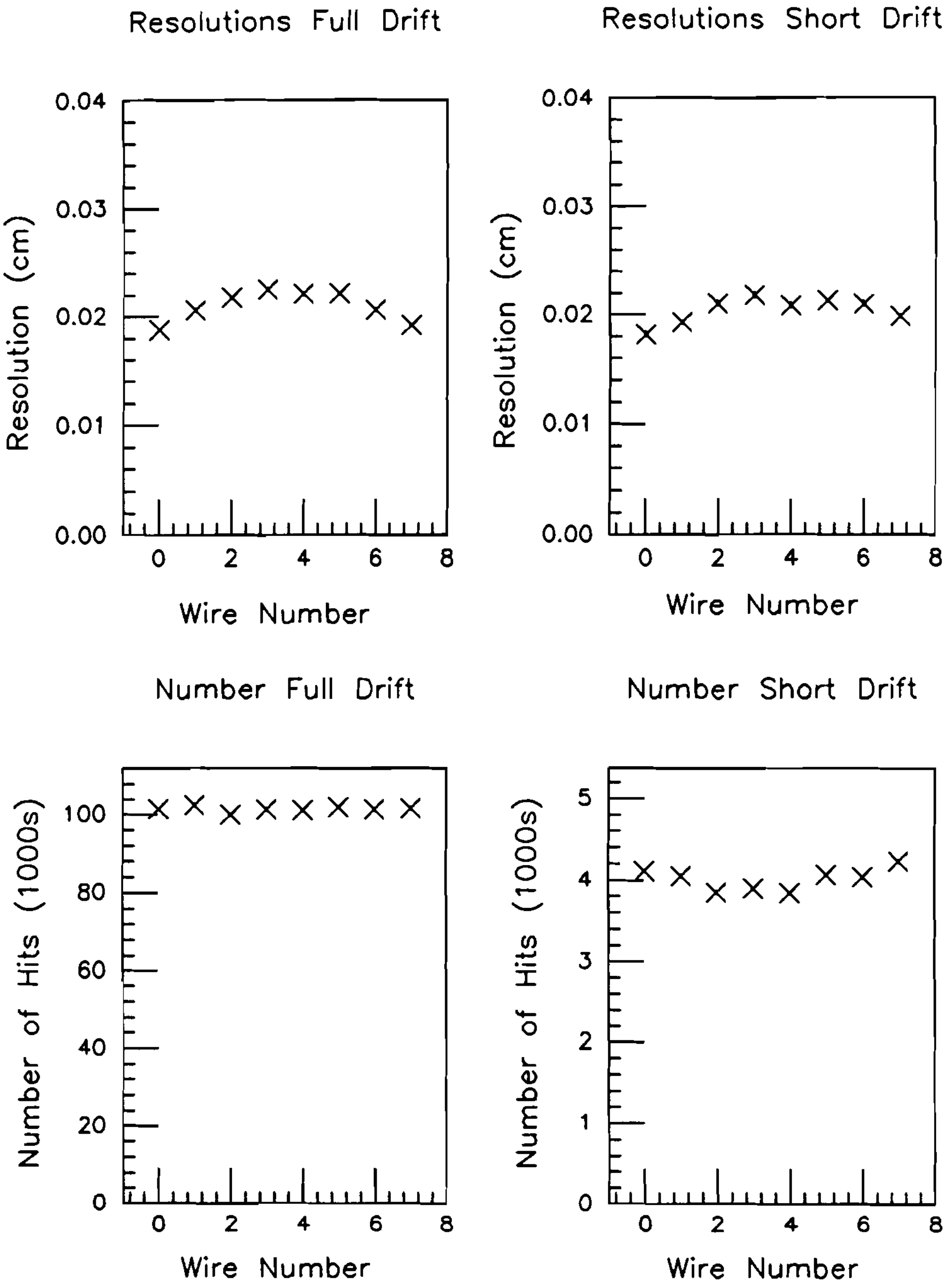

Figure 22: Hit Resolution in a Θ Half Sector for both the full drift side and the short drift side. The resolutions are shown by wire and included are the number of hits used for each wire.

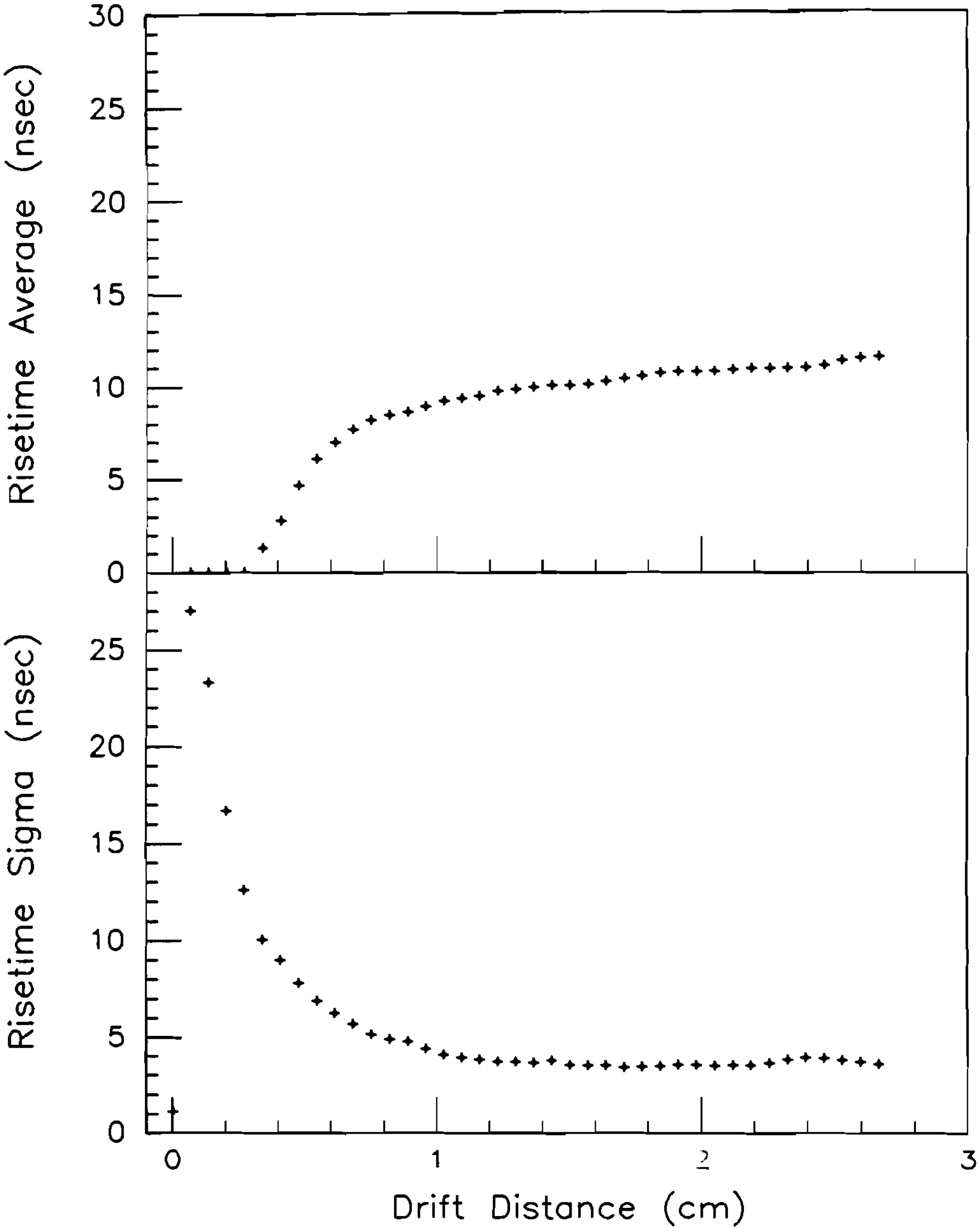

Figure 23: Pulse Risetime Average and Standard Deviation vs Drift Distance for a Φ Sense Wire

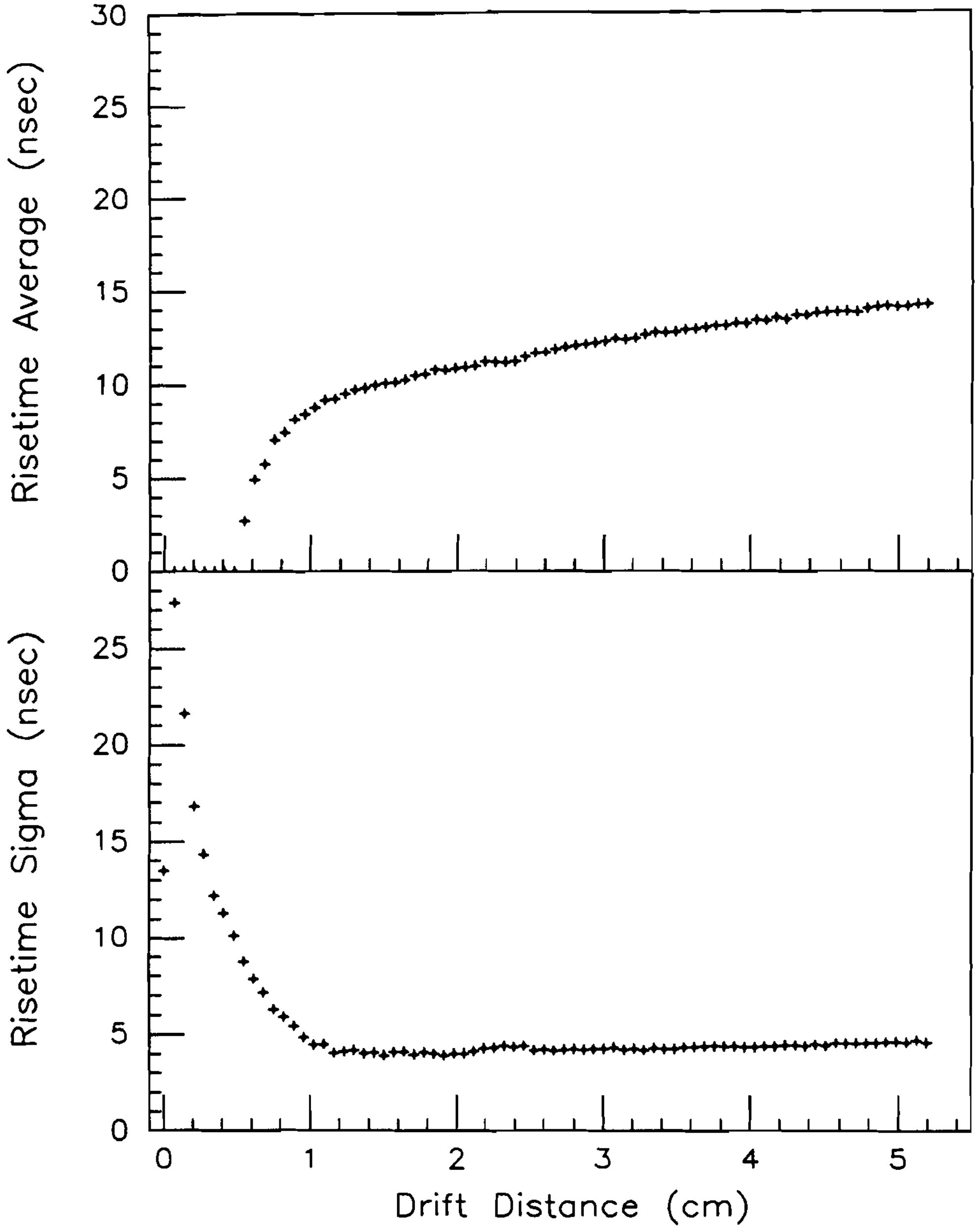

Figure 24: Pulse Risetime Average and Standard Deviation vs Drift Distance for a Θ Sense Wire

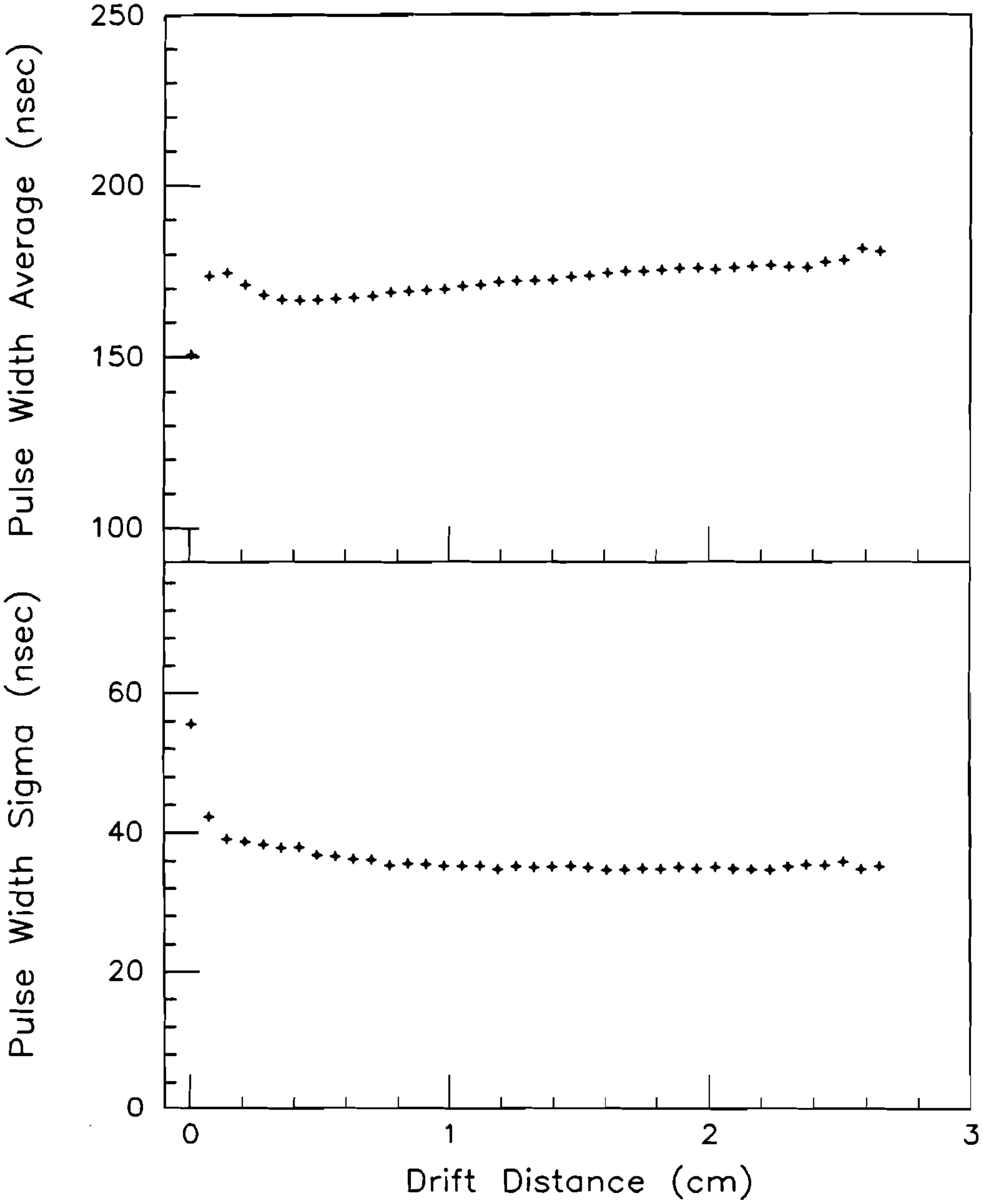

Figure 25: Pulse Width Average and Standard Deviation vs Drift Distance for a Φ Sense Wire

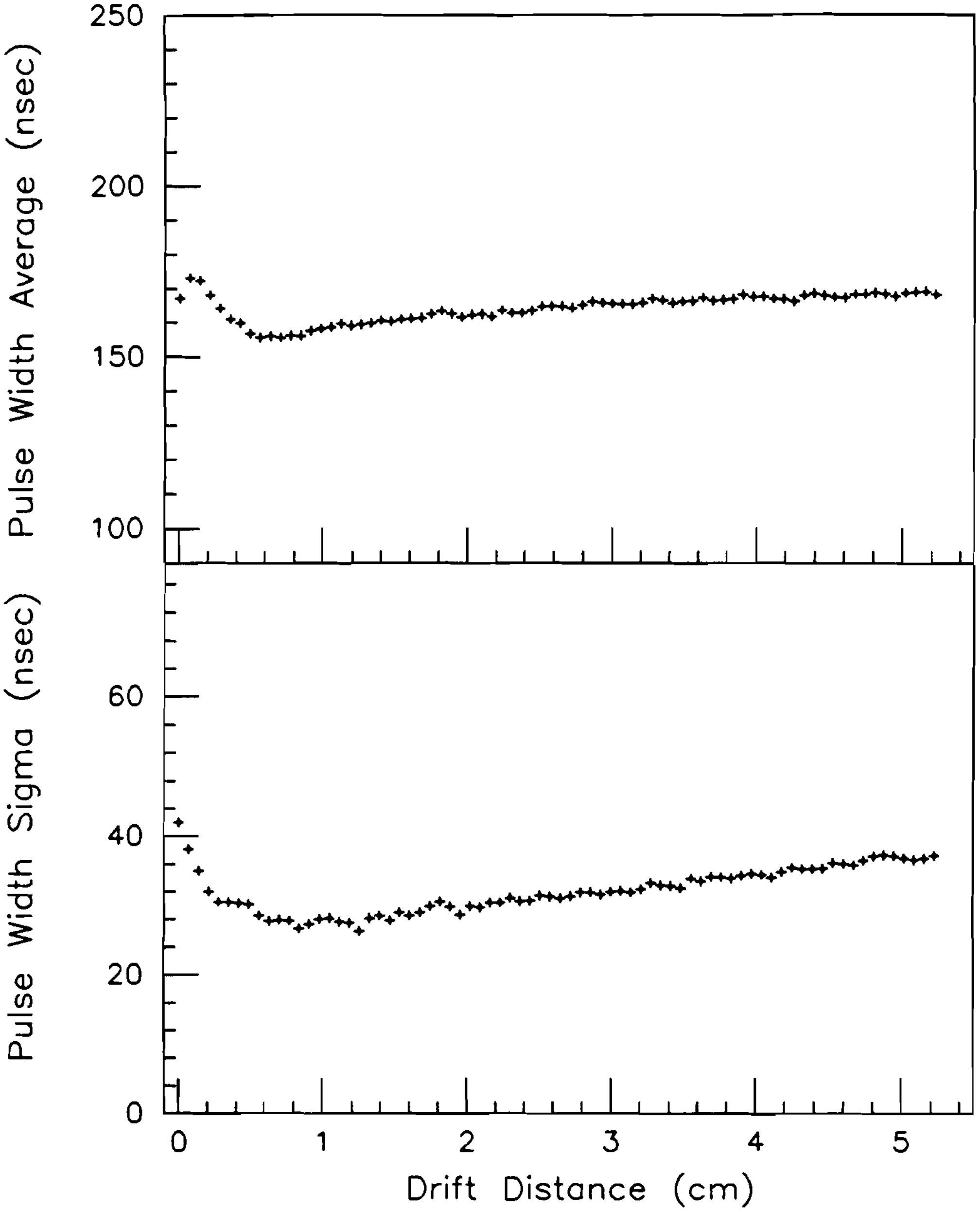

Figure 26: Pulse Width Average and Standard Deviation vs Drift Distance for a Θ Sense Wire

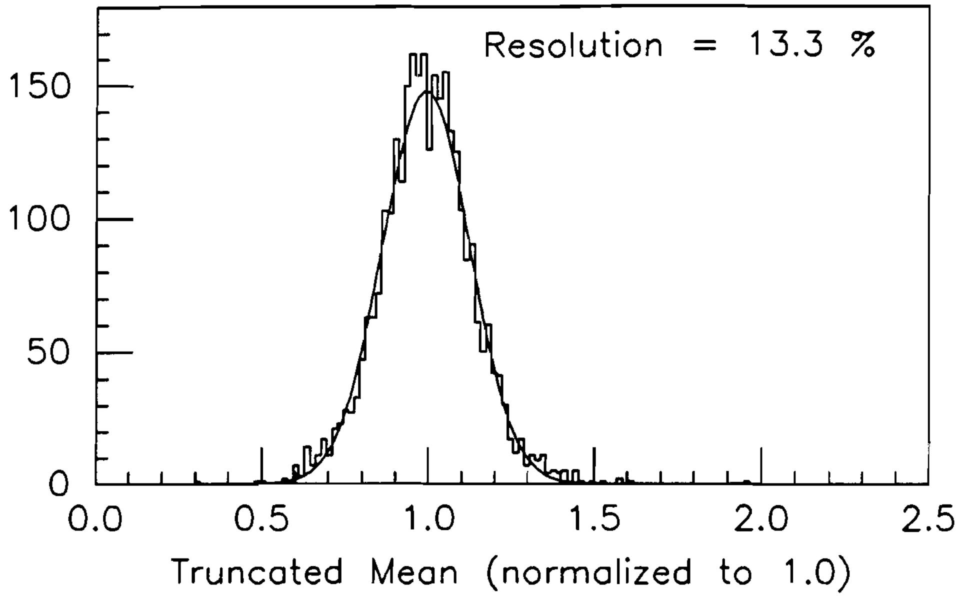

Figure 27: Truncated Mean Pulse Height for Single Pion Tracks

pulse height, the induced pulse on the delay line also increases. This improves both the ability to find the delay line pulse and determine its position along the length of the delay line. Figure 28 shows the effect on resolution and efficiency for a range of sense wire 0 voltage. A vertical dashed line shows a resolution of $0.47\,cm$ and efficiency of 0.92 at the operating voltage of $+1665\,V$.

4.4.6 Crosstalk Correction

The crosstalk correction was mentioned above in Section 4.1.1 and a measure of its success is the reduction in the hit resolution seen when the correction is used. Figures 29 and 30 show the hit resolution for typical Θ and Φ sense wire hits before and after the crosstalk correction is applied. The alternating pattern before the correction is caused by the wire stagger and the selection of tracks only on one side of the sense wire plane. The pulses occurring first at the closer sense wires

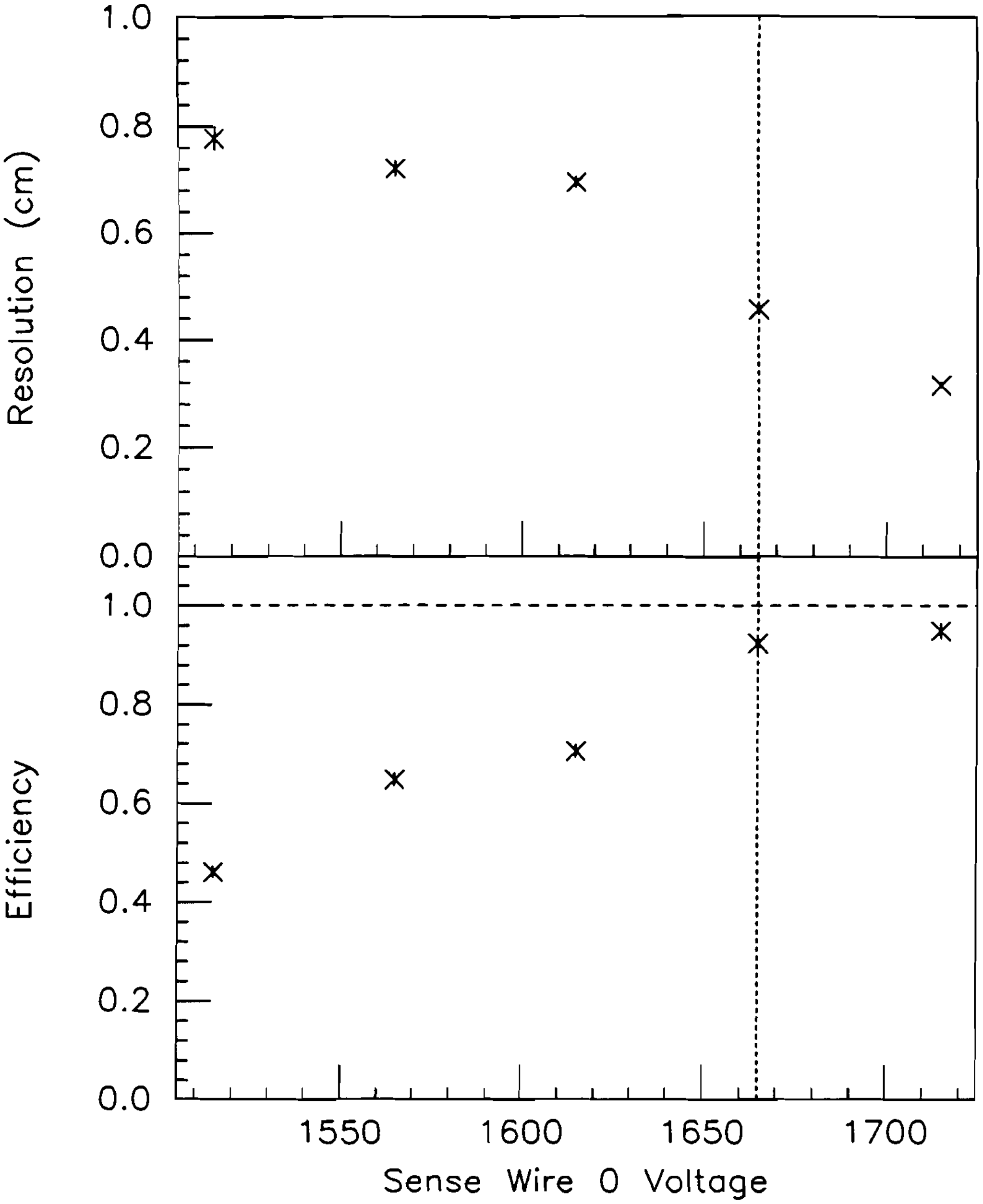

Figure 28: Hit Resolution and Efficiency for a Θ delay line. The dashed line indicates the operational sense wire 0 voltage.

cause a droop in the pulses occurring later which shifts the position of their leading edges later in time and thus increasing the hit residuals.

4.4.7 Two Hit Resolution and Efficiency

The ability of the FDCs to distinguish between two closely spaced pulses on a sense wire depends largely on the pulse shaping, electronic noise, and optimization of the software hitfinding thresholds. The software for the FDC reconstruction has the hitfinding thresholds set low so that every possible hit can be found. Essentially, if the zero-suppression passes along a signal cluster then the hitfinding will also find a pulse at the same leading edge that triggered the zero-suppression. As the results will show, the pulse shaping characteristics will predominately determine the two hit resolution.

To test the two hit resolution, a software package was used that overlapped two adjacent events at the FADC level with the second event delayed behind the first event by a known quantity of FADC samples. The package read in two consecutive events, searched a particular wire in both events, and required exactly one pulse to be found on the wire in each event before the overlapping was performed. The second event's pulse was then overlapped behind the first by a preset amount of time. The overlap method used the times found by the initial check to determine how much to shift the FADC values from the second event with respect to the first event. The FADC sample values were overlapped by first removing the bilinear effect, then subtracting off the pedestal level. The remaining sample values of the second event were then delayed by the proper shift calculated as above including the preset shift. The two events were then added together sample by sample, the pedestal level was added back in and the bilinear effect restored. The resultant FADC channel of samples had two pulses a preset time distance apart. The standard FDC offline reconstruction package was then applied to the resultant FADC channel. See Figure 31 for an example of two hits overlapped by this technique.

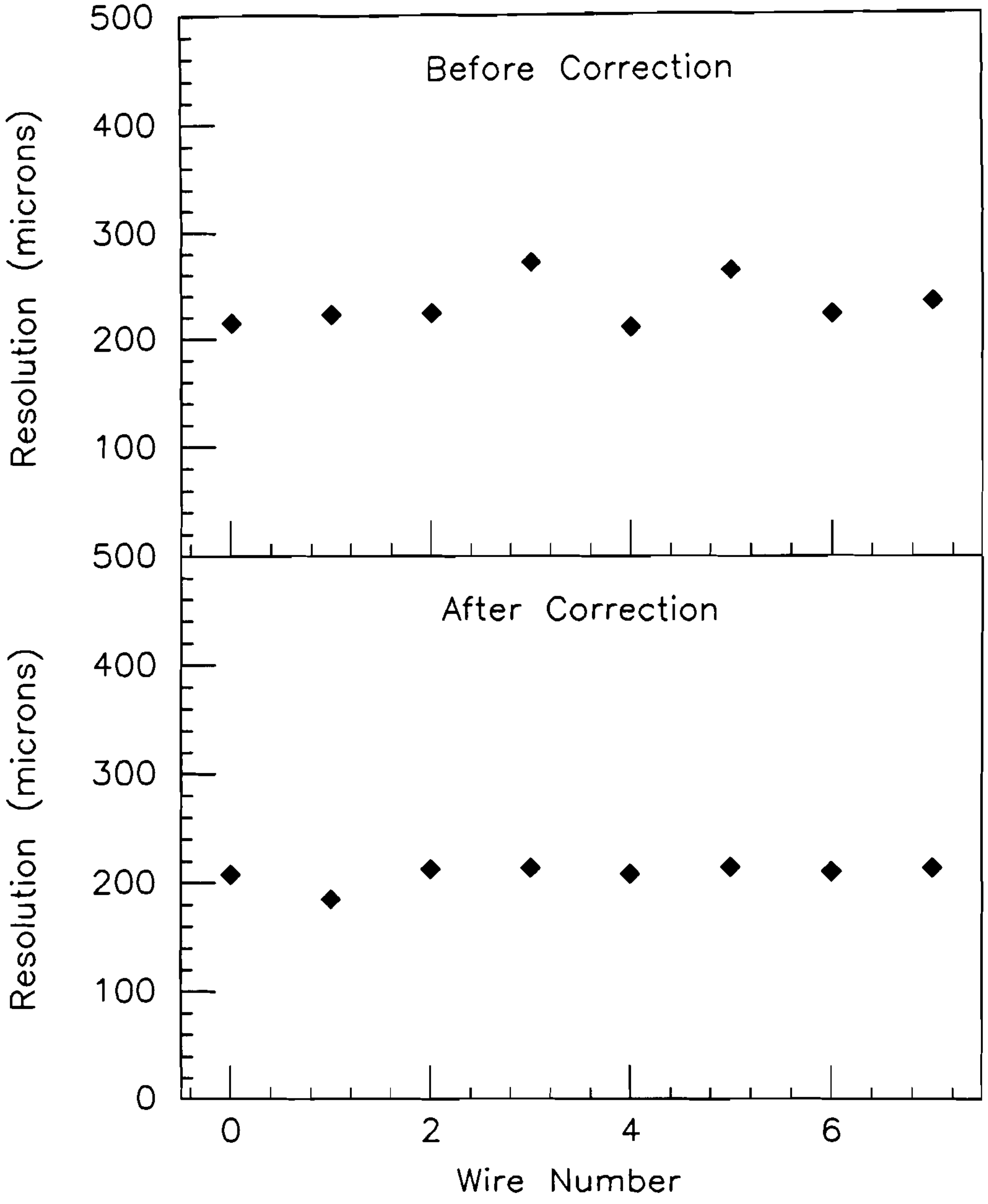

Figure 29: Hit Resolution before and after implementation of the crosstalk correction in a Θ sector.

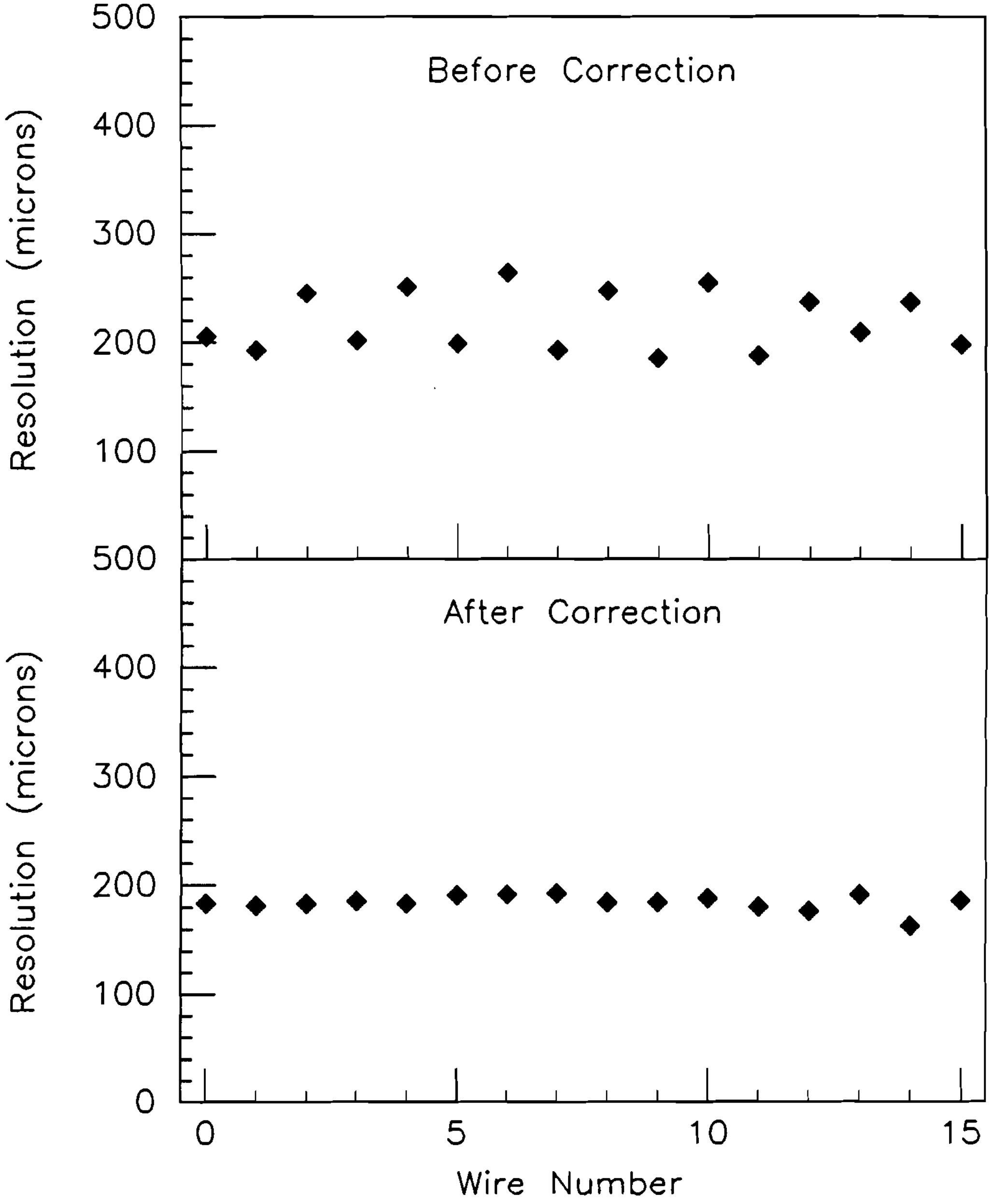

Figure 30: Hit Resolution before and after implementation of the crosstalk correction in a Φ sector.

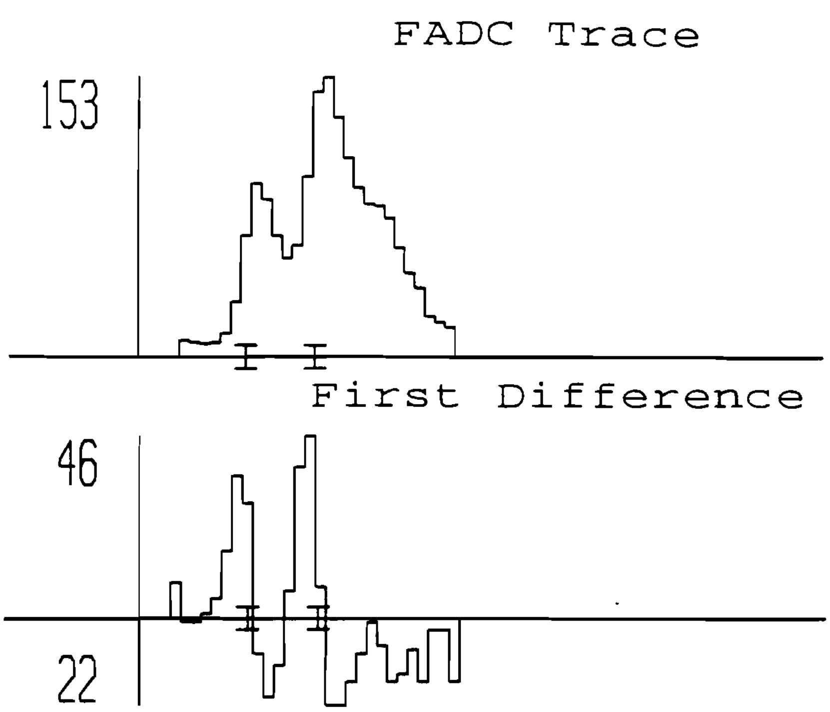

Figure 31: The FADC Trace of Two Overlapped Hits

Two pulses were treated as successfully resolved if two hits were found. An efficiency was obtained by compiling the results of many such overlapped events. A study was done using runs in which the tracks were at different angles to the sense wire plane. Runs were made at increments of 5 degrees from 0 degrees up to 35 degrees for one Θ sector. For each angle run, the events were analyzed for preset pulse separations of 2,3,4,5,6,7,8,9,10,11,12,13,15,17, and 20 FADC samples. Each FADC sample corresponds to 9.434 *nsec*. The efficiency for resolving two pulses as a function of pulse separation at a track angle of 15° is shown in Figure 32. The 70% efficiency level is achieved at a pulse separation of 1.6 *mm* and the 90% efficiency level is achieved at a pulse separation of 3.2 *mm*. See Figure 33 for the resolution versus track angle. The addition of pulse shaping electronics that reduces the length of the pulse tails by 50% provided a marked improvement in the two hit resolution efficiency and eliminated extremely long pulse tails found in the NWA

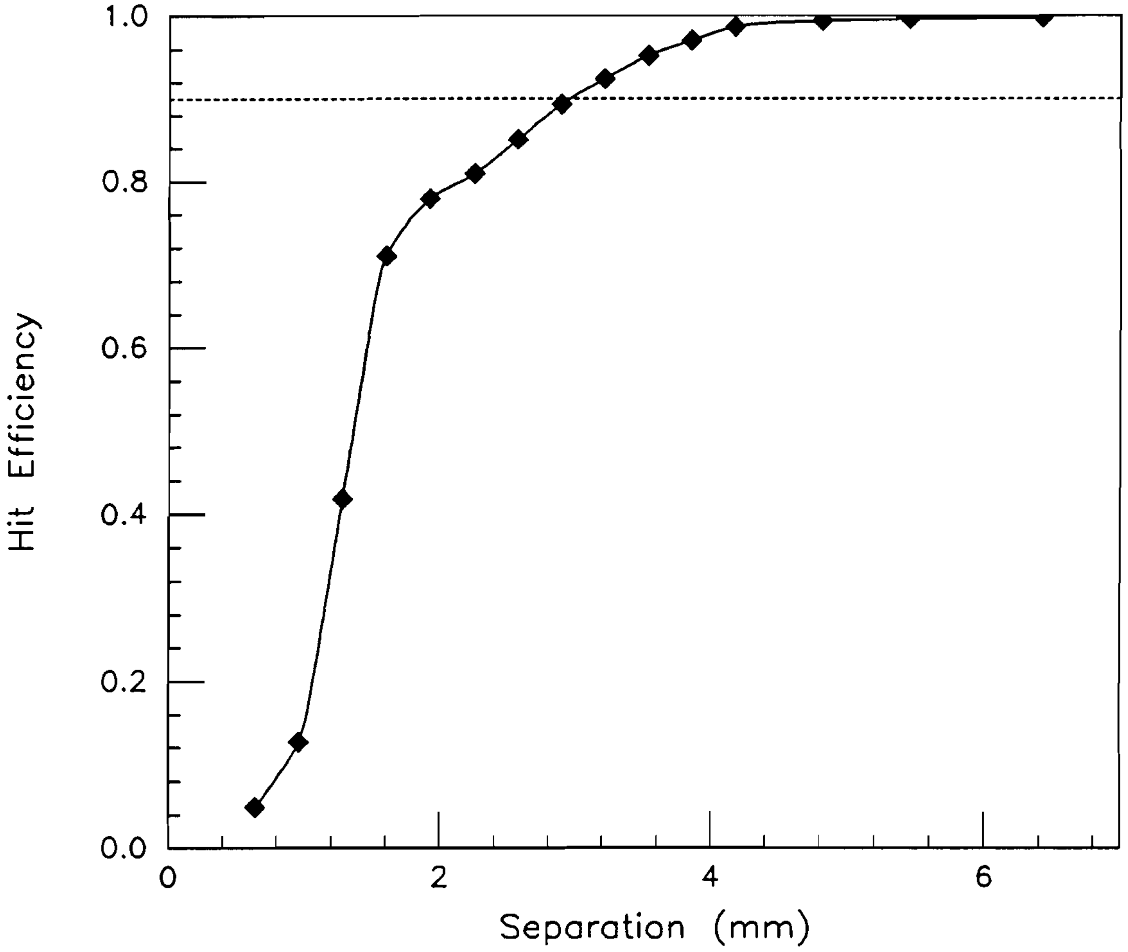

Figure 32: Two Hit Efficiency vs Hit Separation for Track Angle of 15°

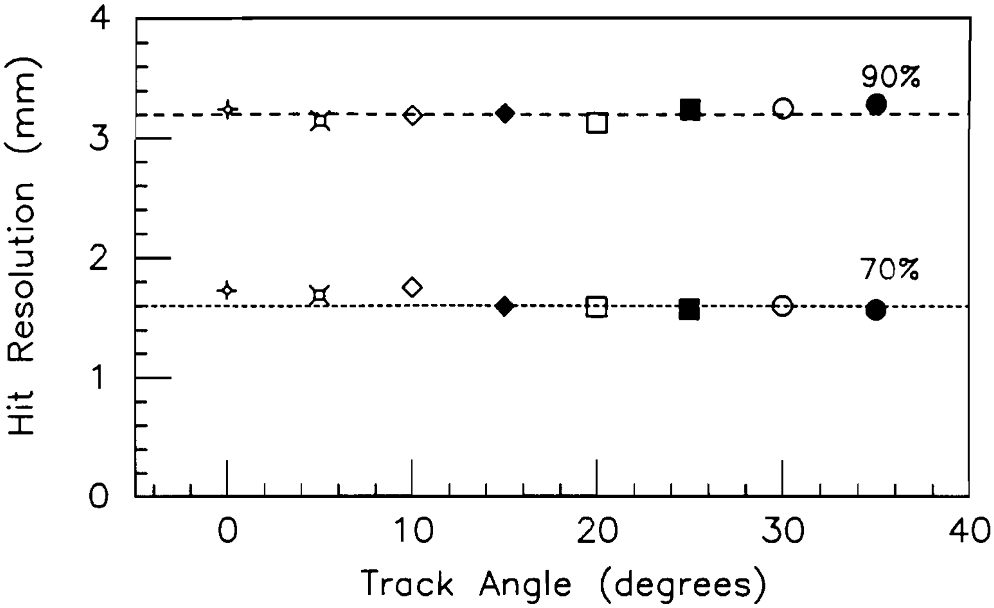

Figure 33: Two Hit Resolution vs Angle

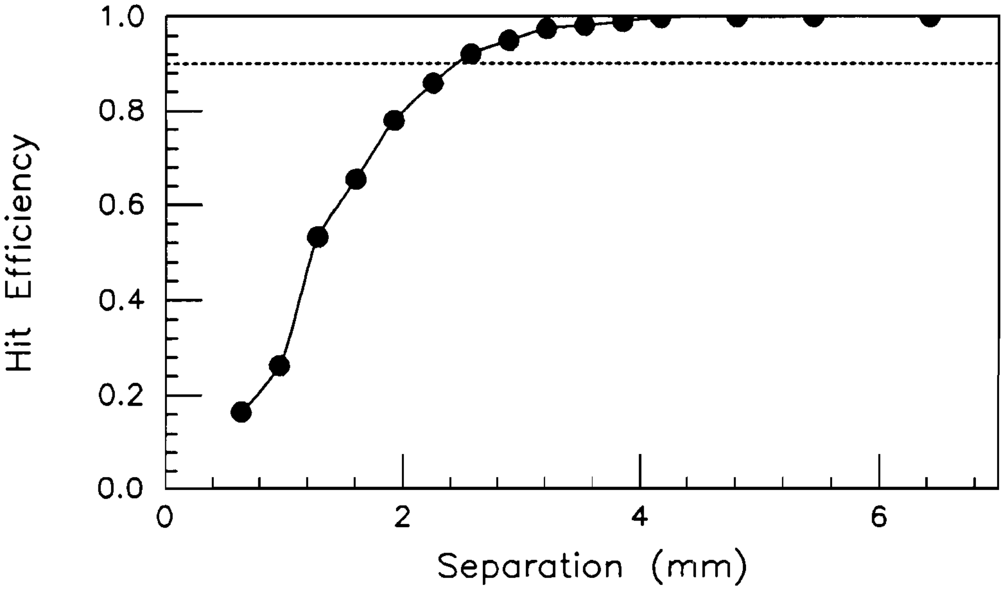

Figure 34: Two Hit Resolution and Efficiency - New Shapers

testbeam run. The results of a study using such shaping are shown in Figure 34. This new shaping which has the 90% efficiency level at a separation of 2.5 *mm* has since been added to all of the FDC pulse shaper headers.

4.4.8 Resolution and Efficiency for Two Closely Spaced Segments

It is important for finding two closely spaced track segments that not only individual hits are found but also enough hits are found to form a proper segment. The study of closely spaced hits has been extended to study complete segments. For segments, the FADC data for an entire Θ sector from one event is overlapped with the appropriately delayed FADC data from a second event. The amount of delay was determined by the pulses on one particular middle wire from the two adjacent events. Since it was necessary to assure that the full segments found in each separate event would overlap correctly for all wires, an additional requirement was set. The outermost wires are required to have their pulses' time within 5 FADC samples of each other. That is, the two pulses on sense wire 0 from the two events must have a time difference in FADC samples within the time difference of the two pulses on sense wire 7. This assures that the full segments from the two events are reasonably parallel. One major problem that was eliminated by this requirement was the segments from the two events being on opposite sides of the sense wire planes. Their FADC pulses would then cross like an X instead of being parallel. The two segments were always found in these cases because most of the pulses were not near each other and were certainly not at the preset separation. An example of the problem overlap is shown in Figure 35. The results of the two segment separation resolution and efficiency are shown in Figures 36 and 37. The 70% efficiency level is achieved at a segment separation of 2.1 *mm* and the 90% efficiency level is achieved at a segment separation of 2.9 *mm*. This new shaping which has the 90% efficiency level at a separation of 2.7 *mm*.

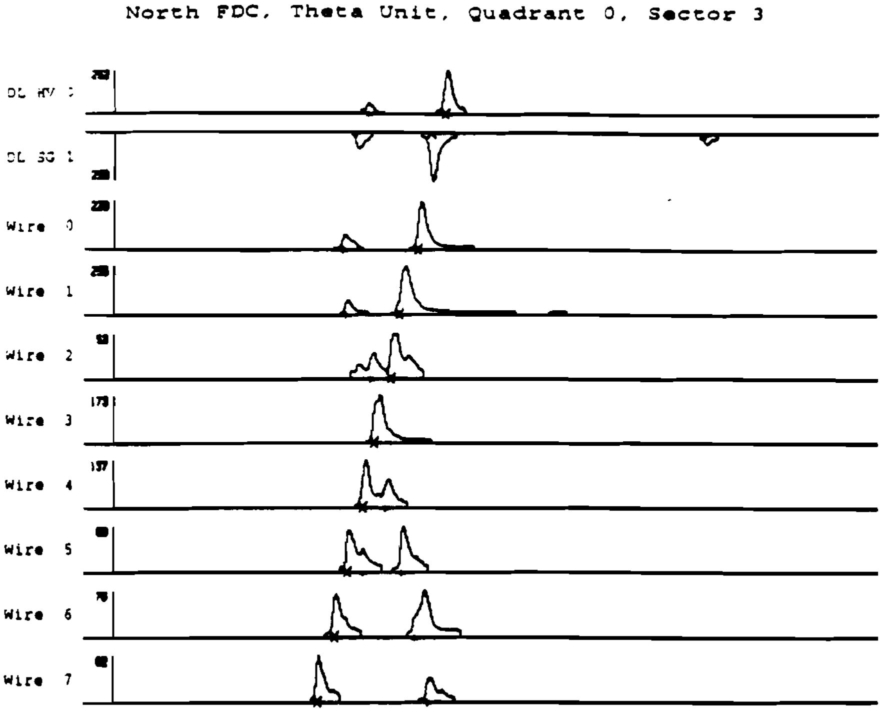

Figure 35: FADC Trace Showing the Problem Overlap of Segments

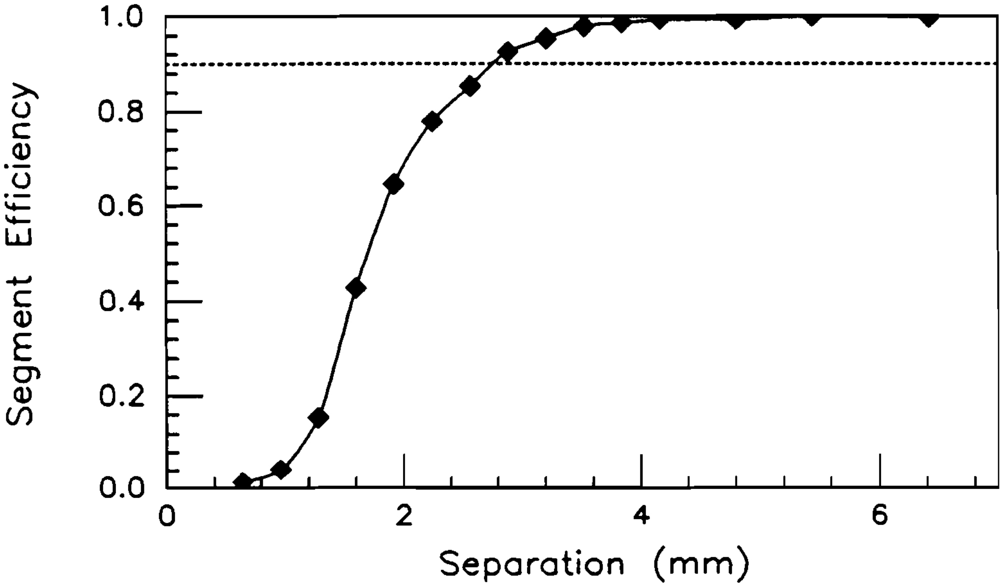

Figure 36: Two Segment Efficiency vs Angle

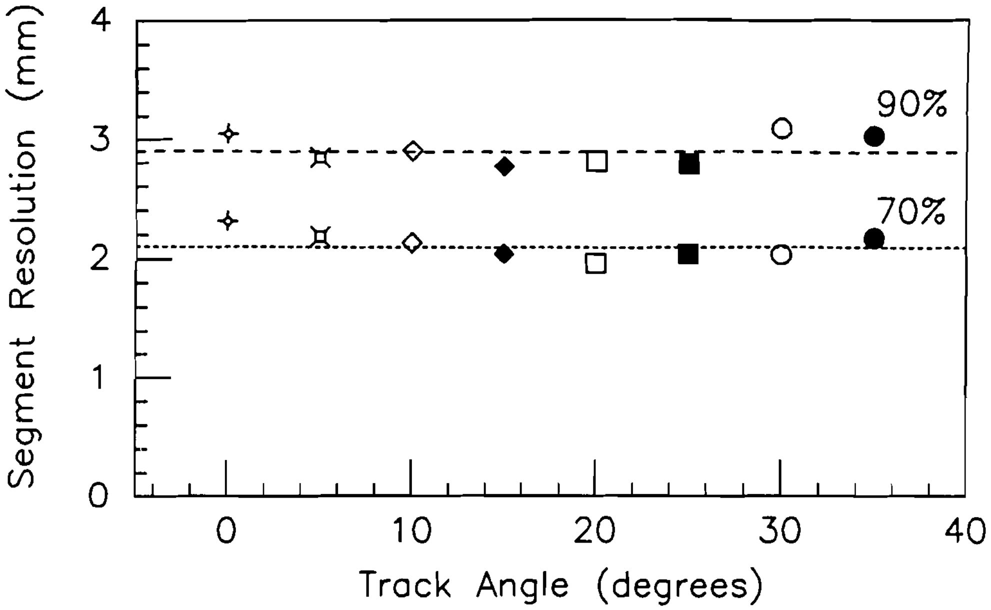

Figure 37: Two Segment Resolution vs Angle

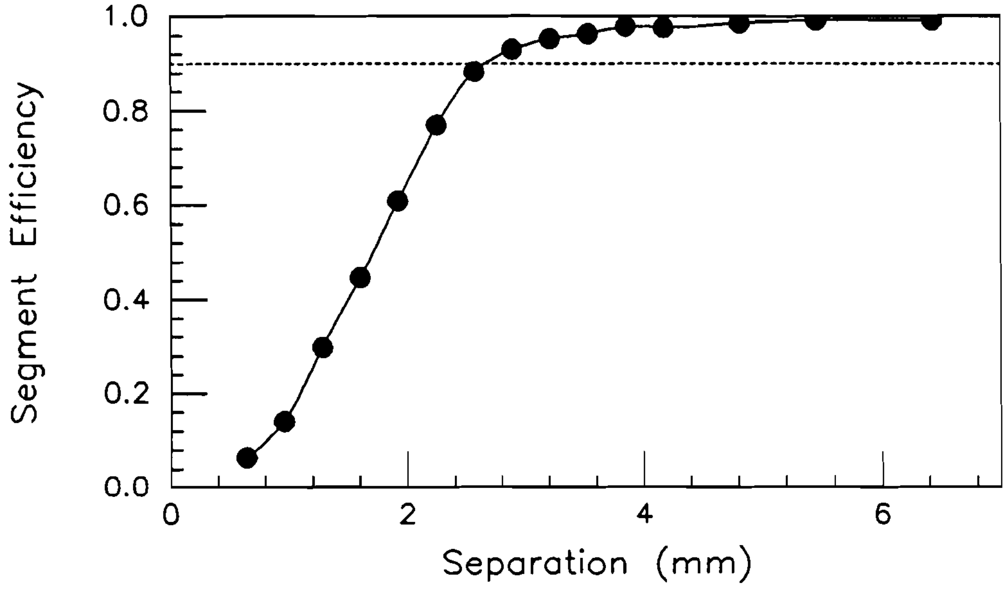

Figure 38: Two Segment Efficiency - New Shapers

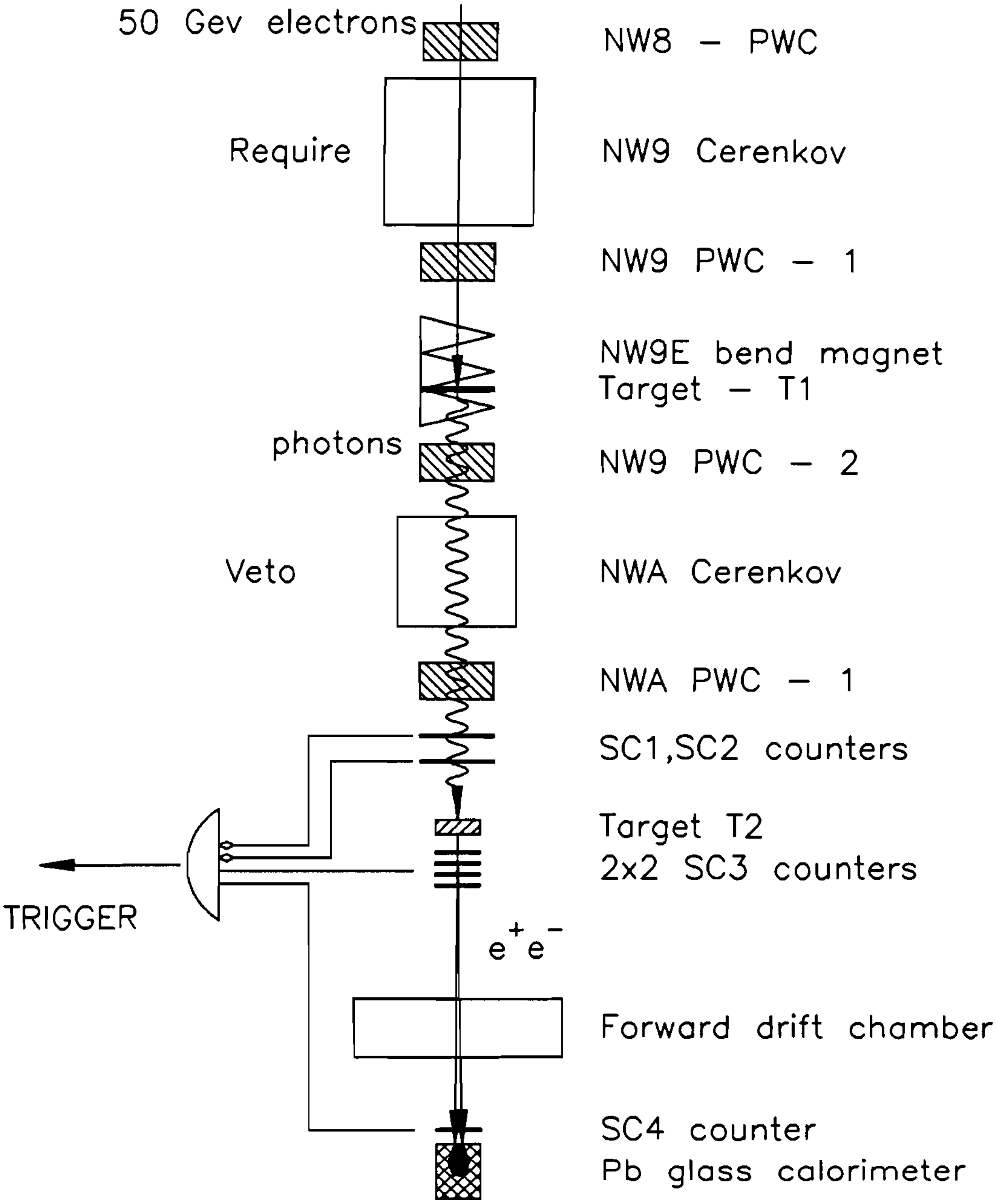

Figure 39: Beamline for Photon and Conversion Pair Generation

4.4.9 Two Track Resolution and Efficiency

The two track resolution and efficiency were done using a very different method than the two hit or two segment method. A beam of high energy photons was created in the NWA beamline and aimed at a lead target. The resultant e^+e_- conversion pairs were tracked through the FDC chamber. Single tracks in the chamber were used for dE/dx measurements whose results are contained elsewhere [11] and the higher multiplicity events were used for the two track separation.

The original beam was a $50\,GeV/c$ electron beam as detailed earlier in Section 3.1. In front of the last magnet, a lead sheet was placed in the beam. See Figure 39.

The electrons would bremsstrahlung creating photons which would continue towards the NWA area. The electrons would be swept away by the remaining NW9E bend magnet. The Čerenkov detectors were set to detect passing electrons. The NW9 Čerenkov was required to fire indicating an incoming electron and the NWA Čerenkov was used as a veto to eliminate any remaining electrons. The photon beam trigger was arranged to require a neutral particle upstream of the Pb target and at least one charged particle downstream of the target. This process created a photon beam whose energies ranged from very low energies up to the $50\,GeV$ of the original electron. The spectrum of photons created by bremsstrahlung is expected to follow an inverse momentum distribution. The lead target used to convert the photons was 0.277 radiation lengths thick. An additional detector was used in the trigger. A lead glass detector was placed after the FDC chamber to measure the energy of the conversion pair.

To determine two track resolution, events containing two or more tracks were analyzed for the separation between all possible pairs of tracks. The distance of separation of the two tracks was calculated using the track reconstruction information. The position chosen was the position of the sense wire nearest the target, the inner Θ sense wire 7. This would be roughly $105\,cm$ from the target. The closest pair of tracks for each event was retained as a part of the event sample. A

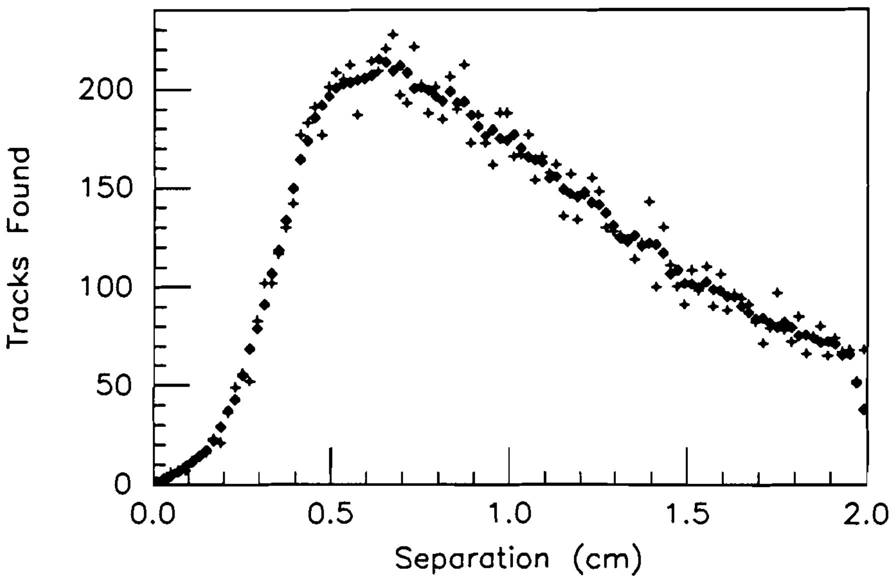

Figure 40: Two Track Separation Data

cut was applied to eliminate all pairs in which at least one of the tracks had an average ionization per hit greater than that of one minimum ionizing particle. The tracks were required to average less ionization per hit than 1.5 times the average ionization per hit of singly ionizing tracks. The qualifying track pairs were expected to be e^+e_- pairs. The distribution of the separation distances was smoothed using a technique which set the value of the current sample equal to one-fifth of the total of the current sample and its neighboring samples, two on each side. This technique is not standard but smoothed the data effectively as shown in a plot of the original data and the smoothed data in Figure 40. If each sample is divided by the value of the peak sample, the 90% and 50% efficiency distances for two track separation can be obtained. The distribution of efficiency using this method is shown in Figure 41. At 90% efficiency the two track separation is $4.8\,mm$ and at 50% the two track efficiency is $3.3\,mm$. These values are greater than the two hit and the two segment separation because of the different orientations of the Θ and Φ chambers. Two tracks

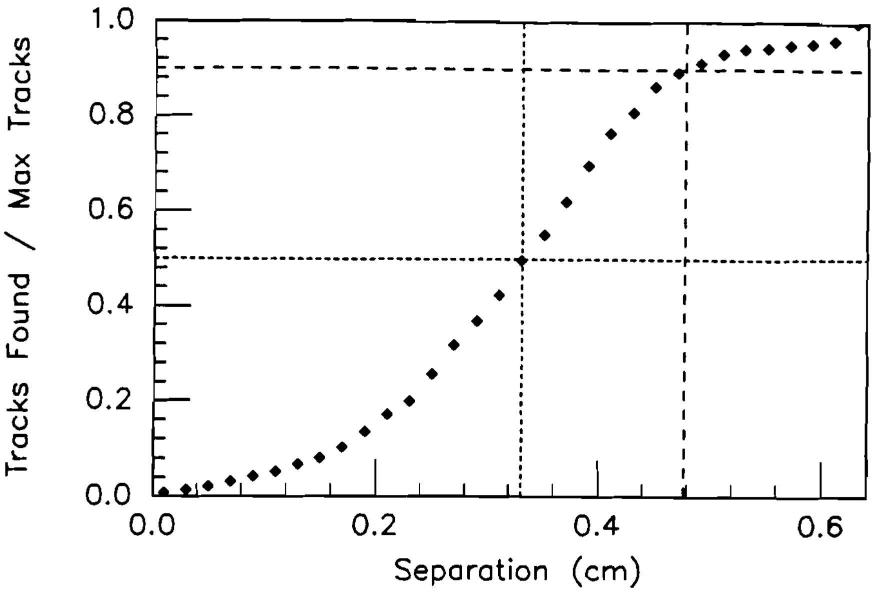

Figure 41: Two Track Separation Efficiency

that are maximully separated in the Φ layer are at most separated by $1/\sqrt{2}$ of the separation in both of the Θ layers.

A study of two track separation was performed using Monte Carlo-generated data. Using the D0 version of the GEANT Monte Carlo program, a full simulation of the NWA testbeam area was made. A beam of photons was created with various energies and passed through the simulation. The Monte Carlo generated event output that was a duplication of FADC output from the FDC. Thus, an identical reconstruction analysis to the real data analysis could be performed on the Monte Carlo output. One Monte Carlo event sample started with a beam of photons whose energies were distributed between $10\,MeV$ and $50\,GeV$ with numbers of photons for a given energy $N(E)$ falling as $1/E$, the typical bremsstrahlung spectrum. Using a smoothing technique as above, the 90% efficiency separation was $3.0\,mm$ and the 50% efficiency separation was $2.2\,mm$. The original and smoothed data are shown in Figure 42 and the distribution of efficiency is shown in Figure 43.

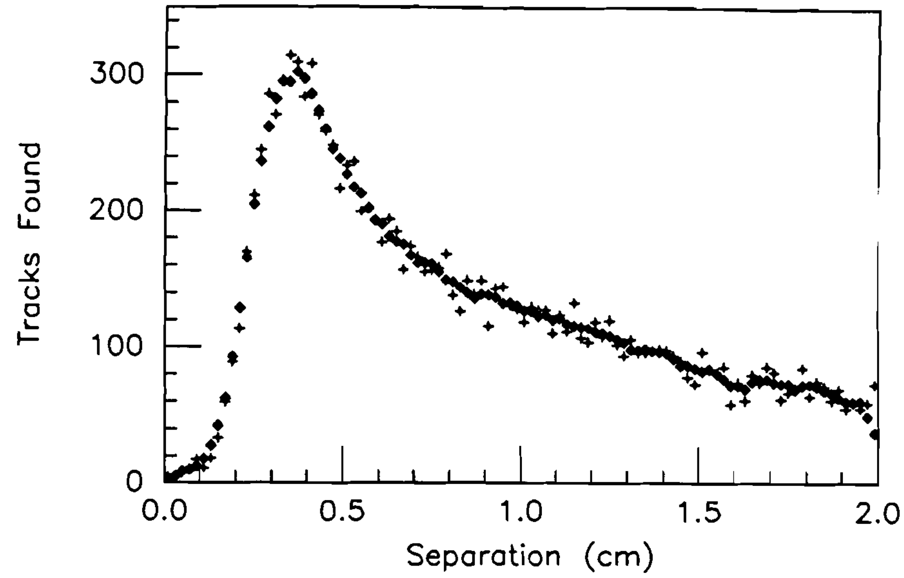

Figure 42: Two Track Separation Monte Carlo Data

The real data and Monte Carlo data distributions differ in two ways. The Monte Carlo two track separation is better than that for the real data. This is due to the narrower pulse shape used in the Monte Carlo and the lack of noise simulation. A comparison of the two average shapes is shown in Figure 44. An improved Monte Carlo pulse shape will be used based on the new shaper components.

The second mismatch in features of the two track data distributions is the much greater peak at small separations evident in the Monte Carlo data only. This greater peak is most likely due to greater numbers of high energy photons being used in the Monte Carlo sample. Several different Monte Carlo data runs were generated with photon energies preset to $0.1, 0.2, 0.5, 1, 2, 5, 10, 20$, and $50\,GeV$, one energy per run. The two track separation distributions from the $2\,GeV$ and $50\,GeV$ runs are shown in Figures 45 and 46. The high peak is only present in the $50\,GeV$ sample and the $2\,GeV$ sample resembles the data more closely. An attempt was made to model the real data

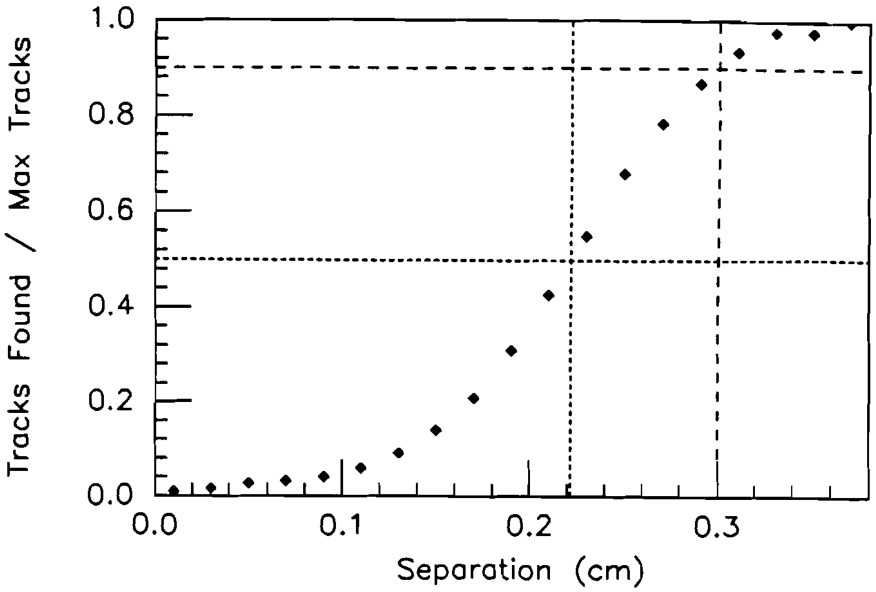

Figure 43: Two Track Separation Efficiency - Monte Carlo

photon spectrum more accurately but there was always a mismatch at either the closer separation distances or at the wider $(2 - 5\,cm)$ separations. Additionally, the lead glass detector was not adequate to aid in modelling the spectrum.

4.5 Summary

The most important calibration results of the testbeam were the basic ones. Although the electron drift field is not the same for the Θ and Φ chambers due to differences in geometry and guard wire configuration, their overall performance is similar. The linear drift time to drift distance relation greatly simplifies track reconstruction in the chambers. With typical drift velocities of $34\,\mu m/nsec$, the maximum drift distances in both Θ and Φ chambers are traveled in less than $1.6\,\mu sec$. As a part of the DØ detector, this is less than half of the expected time between collider interactions of $3.6\,\mu sec$ so that interference from a previous event will not exist. Being able to monitor the

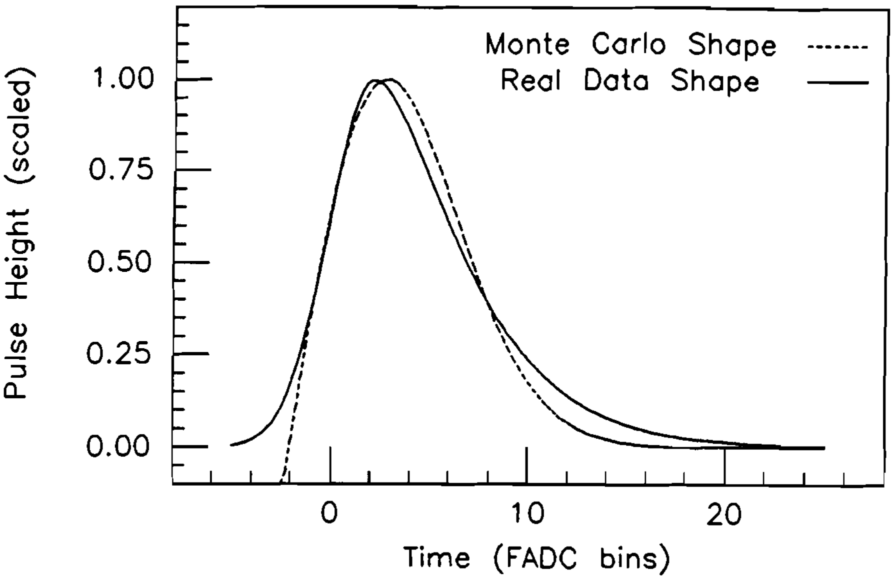

Figure 44: Pulse Shape Comparison - Real Monte Carlo

daily variations with the FDC Canary will provide constant updating to maintain accuracy. This accuracy yields single hit resolutions of $\approx 170\,\mu m$ in the Φ sectors and $\approx 210\,\mu m$ in the Θ sectors. The θ and ϕ direction measurements are two independent, orthogonal measurements of the charged particle track position. The pulse height measurements for track dE/dx calculations has a resolution of 13.3% for 75% truncation. The delay line resolution of $0.47\,cm$ at 92% efficiency provides vital additional information in matching segments between layers. The two hit, two segment, and two track resolution and efficiencies are shown in Table 2. The results are from data using the old shaper components and the new shaper components. Since the reconstruction software parameters were optimized for the older data, it is hoped that optimization of parameters for the new shapers will come with additional experience and use.

The chambers overall performance provided great confidence in its capabilities in its final job as the D0 Detector's forward tracking chambers.

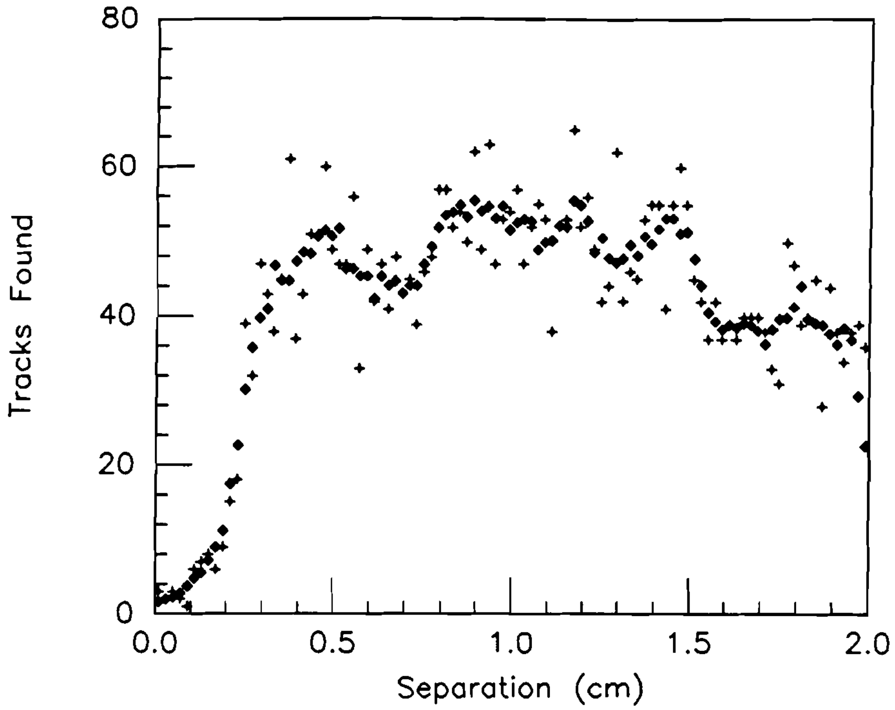

Figure 45: Two Track Separation Data - 2 GeV MC Sample

	Separation (mm)		
	Efficiency		
Type	50%	70%	90%
Two Hit	-	1.6	3.2
Two Segment	-	2.1	2.9
Two Track	3.3	3.9	4.8
Two Hit - New	-	1.7	2.5
Two Segment - New	-	2.1	2.7

Table 2: Separation Results Summary

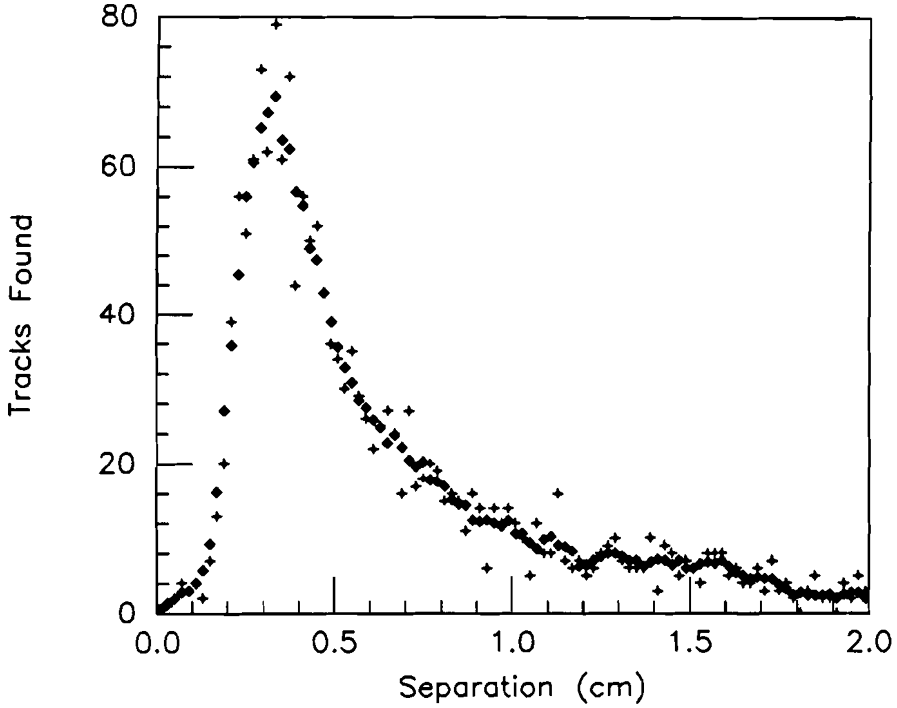

Figure 46: Two Track Separation Data - 50 GeV MC Sample

5 Target Runs and Results

5.1 Basic Goals

The testbeam at NWA provided an opportunity to study the ability of the FDCs in a high rate, multi-track per event environment. A series of data runs were made with the FDC in an angled position and a range of targets from beryllium to lead was placed in a π^- beam. The chamber was aligned so that the target was at a position equivalent to the exact center of the D0 Detector's interaction region. The wide range in atomic mass of the targets permitted a study of the elastic diffractive scattering nuclear slope which is a function of A. For each target, a run was taken at beam momenta of $10\,GeV/c$, $50\,GeV/c$, and $150\,GeV/c$. This range in momenta for the incident pions also allowed the study of charged track multiplicity. Although results for these processes have been obtained by more sophisticated detectors over similar momentum ranges, it is useful to try to use the Forward Drift Chambers in such experiments to push its capabilities as much as possible and in so doing, perhaps, better understand its limitations.

5.2 Charge Track Multiplicity

5.2.1 Basic Theory

Studying the number of charged particles tracks coming from an interaction is a basic analysis that has been performed in bubble chambers [26] [27] and counter [28] [29] [30] experiments. With these kinds of detector systems, it was very easy to count the number of charged prongs that emerged from an interaction point from an inelastic collision occurring in the detectors. Each prong was an individual charged particle and the total number of prongs for an interaction was called the charge particle multiplicity denoted by N_{ch} . The inelastic cross section for the production of final states with N_{ch} charged prongs is called the topological cross section denoted by $\sigma_{top}(N_{ch}, s)$ where s is the square of the total center of mass energy, E^{cms}. Previous results [31] have shown that the topological cross section rises quickly but flattens out as the energy increases. Thus at high energies, the low N_{ch} topological cross sections are decreasing while the higher multiplicity ones are small but increasing quickly. Although the exact relationship between $\langle N_{ch}\rangle$ and E^{cms} is not known, the relation can be represented by a power law

$$\langle N_{ch}\rangle = c\,s^{n} \tag{10}$$

or by a logarithmic law

$$\langle N_{ch}\rangle = a + b\ln s \tag{11}$$

These relations are simple functions that characterize the trends of N_{ch} as found in "fireball" [32], "multiperiphal" [33] [34], and "diffractive" [35] [36] models. One fundamental model is based on thermodynamics and assumes that N_{ch} is high enough to allow application of thermodynamical considerations to the final state. An early treatment of this idea is given by Fermi [37]. It is assumed that all final state particles are pions, positive, negative, or neutral, and that each charge state has an equal probability. Further, the pions are considered as a gas confined in a volume Ω fixed by the range of the strong interactions and so approximately,

$$\Omega \approx \left(\frac{\hbar}{m_{\pi}c}\right)^{3} \tag{12}$$

where m_{π} is the pion mass. The total energy confined in Ω is the total energy E^{cms} in the center of mass. The pions are also considered extremely relativistic so that their mass is negligible.

The statistical mechanics of massless pions is very similar to the statistical mechanics of photons in that they both obey Bose-Einstein statistics. From Planck's black-body distribution law, the most probable number of photons per unit frequency per unit volume is,

$$\frac{dN(\nu)}{d\nu} = \left[\frac{8\pi\nu^{2}}{c^{3}}\right]\left[\frac{1}{e^{h\nu/KT}-1}\right] \tag{13}$$

where ν is the frequency and K is the Boltzmann constant. To substitute the use of pions, one notes that a photon of fixed energy has two available spin states and a pion has three available charge states. Using this information and letting $2\pi\hbar\nu \rightarrow E$, the energy of the pion,

$$\frac{dN(E)}{dE} = \frac{3}{2}\left[\frac{E^2}{\pi^2\hbar^3c^3}\right]\left[\frac{1}{e^{E/KT}-1}\right] \tag{14}$$

Integrating the right hand side for $0 \leq E \leq \infty$, one obtains the total number of pions per unit volume in the most probable distribution. One can use simple thermodynamic arguments to equate this to $\langle N_{ch}\rangle$, the average total number of pions per unit volume for all the different distributions. Setting $\hbar = c = 1$ and integrating,

$$\langle N\rangle = \frac{3.60}{\pi^2}(KT)^3 \tag{15}$$

To find the temperature T, one calculates U, the total energy per unit volume,

$$U = \int_0^\infty \left[\frac{3E^3}{2\pi^2}\right]\left[\frac{1}{e^{E/KT}-1}\right] dE \tag{16}$$

Integrating,

$$U = \frac{9.74}{\pi^2}(KT)^4 \tag{17}$$

Also noting that $9.74/\pi^2 \approx 1$ and that U is also given by,

$$U = \frac{E^{cms}}{\Omega} \tag{18}$$

Combining, one obtains,

$$(KT) = 1.00\left[\frac{E^{cms}}{\Omega}\right]^{1/4} \tag{19}$$

Using this value for (KT),

$$\langle N\rangle = 0.36\left[\frac{E^{cms}}{\Omega}\right]^{3/4} \tag{20}$$

Therefore the end result is,

$$\langle N_{ch}\rangle = (constant)\,(E^{cms})^{0.75} \sim c\,s^{0.375} \tag{21}$$

This simplistic result is in crude agreement with experiment including this one (see Figure 53). Elaborations of the model have been made and implemented in statistical models that are combined with the forward dominance concept. These "fireball" [32] and "nova" [38] models provide a better treatment of the physical process and at high s obtain a logarithmic law solution. One such result [27] fits bubble chamber data of $\pi^- p$ interactions to obtain the solution

$$\langle N_{ch} \rangle = 0.59 + 0.81 \cdot \ln\, s + 0.074 \cdot \ln^2\, s \tag{22}$$

The results for a carbon target are expected to be higher [29] because of the presence of the additional nucleons.

5.2.2 Experimental Limitations and Results

The NWA angled position of the FDC allowed it to cover a cone for forward going tracks of angle 0.20 radians ($\approx 11.3^\circ$). Therefore, not all of the charged particle tracks were seen but due to the high momentum of the incident beam pion, the relativistic effect folds the center of momentum (CMS) frame forward in the laboratory (LAB) frame and thus increases the acceptance with the increasing beam momentum. Table 3 shows the relevant parameters for each of the three momenta where the data was taken. A direct calculation of acceptance is difficult because the momentum of the particles emerging from the interaction could not be measured. This would not be necessary in a bubble chamber experiment where one can just count up the number of emerging prongs from the interaction for a full 4π acceptance. For this setup, correcting for the geometrical acceptance and extrapolating the lowest energy beam data allow the acceptance to be extended to 90° in the CMS frame. Doubling these results would achieve full acceptance. A simple calculation using the Lorentz transformation given below

$$\tan(\theta^{lab}) = \frac{p^{cms} \cdot \sin(\theta^{cms})}{\gamma \cdot p^{cms} \cdot \cos(\theta^{cms}) + \beta \cdot \gamma \cdot E^{cms}} \tag{23}$$

Parameter	π^- Momentum 10 GeV/c	 50 GeV/c	 150 GeV/c
E^{lab} (GeV)	10.001	50.00	150.00
E^{cms} (GeV)	4.436	9.735	16.810
β^{cms}	0.914	0.982	0.994
γ^{cms}	2.466	5.233	8.979
s (GeV^2)	19.68	94.77	282.6
$\ln s$	2.98	4.55	5.64
$s^{0.375}$	3.06	5.51	8.30

Table 3: Center of Momentum Frame Parameters

allows one to calculate the particle angle with respect to the incident particle direction in the LAB frame given a π^- emitted at 90° in the center of momentum frame. The range of π^- momenta used was from $10\,MeV$ up to the maximum possible momentum allowed in the CMS frame. This value is determined by considering the incident pion and target nucleon in the CMS frame. The maximum momentum the pion can obtain is when no other particle is created and the pion and nucleon are emitted back to back with equal but oppositely directed momentum. Total energy in the center of momentum can then be written

$$(E^{cms})^2 = (E^{cms}_{\pi^-} + E^{cms}_N)^2 \tag{24}$$

$$(E^{cms})^2 = (\sqrt{(p^{cms})^2 + (0.1395\,GeV)^2} + \sqrt{(p^{cms})^2 + (0.939\,GeV)^2}\,)^2 \tag{25}$$

Numerical analysis can provide the pion CMS momentum given a fixed value for the CMS energy. Table 4 shows the results for all three beam momenta. Using the listed maximum CMS pion momenta values, the results of the calculation for the laboratory angle given a 90° angle of emission in the CMS frame are shown in Figure 47. The lab frame angle is within 10% of the maximum angle for all π^- CMS momenta above $\approx 300\,MeV$. Assuming any emitted particle is a pion and

	π^- LAB Momentum		
Parameter	10 GeV/c	50 GeV/c	150 GeV/c
E^{cms} (GeV)	4.436	9.735	16.810
Max p^{cms} (GeV/c)	2.117	4.822	8.378
Max $E^{cms}_{\pi^-}$ (GeV)	2.122	4.824	8.379
for $\theta^{cms} = 90^\circ$			
θ^{lab} (rad)	0.417	0.192	0.121
θ^{lab} (deg)	23.90	11.01	6.39
Dist from beam at FDC (cm)	46.69	20.50	11.81

Table 4: Center of Momentum π^- Parameters

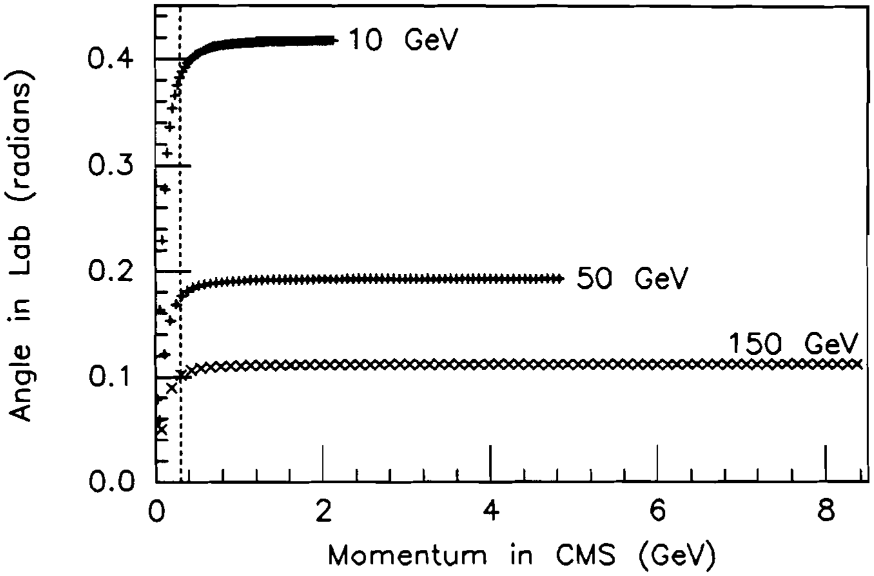

Figure 47: LAB Angle vs CMS 90° Emission Momentum

it has a momentum greater than 300 MeV in the CMS frame, then a calculation can be made of the CMS angle given any LAB angle and the results are shown in Figure 48. The dashed line in Figure 48 is set to 90° emission in the CMS frame. The runs taken at 50 GeV/c and 150 GeV/c

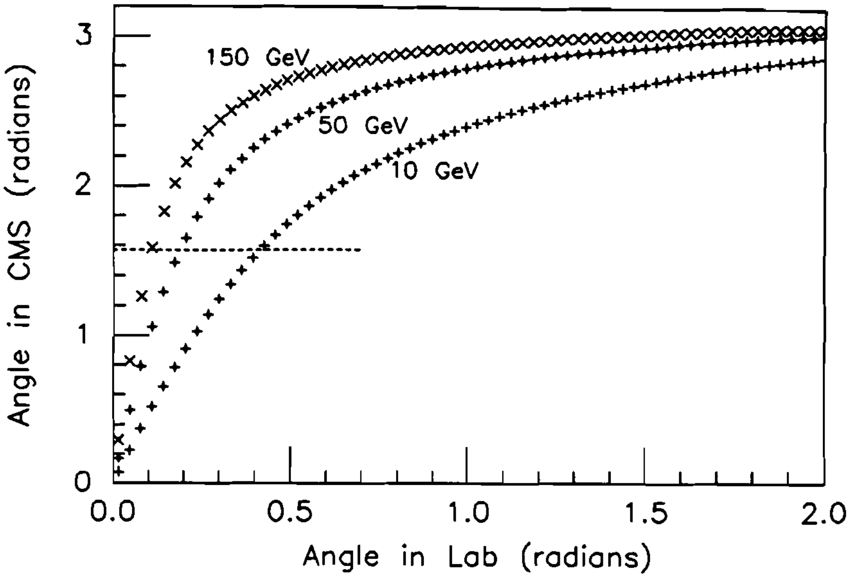

Figure 48: CMS Angle vs LAB Angle for π^-

have at least some coverage up to 90° in the CMS by the FDC in the testbeam setup. A plot of track distribution in θ^{lab} and ϕ^{lab} is shown in Figure 49 for the $150\,GeV/c$ Carbon target run. Comparing with the θ^{lab} in Table 4, there are tracks for some ϕ^{lab} angle ranges out to θ^{lab} angle of 0.36 radians. A reasonable way to fill in the missing coverage would be to weight the number of tracks in a band of θ^{lab} by the inverse of the amount of coverage in ϕ^{lab} of the band. A weight was calculated for each 0.01 band in θ^{lab}. A distribution of the tracks in θ^{cms} is shown for the unweighted data and for the weighted data in Figures 50a and 50b. For comparison, Figure 50c shows the unweighted data for tracks with a ϕ angle greater than π which has complete coverage out to a θ^{lab} angle of 0.25 radians. This subset of the unweighted data is equal to 40% of the weighted data for all bands including the bands with a weight of 1.0. The results for all three beam momentum runs are shown in Figure 51. Since the $10\,GeV/c$ data does not extend in the lab frame to the θ^{lab} angle equivalent to 90° in the CMS frame, one can extrapolate the data by adding in tracks at the missing θ^{cms} values in amounts equivalent to the numbers of tracks in the last few

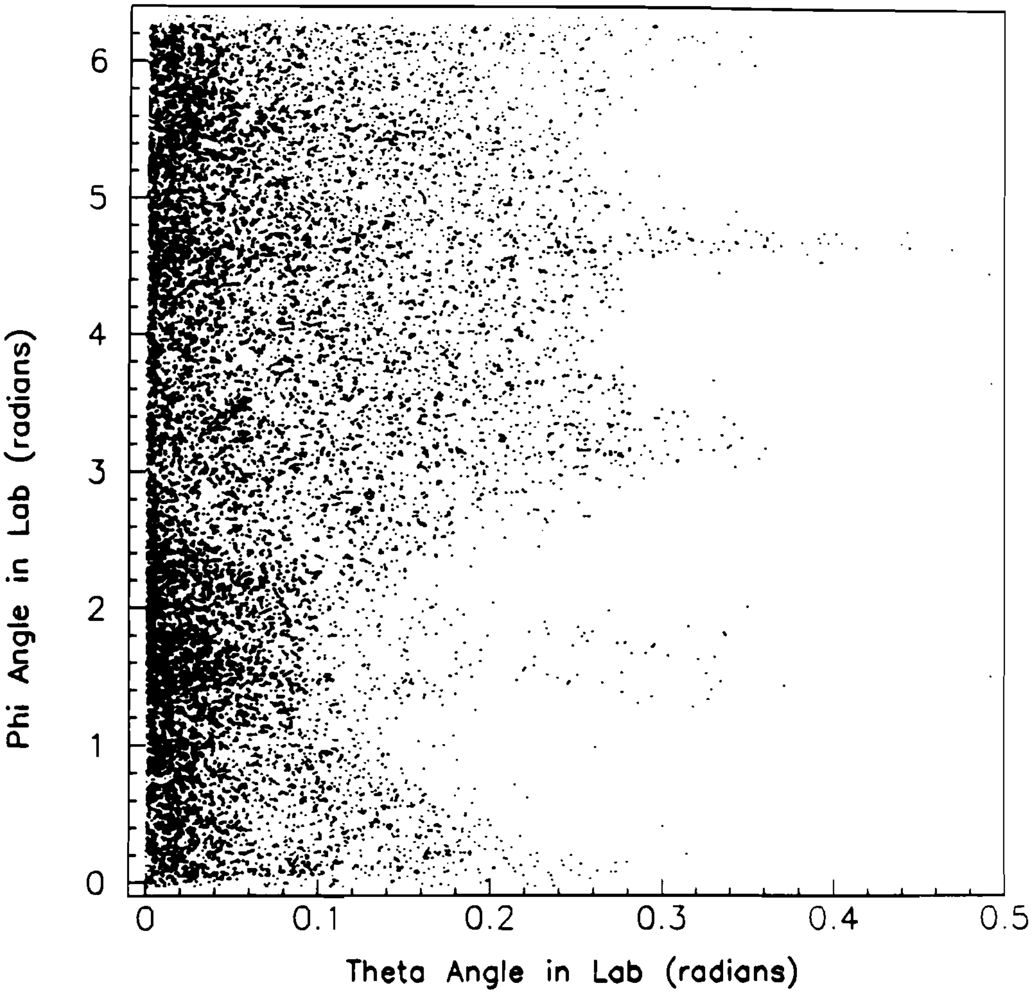

Figure 49: LAB Track Distribution in Angles ϕ^{lab} vs θ^{lab}

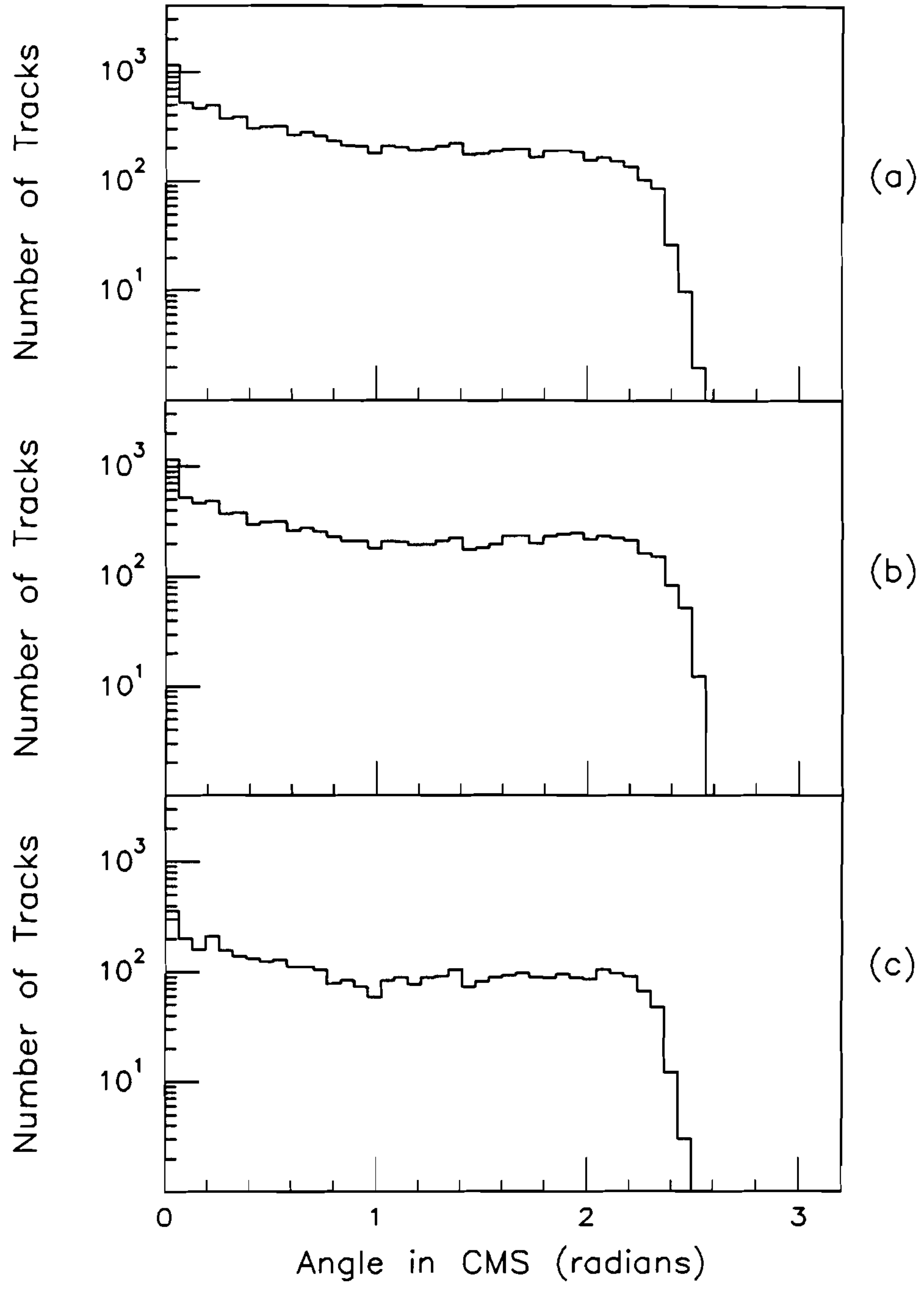

Figure 50: Track CMS θ Angle for $150\,GeV/c$ event data that has been accumulated in three different ways (a) unweighted, (b) weighted, and (c) unweighted with $\phi^{lab} > 3.14$ from Carbon target runs.

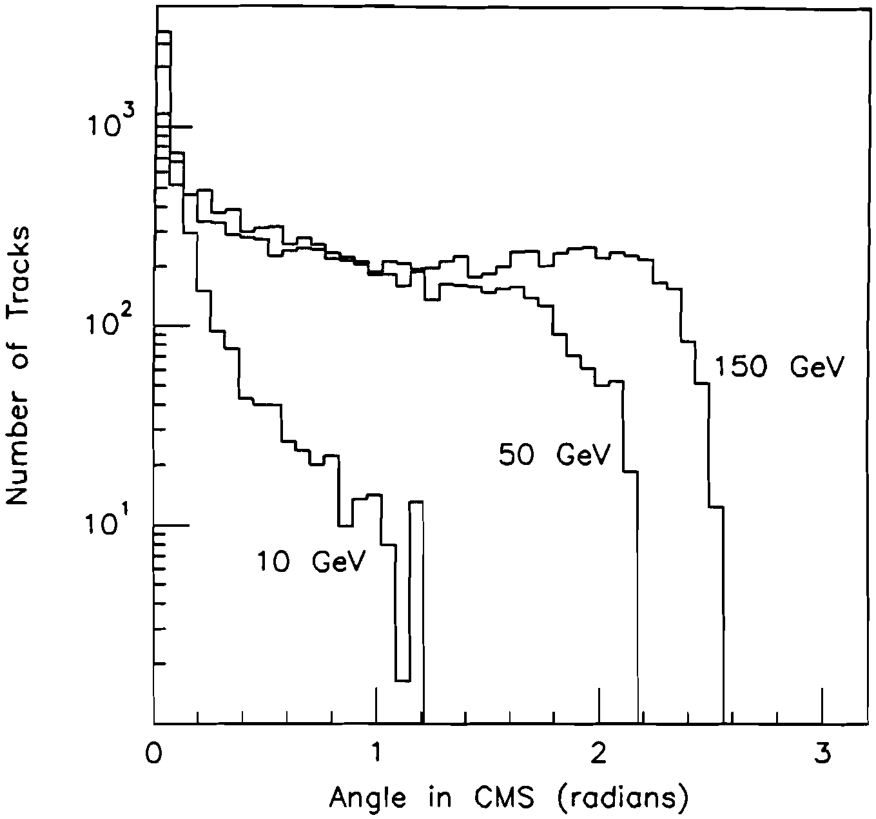

Figure 51: Track CMS θ Angle for Weighted Data from Carbon Target Runs

filled θ^{cms} bins. By extending the $10\,GeV/c$ coverage to 90°, one achieves an acceptance of 50% which can be made 100% by assuming symmetry in the forward-backward direction in the CMS frame. This method makes maximum use of the tracks collected at all three momenta. If one limited the acceptance to the maximum, unweighted coverage of the $10\,GeV/c$ runs, then the acceptance would be only $\approx$ 16% and would be dominated by the leading particles.

Measurement of the charged particle multiplicities in each event made use of the standard reconstruction package and the PWC beam reconstruction software mentioned earlier. In each event, every track is corrected for the initial beam position at the target by using the PWC information. If the PWC information is not available then the event is thrown out. Each track counts towards the event multiplicity if it projects back to within a $5.0\,cm$ radius of the target. The center of the target is determined by a gaussian fit made to all the track positions as projected back to $z = 0.0\,cm$. This value was unique for each beam momentum setting but consistent within 1.6% ($0.05\,cm$) of the average value for all runs of the same momentum. Without the PWC information correcting the tracks, the track position values at the target ($z = 0.0\,cm$) are spread evenly across the full $5\,cm$ width of the defining target trigger scintillators. The track was also required to be within the equivalent acceptance radius of the beam center on the FDC front face at $z = 105.345\,cm$ as listed in Table 4. The distribution of the tracks at the chamber is smeared by the beam width. Applying the PWC correction to tracks allowed a gaussian fit to be made to the distribution of the position of all of the tracks on the FDC front face ($z = 105.345\,cm$). The mean position for all runs of the same momentum was consistent within 0.3% ($0.1\,cm$) of the average value for all runs of the same momentum. Using these mean positions to set the beam path, the track angle with respect to the beam path was calculated for all tracks.

The event multiplicity was set equal to the number of the tracks passing the cuts on distance from target center and the acceptance distance on the face of the FDC divided by the total number of contributing events. All events with only one track were thrown out because single track events could arise from elastic scattering and the requirement is for inelastic events. The resultant distributions of mean multiplicity for the carbon target at each momentum is shown in Figures 52 and 53. Statistical errors were calculated treating each $0.01\,\theta^{lab}$ bin as independent and summing the weighted statistical error for each bin. Systematic errors are much larger, dominating the result. The major contributor is the tracking efficiency for complicated events. In a study performed using Monte Carlo-generated event data [39], the tracking efficiency for both FDCs combined was

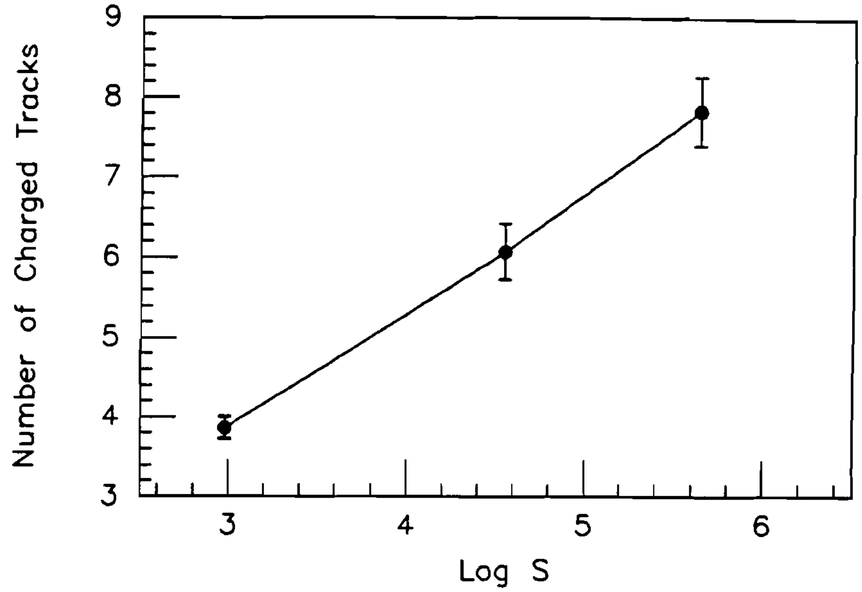

Figure 52: Track Multiplicity for Carbon Target - Log Law Trend

determined for up to 108 tracks per event. Since the testbeam setup only had just over one-fourth of one FDC instrumented, a comparable number of tracks per event would be roughly four times the number of tracks detected. This includes a factor of 0.5 for only forward coverage in the testbeam and a cancelling factor of 2.0 for two FDCs in the DØ Detector of the Monte Carlo program. Also, the delay line inefficiency for the target run data was only 54% in the inner Θ quadrants and 69% in the outer Θ quandrant. Comparing to the Monte Carlo simulation efficiency of 89% in both layers, a rough estimate of the real data tracking reconstruction inefficiency would be the Monte Carlo inefficiency scaled by a factor of 3.5. This can be treated as a correction since the reconstruction depends on successful delay line-sense wire matches to assemble segments into tracks and to allow two segment tracks. Recall all two segment tracks must have at least one matched delay line and sense wire. The Monte Carlo simulation reconstruction inefficiency can also be used as an error (without multiplier) because the reconstruction can both fail to find tracks and contain bad track

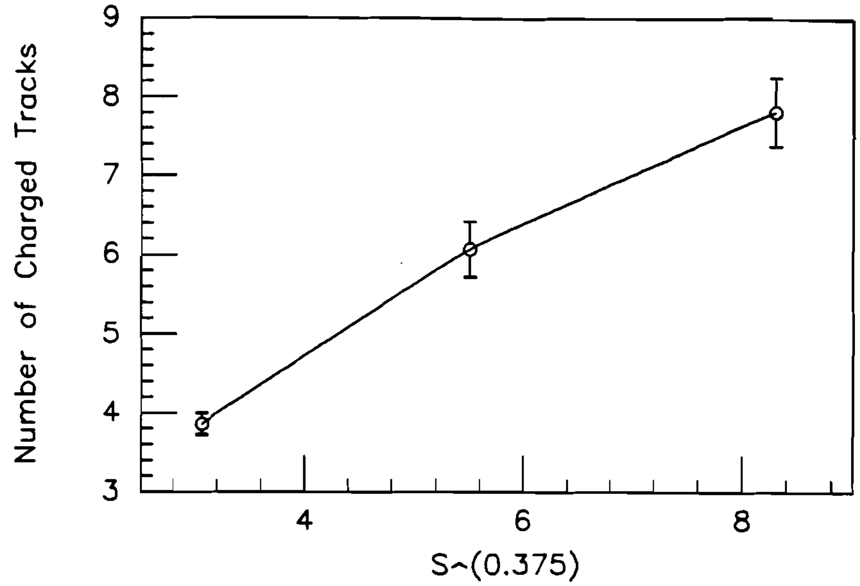

Figure 53: Track Multiplicity for Carbon Target - Power Law Trend

combinations.

Forward dominance is shown in the data. One would expect isotropy in the track distribution in the CMS frame for all angles except in the forward-backward direction where the effects of quark-gluon jets dominate. Counting only tracks in the forward region that is completely covered by the FDC (16% acceptance), the number of tracks per event only increased by 20% from 10 GeV/c to 150 GeV/c. A sample using an off-axis region (0.8 to 1.06 *rads*), showed 14 times more tracks per event in the 150 GeV/c beam runs than in the 10 GeV/c runs. This shows the dominance of the leading particle in the forward region bringing with it some of the other particles at all beam momenta. However, many particles in the higher momenta, higher multiplicity events are being emitted uniformly at all angles in the CMS frame.

A comparison of the results of this experiment with other experiments is shown in Figure 54. The dotted line in this figure shows the expected multiplicities from a bubble chamber experiment [27] which involved a π^- beam incident on protons in the hydrogen, a single nucleon target. The dashed lines show data results from other experiments [40] [41] [42]. Reference [40] involved propane-filled bubble chambers while the other two used Carbon targets in front of hodoscope arrays at Fermilab [41] and at the CERN SPS [42]. It can be seen that this experiment's results are lower than the other experimental results at the higher values of $\ln s$ by 1 to 2 standard deviations. The most likely explanation is the increased density of tracks at increased momenta. The forward region becomes a smaller and smaller radius cone as the beam momentum increases. An accurate track reconstruction efficiency versus track density has not been done with the Monte Carlo simulation at this time. A folding together of the delay line efficiency and the two track separation efficiency could possibly provide a better correction at higher momenta with further study.

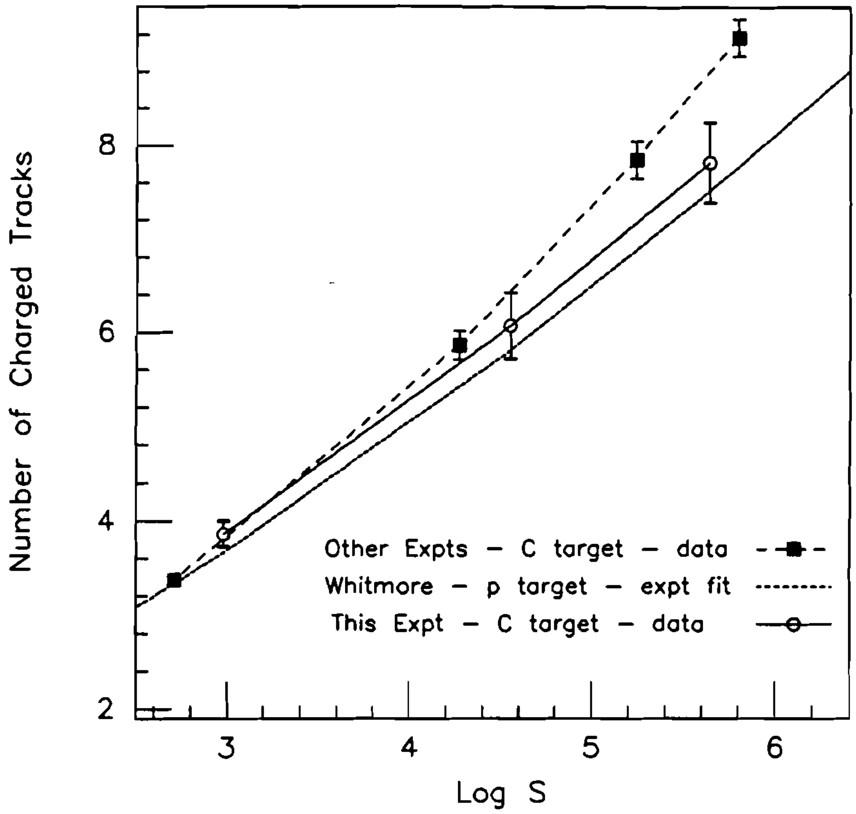

Figure 54: Track Multiplicity for Carbon Target comparing this experiment with other experimental results for the log law trend.

5.3 Elastic Diffractive Scattering

Elastic diffractive scattering occurs in most of the the single track events recorded during the target runs. The process contributing most to the single track events is Coulomb scattering. Single and multiple Coulomb scattering occurs when an incident charged particle is deflected slightly by the Coulomb interaction between it and the atoms in the target. The dominant component producing the largest deflections is caused by interaction with the atomic nuclei. Much smaller angle deflections arise at greater impact parameters where the electron cloud shields the charge of the nucleus. The energy lost in these collisions is negligible due to the high mass of the target. However the transverse scattering is appreciable in the Coulomb field of the nucleus. For a 'thick' target (a few % of a radiation length), multiple small angle scatters are likely with each one independent of the other. The thickness of each target in radiation lengths is given in Table 5 along with the rms angle of deflection of a $10\,GeV/c$ π^- due to multiple scattering in the target. This last quantity was determined using

$$\theta_o = \frac{13.6\,MeV}{\beta c p} z \sqrt{\frac{x}{X_0}} \left[1 + 0.038 \ln \frac{x}{X_0}\right] \tag{26}$$

The second and more interesting electromagnetic process with the single track events is diffractive scattering which is very similar to optical scattering of waves. Just like the diffraction caused by a completely or partially absorbing disk placed in the path of a light wave, the elastic cross section at non-zero angles is dominated by particles scattered by the disks of the target nuclei. The amplitude of the scattering is related to the cross-sectional area of the nuclei which is proportional to $A^{2/3}$. For large enough incident particle momenta, diffraction minima can be observed. Although this experiment reached high enough incident momenta to observe these minima, the cross section at the minima was at least four orders of magnitude below what was obtainable with the available quantity of data. A summary is given below of diffractive elastic scattering using the

	Parameters			
	Thickness	Radiation Length	Fraction	Multiple Scatter
Target	x (cm)	X_0 (cm)	x/X_0	Angle $10\,GeV/c\ \pi^-$(mrad)
Beryllium	10.236	35.30	0.290	0.388
Carbon	5.664	18.8	0.301	0.406
Aluminum	2.540	8.9	0.285	0.380
Iron	0.788	1.76	0.448	0.632
Copper	0.502	1.43	0.351	0.485
Zinc	0.548	≈ 1.38	0.397	0.556
Lead	0.155	0.56	0.277	0.366

Table 5: Target Multiple Scattering Parameters

first Born approximation in an optical model as reviewed in [43].

5.3.1 Basic Theory

Since the diffraction peak occurs at high momenta in all hadronic systems, it can not depend on the precise nature of the hadrons at least to first order. Therefore, the internal quantum numbers particularly spin can be ignored. Although the system under consideration is relativistic, a non-relativistic treatment will be given. A modification to obtain a relativistic solution will be mentioned.

Consider two spinless particles a and b of masses m_a and m_b. The Schrödinger equation in the CMS system for spinless particles is

$$[\nabla^2 + k^2]\psi(\mathbf{r}) = U(\mathbf{r})\psi(\mathbf{r}) \tag{27}$$

where $U(\mathbf{r}) = 2mV(\mathbf{r})$ and $k^2 = 2mE$. Here, m is the reduced mass $m_a m_b/(m_a + m_b)$, E is the total kinetic energy of the system, and the initial and final three-momentum of particle a are $\mathbf{k}$

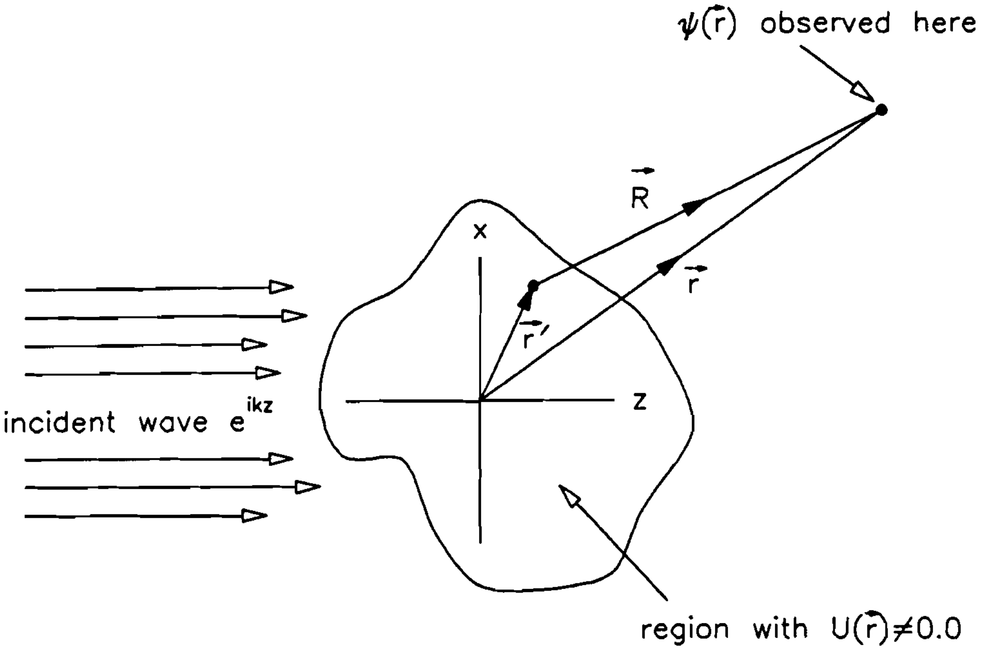

Figure 55: Scattering of a Plane Wave by a Potential

and $\mathbf{k}'$ respectively. If one assumes that the potential falls off more rapidly than $1/r$ as r increases and that it has cylindrical symmetry about the line of incident particle motion, the approximate wave function becomes

$$\psi(\mathbf{r}) = \psi_{inc}(\mathbf{r}) + \psi_{scat}(\mathbf{r}) \tag{28}$$

where

$$\psi_{inc}(\mathbf{r}) = e^{i\mathbf{k}\cdot\mathbf{r}} = e^{ikz} \tag{29}$$

and in the far field limit of r much larger than the extent of $V(r)$

$$\psi_{scat}(\mathbf{r}) = f(\theta)\frac{e^{ikr}}{r} \tag{30}$$

See Figure 55. The elastic scattering amplitude $f(\theta)$ is related to the differential cross section in the CMS frame by

$$\frac{d\sigma}{d\Omega^*} = |f(\theta)|^2 \tag{31}$$

The solution for $\psi_{scat}(\mathbf{r})$ becomes

$$\psi_{scat}(\mathbf{r}) = -\frac{1}{4\pi}\int\left[U(\mathbf{r}')\psi(\mathbf{r}')\frac{e^{ikR}}{R}\right] \tag{32}$$

where $\mathbf{R} = \mathbf{r} - \mathbf{r}'$. Using the first Born Approximation in which $\psi(\mathbf{r})$ is replaced by $\psi_{inc}(\mathbf{r}) = e^{ikz}$, equation 32 can be reduced to

$$\psi_{scat}(\mathbf{r}) = -\frac{1}{4\pi}\int\left[U(\mathbf{r}')e^{ikz'}\frac{e^{ikR}}{R}\right] \tag{33}$$

The first Born approximation assumes that $\psi_{inc}(\mathbf{r})$ scatters only once on the potential and then leaves the potential region. Higher Born approximations which correspond to more scatters on the potential will be mentioned later.

Consider the optical analogy of a scattering plane light wave passing through and around a disk. Let the disk have a radius b_0 and a cylindrically symmetric absorption $\beta(b)$ for a radius b. If $\beta(b)$ is the absorption coefficient for the ampitude of the wave than the amplitude transmission coefficient is $1 - \beta(b)$. Therefore β is between 0 and 1 and for a completely absorbing disk, $\beta = 1$. For a plane wave moving in the $+z$ direction and a disk located at $z = 0$, the incident wave can be written as

$$\psi_{inc}(\mathbf{r}) = e^{ikz} = -\frac{ik}{4\pi}\int_0^{2\pi}\int_{b=0}^{b=\infty} d\phi' b' db'(1+\cos\theta')(1)\frac{e^{ikR}}{R} \tag{34}$$

The Huygens principle states that the amplitude at a point $\mathbf{r}$ can be found by regarding each point on the plane $z = 0$ as a source for a spherical wave. Including points on the disk as well as points beyond the disk, a summation of the points is

$$\begin{aligned}\psi(\mathbf{r}) &= -\frac{ik}{4\pi}\left[\int_0^{2\pi}\int_{b=0}^{b=b_0} d\phi' b' db'(1+\cos\theta')(1-\beta(b'))\frac{e^{ikR}}{R}\right.\\ &\quad\left.+\int_0^{2\pi}\int_{b=b_0}^{b=\infty} d\phi' b' db'(1+\cos\theta')(1)\frac{e^{ikR}}{R}\right]\end{aligned} \tag{35}$$

The scattering wave $\psi_{scat}(\mathbf{r})$ is the incident wave subtracted from the above equation and one obtains

$$\psi_{scat}(\mathbf{r}) = -\frac{ik}{4\pi}\int_0^{2\pi}\int_{b=0}^{b=b_0} d\phi' b' db'(1+\cos\theta')(-\beta(b'))\frac{e^{ikR}}{R} \tag{36}$$

For small angle scattering $\cos\theta = 1$ so

$$\psi_{scat}(\mathbf{r}) = -\frac{1}{4\pi}\int_0^{2\pi}\int_{b=0}^{b=b_0} d\phi' b' db' \left[(-2ik\beta(b'))\frac{e^{ikR}}{R}\right] \tag{37}$$

If the disk had a non-zero thickness and if $\beta_L(\mathbf{r}')$ was the absorption per unit length along the z axis. Then

$$\psi_{scat}(\mathbf{r}) = -\frac{1}{4\pi}\int d^3r' \left[-2ik\beta_L(\mathbf{r}')e^{ikz'}\frac{e^{ikR}}{R}\right] \tag{38}$$

For a quantum mechanical potential similar to the action of the absorbing disk

$$U_{abs}(\mathbf{r}) = -2ik\beta_L(\mathbf{r}') \tag{39}$$

where $\beta_L(\mathbf{r}')$ is real and greater than zero. Using $\mathbf{R} = \mathbf{r} - \mathbf{r}'$ and for r much greater than r', $R \approx r - \mathbf{r}\cdot\mathbf{r}'/r$. Equation 33 becomes

$$\psi_{scat}(\mathbf{r}) = \frac{e^{ikr}}{4\pi r}\int d^3r' \left[U(\mathbf{r}')e^{i(\mathbf{k}-\mathbf{k}')\cdot\mathbf{r}'}\right] \tag{40}$$

Comparing with equation 30, one obtains

$$f(\theta) = -\frac{1}{4\pi}\int d^3r' \left[U(\mathbf{r}')e^{i(\mathbf{k}-\mathbf{k}')\cdot\mathbf{r}'}\right] \tag{41}$$

This is the basic equation for $f(\theta)$ in the first Born approximation to the optical model which will be needed later.

One model for elastic scattering consists of replacing the target particle by a disk of radius R with a constant absorption coefficient β in the $x-y$ plane at $z=0$ and setting the incident particle radius to zero. Setting the distance between particle centers to b then the potential becomes

$$U(b,z) = -ik2\beta\delta(z) \qquad b \le R \tag{42}$$

$$U(b,z) = 0 \qquad\qquad b > R \tag{43}$$

Using this potential, noting that $\mathbf{k}\cdot\mathbf{r}' = kz'$ and defining the two-dimensional vector $\mathbf{b}$ in the xy plane, the z' integration can be carried out

$$f(\theta) = \frac{ik\beta}{2\pi}\int_0^{2\pi} d\phi' \int_0^R b'db' e^{-i\mathbf{k}'\cdot\mathbf{b}'} \tag{44}$$

If $\mathbf{k}'$ is put in the xz plane then $\mathbf{k}'\cdot\mathbf{b}' = kb'\sin\theta\cos\phi'$ where ϕ' is the angle between the x axis and the vector $\mathbf{b}'$. The scattering angle, θ, is the angle between $\mathbf{k}'$ and the z axis. The form of the Bessel functions of the first kind is

$$J_n(z) = \frac{i^{-n}}{\pi}\int_0^{\pi} e^{iz\cos\theta}\cos(n\theta)d\theta \tag{45}$$

Selecting $n = 0$ and setting $z = b'k\sin\theta$, then

$$f(\theta) = ik\beta\int_0^R b'db' J_0[b'k\sin\theta] \tag{46}$$

Integrating, one obtains

$$f(\theta) = ik\beta R^2\left[\frac{J_1[Rk\sin\theta]}{Rk\sin\theta}\right] \tag{47}$$

Since this is in the CMS frame and $(\mathbf{k}-\mathbf{k}')$ is the three-momentum transferred in the collision, $t = -(\mathbf{k}-\mathbf{k}')^2$. For small angles,

$$\sqrt{-t} \approx k\sin\theta \tag{48}$$

Since $J_1(z) = (z/2) - (z/2)^3/2! + \cdots$ and for small angles ($\sin\theta \approx \theta$) then

$$f(\theta) = \frac{ik\beta R^2}{2}\left[1 - \frac{(Rk\theta)^2}{8}\right] \tag{49}$$

For small angles, the differential cross section is represented by $d\sigma/dt = Ae^{-b|t|}$ so that

$$A = \frac{\pi}{k^2}|f(0)|^2 \tag{50}$$

$$f(\theta) = f(0)\exp[-bk^2(1-\cos\theta] \approx f(0)\left[1 - \frac{bk^2\theta^2}{2}\right] \tag{51}$$

Four major points are observed in comparing equations 49 and 51.

$$f(\theta) \text{ will be purely imaginary} \tag{52}$$

$$f(0) = ik\beta R^2/2 \tag{53}$$

$$A = \pi\beta^2 R^4/4 \tag{54}$$

$$R^2 = 4b \tag{55}$$

To improve the model, the sharp-edged disk of zero-thickness for each particle can be replaced by matter distributions. For particle a, a Gaussian matter distribution would be

$$\rho_a(\mathbf{r}_a) = g_a e^{-r_a^2/R_a^2} \tag{56}$$

and a similar expression could be written for particle b. If these two distributions pass through each other with a mutual absorption, we can fold these Gaussian expressions together to obtain a Gaussian potential $U(\mathbf{r})$

$$U(\mathbf{r}) = -2ik\eta e^{-r^2/R^2} \tag{57}$$

Again, the Lorentz contractions of the distributions have been ignored. This can be expressed as

$$U(\mathbf{r}) = -2ik\beta_L(\mathbf{r}) \tag{58}$$

where $\beta_L(\mathbf{r})$ is the general amplitude absorption coefficient. For a particle passing along the z axis, one can define β_0, a special absorption coefficient where

$$\beta_L(\mathbf{r}) = \left[\eta \int_{-\infty}^{+\infty} e^{-r^2/R^2} dz\right]_{x=0,y=0} = \eta\sqrt{\pi R^2} \tag{59}$$

It should be noted that

$$0 \leq \beta_0 \leq 1 \tag{60}$$

Rewrite equation 57 in the form

$$U(\mathbf{r}) = -2ik\frac{\beta_0}{\sqrt{\pi R^2}} e^{-r^2/R^2} \tag{61}$$

and inserting this into equation 41, the result is

$$f(\theta) = \frac{ik\beta_0 R^2}{2} e^{-(R^2/4)(\mathbf{k}-\mathbf{k}')^2} \tag{62}$$

and from there

$$\frac{d\sigma}{dt} = \frac{\pi\beta_0^2 R^4}{4} e^{-(R^2/2)|t|} \tag{63}$$

The first Born approximation using a Gaussian absorption density yields an exponential form for the diffraction peak. This differential cross section is free of the dips and bumps of the Bessel functions that appeared in the sharp-edged disk result. Also, by changing $\beta_L(\mathbf{r})$ as a function of $\mathbf{r}$, the large angle part of the diffraction peak can be changed without significantly altering the small angle part of the peak. The two different results indicate the shape of the diffraction peak can provide information about the assumed matter distribution inside the particles. A smoothly decreasing diffraction peak comes from a smoothly decreasing matter distribution and a diffraction peak dropping through a series of bumps and dips comes from a matter distribution which decreases suddenly. Experimental results show a series of sharp dips and bumps indicating that the nucleus has a reasonably well-defined radius.

Additions to this model are the Lorentz contraction of the sources and the possibility of many collisions taking place while the incident particle is in the potential. To include the Lorentz contraction, substitute

$$r^2 = x^2 + y^2 + \gamma^2 z^2 \qquad \text{where } \gamma = [1 - (v/c)^2]^{-1/2} \tag{64}$$

in equation 57 and recalculate the differential cross section. This is not a complete relativistic treatment as a full treatment using relativistic quantum mechanics also includes the production and annihilation of particles. The optical model can not include additional particles.

Multiple collisions are more complex. A derivation using an eikonal approximation was carried out by Glauber [44]. The result is a series solution

$$f(\theta) = \sum_{n=1}^{\infty} f_n(\theta) \tag{65}$$

$$f_n(\theta) = \frac{kR^2(-\lambda)^n}{2in(n)} e^{b_n t/2}, \qquad b_n = \frac{R^2}{2n} \tag{66}$$

where $f_1(\theta)$ is similar to the result of equation 62. Each term adds a smaller contribution and a decreasing exponential slope so that at $t = 0$ the lowest n terms are the most important.

In all of these results, the differential cross section is proportional to $e^{-\alpha R^2|t|}$ where α is a constant and $|t|$ is the square of the momentum transfer. R^2 is the square of the radius of the potential of the target nucleus. An approximate value for the radius of a given nucleus, R_A, is given by

$$R_A = r_N \cdot A^{1/3} \tag{67}$$

where r_N is the radius of an individual nucleon. Thus, one obtains

$$\frac{d\sigma}{dt} = \frac{\pi \beta_0^2 R^4}{4} e^{-(r_N^2 A^{2/3}/2)|t|} \tag{68}$$

5.3.2 Nuclear Slope Measurements

The NWA target data runs contained a subset of events that contained only a single track. These events formed the pool from which the elastic scattering events were selected. There were runs available from all seven targets at beam momenta of $10\,GeV/c$, $50\,GeV/c$, and $150\,GeV/c$. Unfortunately, due to the insufficient quantity of data and narrowness of the expected nuclear slope, the $50\,GeV/c$ and $150\,GeV/c$ target data runs did not yield a usable result.

Events had to pass a series of cuts and requirements to be considered as elastic events. The basic requirements are a track in the last two PWCs, those after the last magnet and before the target (NW9PWCB,NWAPWCA), and a single track found in the FDC. In addition, a limit of up to one segment is allowed in each layer to eliminate any possible second tracks from being missed because they were not reconstructed as a full track. These limits pass events with one particle track into the target and one particle track out of the target towards the FDC. The PWC track leading up to the target was required to be fairly parallel to the average beam path to eliminate beam particles that may have scraped the magnet or may have momenta beyond the typical beam momentum spread. The PWC slope in the x direction along the beam path was limited to be between -0.73 and 1.57 $mrad$. The PWC slope in the y direction along the beam path was limited to be between -0.66 and 0.50 $mrad$. These cuts are derived from $\pm 2.5\sigma$ of the gaussian fit to the uncut slope distribution. See Figure 56. A maximum transverse distance from the target of the track in the event of 2.0 cm from the target center in the x direction and 1.0 cm in the y direction was allowed to insure that the single track measured came from the target. See Figures 57 and 58. This eliminates particles highly scattered by the material of the FDC itself and eliminates any secondaries that may have been created by the scattered beam particle after the target. All of these restrictions are meant to compensate for the lack of full acceptance of the detector, any beam particle identification, and a momentum measurement of the scattered beam particle.

The single track distribution in $|t|$ was obtained using the distance of the track from the projected beam center on the face of the FDC. The beam path and beam center were obtained by fitting the distribution of all the single track positions in x and y at the target and on the front face of the FDC. Before the fit, the PWC x and y track positions at the target were used to correct the reconstructed track to eliminate the original beam size. The original beam particle distribution is distributed approximately equally over the surface of the small target trigger scintillators. The PWC track position for the event is used to translate each particle track in (x, y) to a single point on the target face. This effect also occurs on the face of the FDC. Figures 59-62 show the effects of the PWC correction on the x and y direction positions of the scattered particle on the front face

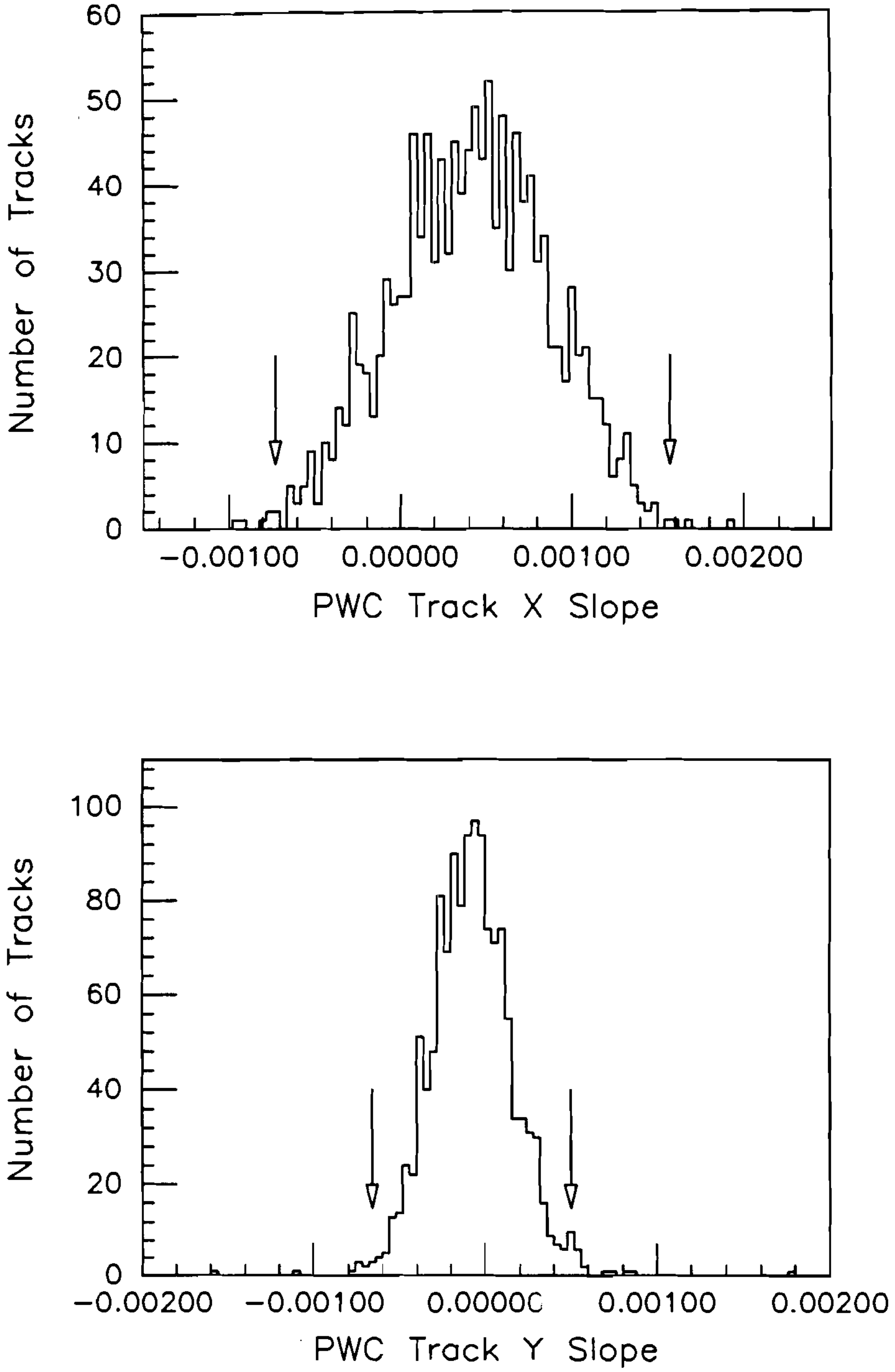

Figure 56: PWC Track Slopes in the x and y Directions. The arrows indicate the slope cut-off values.

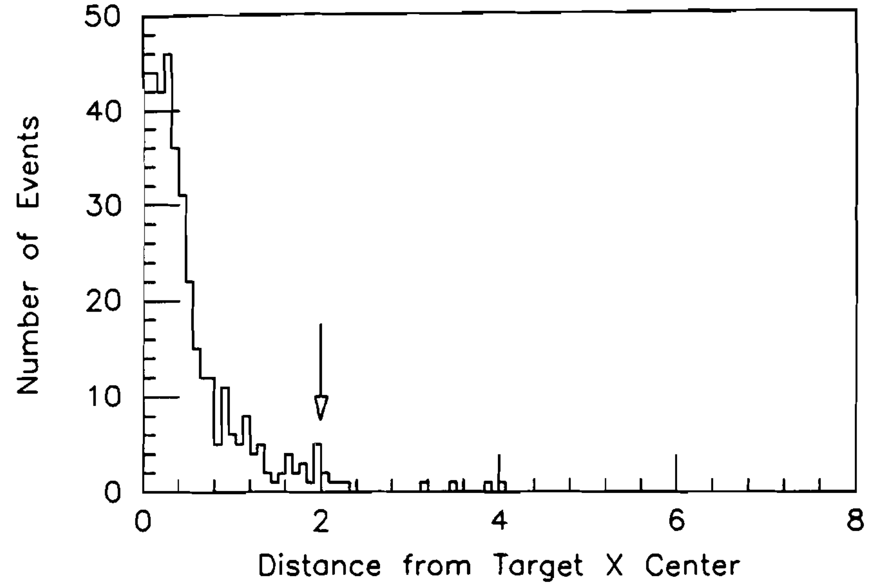

Figure 57: Radius from Target Center in the x Direction. The arrow indicates the slope cut-off value.

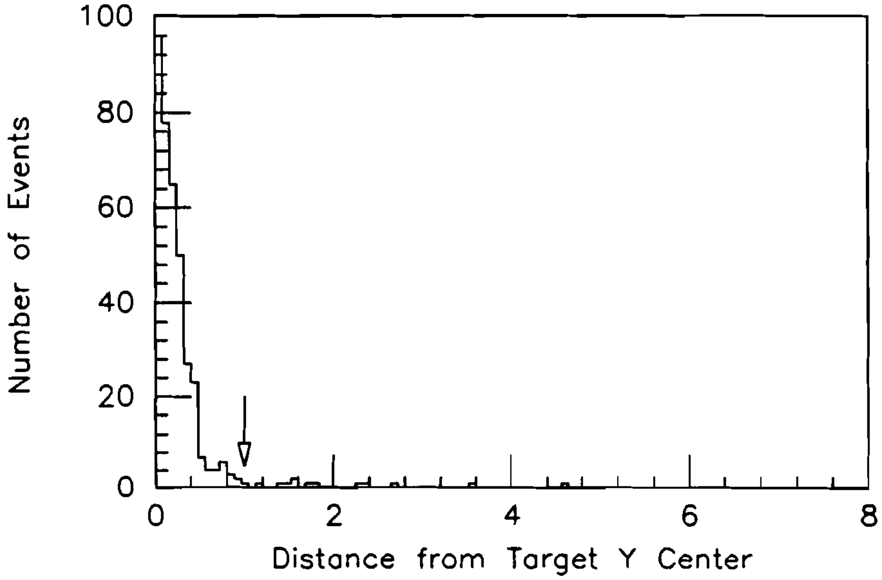

Figure 58: Radius from Target Center in the y Direction. The arrow indicates the slope cut-off value.

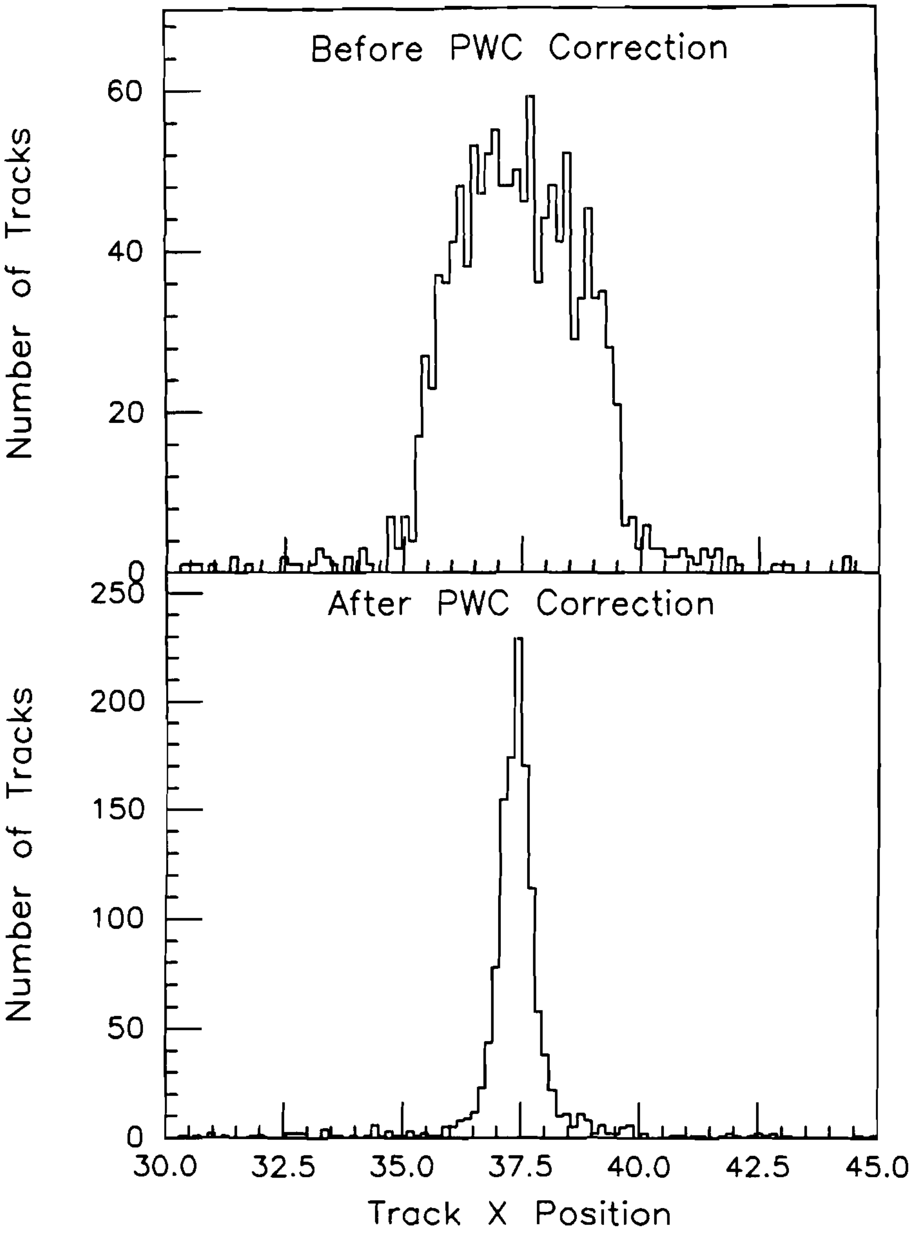

Figure 59: Single Track Distribution in x at the FDC

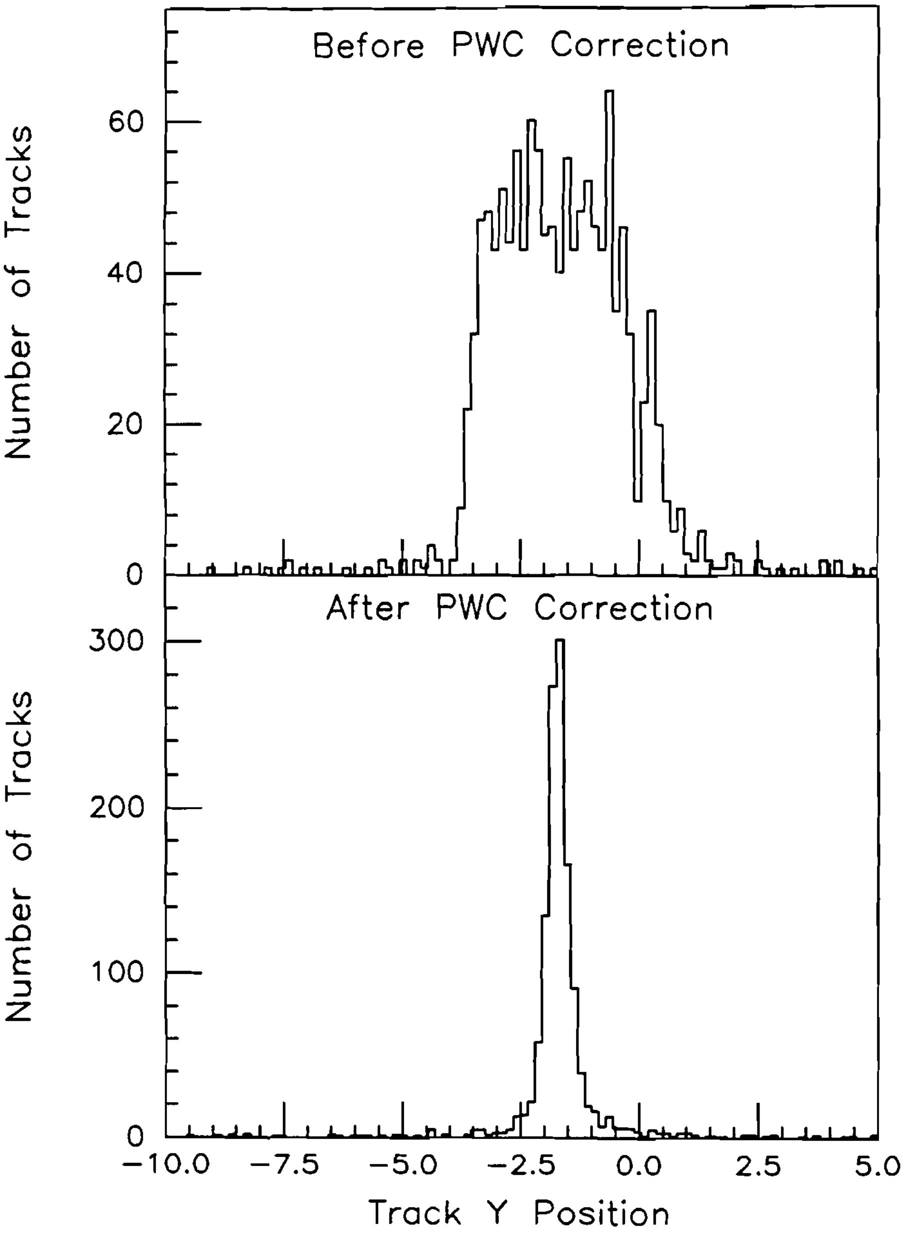

Figure 60: Single Track Distribution in y at the FDC

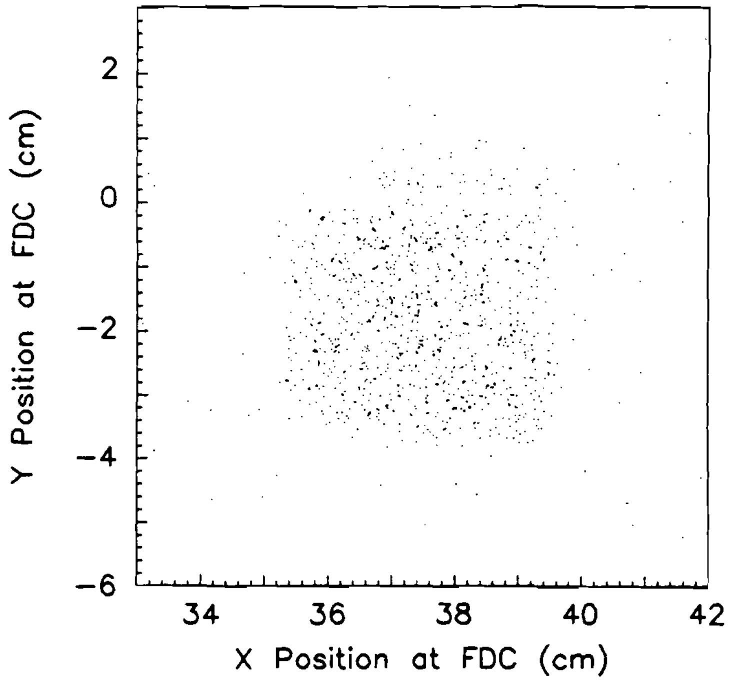

Figure 61: Scattered Particle Position at the FDC Before Correction

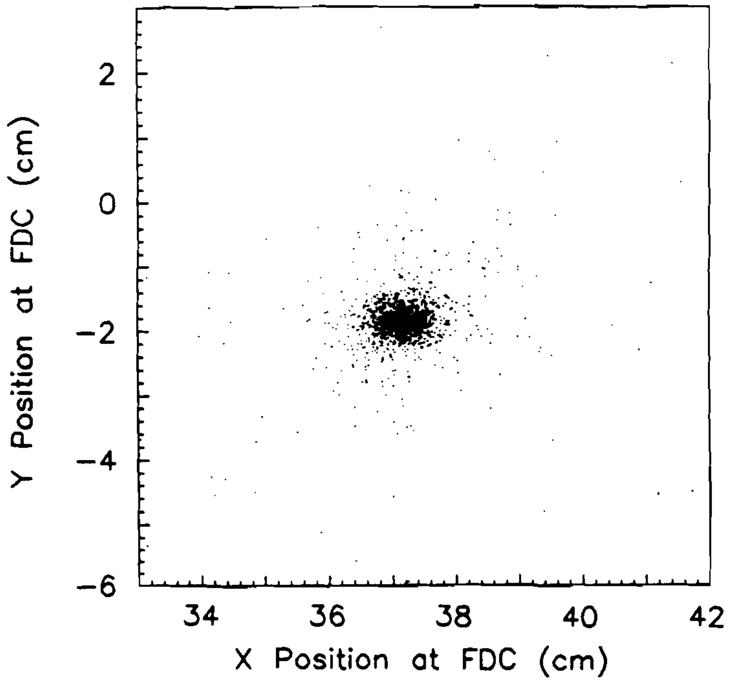

Figure 62: Scattered Particle Position at the FDC After Correction

of the FDC. The center of the distribution is considered the beam center at that point in z. The beam path is defined as the line from the center of the distribution at the target to the center of the distribution on the front face of the FDC. This occurs at z positions of $0.0\,cm$ and $105.3\,cm$ where the expected error is $\pm 0.5\,cm$. It should also be noted that the "front face" of the FDC is defined as the z position of the first sense wire encountered by a particle coming from the target. This is sense wire 7 in the inner Θ quadrants. In order to use the PWC track slopes as a correction, a track found in the FDC is projected back to the target at $z = 0.0$ then re-projected to the front face of the FDC. The re-projection corrects the slope of the FDC track with the slope of the PWC track. This correction makes all the beam particles parallel.

The value of $|t|$ for each track is calculated using the beam momentum and the angle of scatter. If t is the momentum transfer in the elastic scatter then

$$t = -(\mathbf{p} - \mathbf{p}')^2 \tag{69}$$

where p is the momentum vector of the incident particle and p' is the momentum vector of the scattered particle. For elastic scattering, $|\mathbf{p}| = |\mathbf{p}'|$. Thus, for a small scattering angle θ,

$$t \approx -(p \cdot \sin\theta)^2 \tag{70}$$

Using the small angle approximation $\sin\theta = \theta$, one obtains

$$t \approx -(p \cdot \theta)^2 \tag{71}$$

For this experiment, the momentum is $10\,GeV/c$ and the scattering angle θ is the radius of the scattered particle, r_{scat}, at the FDC divided by the distance from the target to the FDC ($\Delta z = 105.3\,cm$).

$$-t \approx (10\,GeV/c \cdot \frac{r_{scat}\,cm}{105.3\,cm})^2 \tag{72}$$

At the higher two beam momenta, the lack of sufficient single track events outside of the multiple scattering window in the expected $|-t|$ window made it impossible to obtain any results. Recall that the differential cross section falls off as $e^{-|t|}$. As p climbs, the value of θ must drop proportionally to yield the original value of $|t|$. The multiple scattering rms angle of deflection falls only as $1/p$. The $-t$ distribution of tracks for the carbon target $10\,GeV/c$ data run is shown in Figure 63. The dotted outline shows the $-t$ distribution without the PWC corrections while the solid outline shows the $-t$ distribution with the PWC corrections. Tracks with a value of $-t$ below $0.005\,GeV^2$ are considered to be part of the Coulomb scattering peak or part of the interference region between the Coulomb scattering and the nuclear diffractive scattering. The cutoff value was determined using the standard deviations of the FDC track fit, the PWC track fit, and the multiple scattering mean angle.

All tracks that pass the numerous cuts and corrections to the data as mentioned above are plotted versus $-t$ in Figure 64. An exponential fit is made to the data and a slope value is obtained. The fit used an error for each histogram bin equal to the square root of the bin contents. Empty bins out to $0.12\,GeV^2$ were given an error equal to that of a bin containing a single track. The result for the carbon target data is shown as the dashed line in Figure 64. The data from each target run is analyzed according to the prescribed method. The slopes of the track distributions in $-t$ are shown in Table 6. Figure 65 shows the diffraction slopes versus the target nuclei $A^{2/3}$. The dashed line is a line fit where each slope value is weighted by its error. Because of the difficulty in obtaining a result from the lead data, it is excluded from the line fit. The errors for each slope are large because of the low number of data points. The slope of the line fit to six targets is $\approx$ 4.1 whereas the results from other experiments [45] [46] [47] [48] [49] is $\approx$ 8.0. The possible reasons for the difference between the two values are many. The foremost is the lack of sufficient statistics especially for the higher A value targets. The final fit for a slope to each target's data uses only about 30 to 50 tracks which is about two orders of magnitude too low. Beam particle identification using the Čerenkov counters would have eliminated contamination of e^- in the beam.

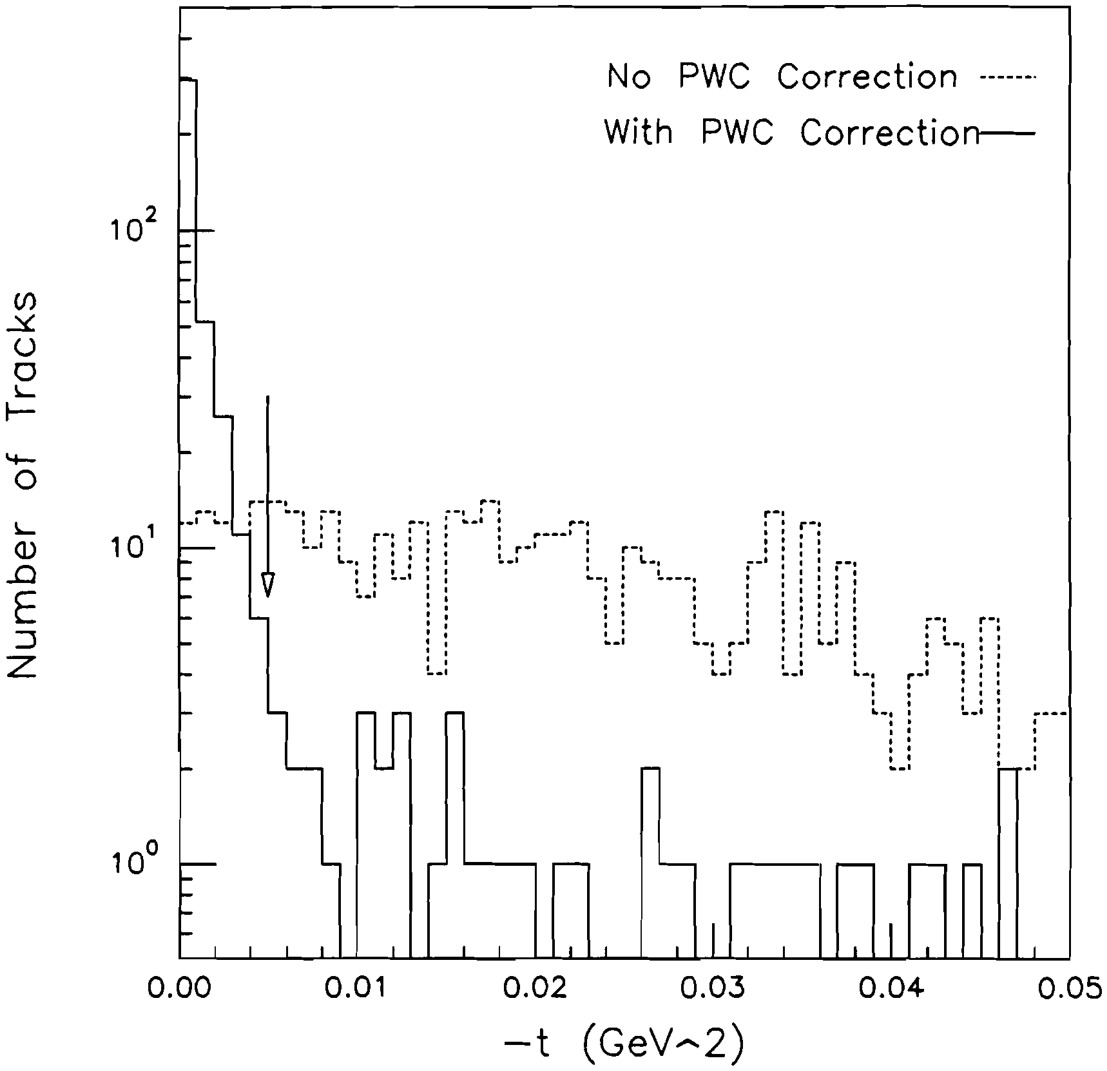

Figure 63: Carbon Target, $10\,GeV/c$ Track Distribution in $-t$

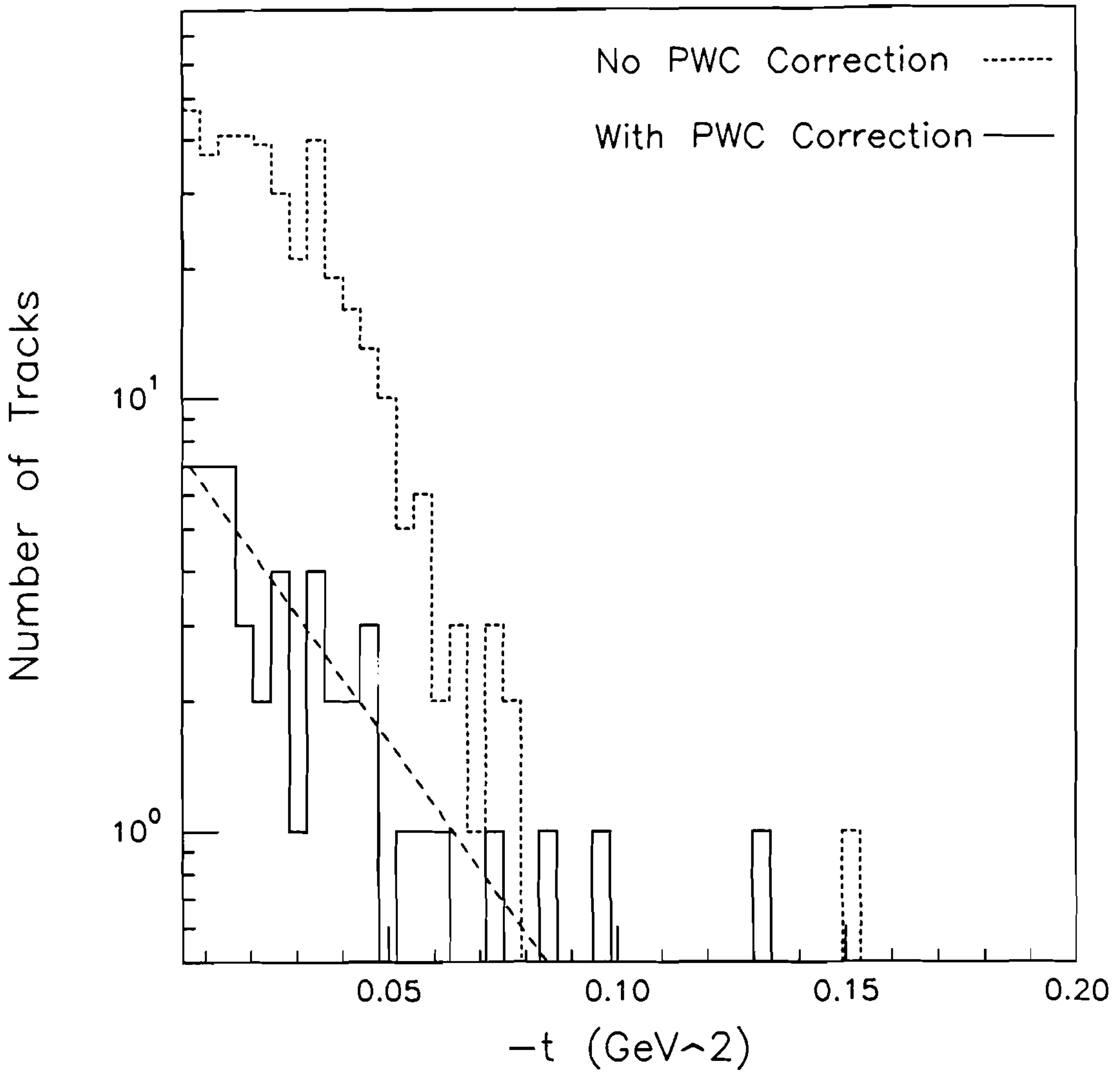

Figure 64: Carbon Target, 10 GeV/c Diffractive Track Distribution in $-t$

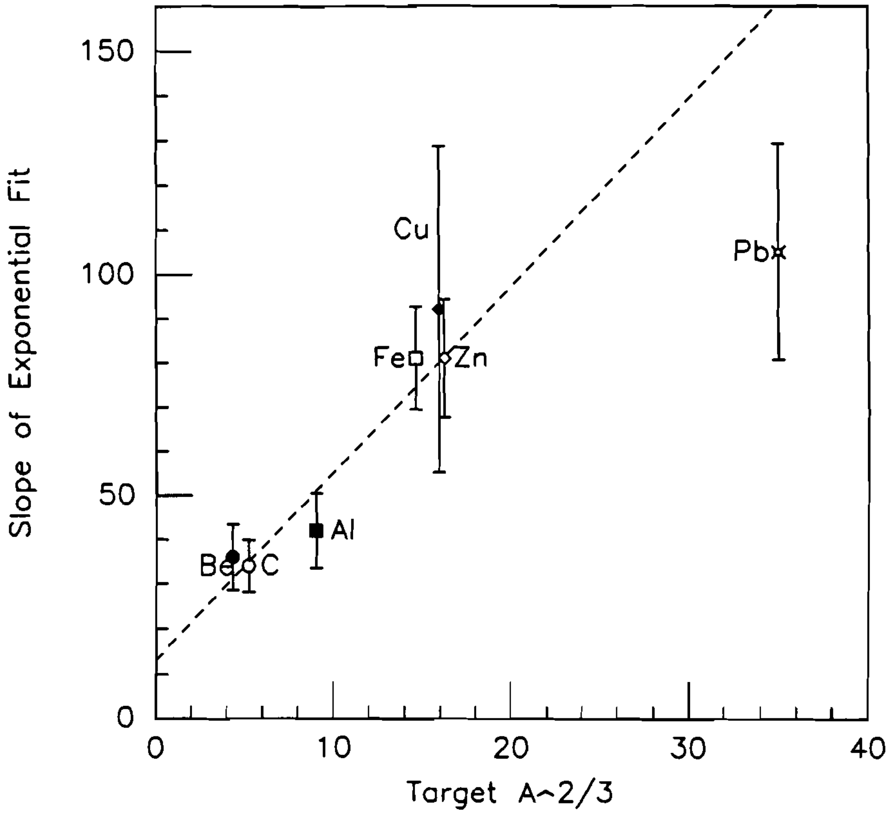

Figure 65: Elastic Diffraction Nuclear Slope versus Target $A^{2/3}$

	Parameters and Results				
Target	Z	A	$A^{2/3}$	Nuclear Slope	Slope Error
Beryllium	4	9.01	4.3	35.9	7.45
Carbon	6	12.01	5.2	33.9	5.84
Aluminum	13	26.98	9.0	42.5	8.46
Iron	26	55.85	14.6	81.2	11.6
Copper	29	63.54	15.9	91.6	36.8
Zinc	30	65.37	16.2	80.7	13.4
Lead	82	207.19	35.0	105.4	24.3

Table 6: Elastic Diffraction Parameters and Results

Beam μ^- were expected to be eliminated by the small angle Coulomb cut. In addition, scattered particle identification and momentum measurement would have eliminated any inelastic events from faking an elastic event. Tracking accuracy could have been improved by placing the second FDC downstream of the first to measure the scattered particle a second time. The reconstruction is good but it would have been an advantage to narrow down the spread of the Coulombic peak. Despite these shortcomings, the overall trend of the nuclear diffraction slopes does go as $A^{2/3}$ as the results indicate. Even the lead target data slope value is within three times the slope error of the expected value.

6 Summary

The first DØ Detector collider run has just begun at FNAL and the DØ Forward Drift Chambers are in place and ready to collect data. The results of the 1990 FNAL testbeam run effort have insured that the chambers are ready and capable of performing their task for the experiment. The testbeam setup contained a subset of the readout electronics and many other features that are currently represented full scale in the DØ collision hall. The experience obtained from the long hours of shift taking and subsequent data analysis provided a knowledge of the robustness of the chambers and the improvements necessary for running in the DØ Detector.

The results of the calibration showed the chambers behaving as expected not always under ideal external conditions. The linear relation between drift distance and drift time yielded typical drift velocities of $34\,\mu m/nsec$. The low hit resolution was $\approx 200\,\mu m$ with an efficiency of 96%. Thus, each charged particle track has position measurements in θ and ϕ which are independent and orthogonal. The sense wires are already accurately located in the third direction, z. The two hit resolution was $2.5\,mm$ at 90% efficiency and two track resolution was $4.8\,mm$ at 90% efficiency. The ionization resolution was 13.3%. These results indicate that the chambers will be very effective in meeting the needs of the DØ Detector. They were also adequate for the two experiments performed in the NWA setup.

The nuclear target runs taken in the middle of the testbeam effort provided data for two experiments that yielded reasonable results given the detectors and time frame available. The multi-track data events were taken at $10\,GeV/c$, $50\,GeV/c$, and $150\,GeV/c$ to look at the trend in charge track multiplicity with s, the energy in the CMS frame. Results for the carbon target show a trend going as $\ln s$ over the three beam momenta.

The target data from the $10\,GeV/c$ beam momenta runs for the range of targets from beryllium to lead were analyzed and showed the elastic diffractive nuclear slope followed a trend proportional to $A^{2/3}$ where A is the atomic mass. The result was consistent for six of the seven targets where the result for the seventh, lead, was within statistical probability but more likely was at the limit of the Forward Drift Chambers. Given the amount of data available and the expected narrow peak of the lead distribution, the lead result was expected to be compromised.

Future capabilities of the FDCs will include a possible fast trigger for the DØ Detector. The total collected charge from charged particle tracks passing through the FDCs can be obtained before extensive event processing. A study has shown that there is a correlation between the amount of charge collected and the total number of tracks reconstructed in the FDCs [50]. Event selection based on particle multiplicity would be possible using a trigger based on requiring a predetermined level of collected charge from the FDCs.

The two studies presented here were important to the overall understanding of the Forward Drift Chambers because they required the most precision possible and the highest efficiency obtainable in the most difficult of circumstances. The experience gained from all of the studies has allowed great understanding of the capabilities of the FDCs. Additional developments such as a fast trigger based on the FDCs show that even more can be achieved in the future.

References

[1] D0 Proposal and D0 Design Report, The D0 Experiment at the Fermilab Antiproton-Proton Collider (1984).

[2] S.H. Aronson *et al.*, *Proceedings of Conference on Multiparticle Dynamics*, Kiryat Anavim, pp. 827 (1985).

[3] P. Franzini, "Perspectives in Electroweak Interactions", *Proceedings of the XXth Rencontre de Moriond, Les Arcs, France*, pp. 185 (1985); R. Yamada, *Proceedings, Physics of Proton Antiproton Collisions, Tsukuba, Japan*, pp. 371 (1985). See also Internal D0 Note 226 (1985) (unpublished).

[4] M.A. Abolins, *Proceedings of the First Aspen Winter Physics Conference*, Annals of the New York Academy of Sciences, **461**, 63 (1986).

[5] P.D. Grannis, "Results and Perspectives in Particle Physics", *Proceedings of Les Rencontres de Physique de la Vallée d'Aoste, La Thuile, Italy*, pp. 253 (1987). See also Internal D0 Note 558 (1987) (unpublished).

[6] A.P. White, *Proceedings of the 8th Topical Workshop on Proton-Antiproton Collider Physics, Castiglione, Italy* (1989). See also Internal D0 Note 917 (1990) (unpublished).

[7] S. Wimpenny *et al.*, Nucl. Instr. and Methods **A279**, 107 (1989).

[8] C. Brown *et al.*, Nucl. Instr. and Methods **A279**, 331 (1989).

[9] A. Clark *et al.*, Nucl. Inst. and Methods **A279**, 243 (1989).

[10] D. Buchholz *et al.*, Nucl. Instr. and Methods **A257**, 556 (1987).

[11] S. Rajagopalan, *The dE/dx Capabilities of the D0 Tracking System*, Ph.D Thesis, Northwestern University, June 1992 (unpublished).

[12] P.Bhat,"TB 1990 Beamline Operation,Performance, and Studies", D0 Note 1076 Pt.1 (1991) (unpublished).

[13] M.Tartaglia,"1990 NW Beamline Performance", D0 Note 1076 Pt.3 (1991) (unpublished).

[14] H.Fenker,"A Standard Beam PWC for Fermilab", FNAL-TM-1179, Feb. 1983.

[15] M. DeMarteau *et al.*, private communication.

[16] R. Yarema, IEEE Trans. Nucl. Science NS-33, 933 (1986).

[17] D. Howard; B. Chase, Internal D0 Note 953 (unpublished).

[18] G. Saewert and B. Chase, Internal D0 Note 669 (unpublished).

[19] M.I. Martin, M.E. Johnson, M.J. Mayberry, and D.C. DeGroot, IEEE Trans. Nucl. Science NS-34, 258 (1987).

[20] B. Gobbi, private communication.

[21] D. Schaile *et al.*, "A Simultaneous Hit Finding and Timing Method for Pulse Shape Analysis of Drift Chamber Signals", Nucl. Instr. and Methods **A242**, 247-253 (1986).

[22] H. Bärwolff *et al.*, "Reconstruction of Double Hits from Drift Chamber FADC Pulses", Nucl. Instr. and Methods **A294**, 117-120 (1990).

[23] D.G. Cassel and H. Kowalski, "Pattern Recognition in Layered Track Chambers Using a Tree Algorithm", Nucl. Instr. and Methods **185**, 235-251 (1981).

[24] R.Avery *et al.*, "Performance of CD Detectors at NWA Test Beam", Internal D0 Note 1049 (1990) (unpublished).

[25] J. Va'vra, "High Resolution Drift Chambers", Nucl. Instr. and Methods **A244**, 391-415 (1986).

[26] J. Whitmore, "Experimental Results on Strong Interactions in the NAL Hydrogen Bubble Chambers", Phys. Rep. **C10**, 273-373 (1974).

[27] J. Whitmore, "Multiparticle Production in the Fermilab Bubble Chambers", Phys. Rep. **C27**, 187-273 (1976).

[28] C. DeMarzo *et al.*, "Multiparticle Production on Hydrogen, Argon, and Xenon Targets in a Stream Chamber by 200-GeV/c Proton and Antiproton Beams", Phys. Rev. **D26**, 1019-1035 (1982).

[29] F. Fumuro *et al.*, "A Dependence in Proton-Nucleus Interactions at $400\,GeV$", Nucl. Phys. **B152**, 376-389 (1979).

[30] A. Brenner *et al.*, "Experimental Study of Single-Particle Inclusive Hadron Scattering and Associated Multiplicities", Phys. Rev. **D26**, 1497-1553 (1982).

[31] G. Giacomelli, "Inclusive Charged and Neutral Particle Production in High Energy Hadron-Hadron Collisions", *Proc. 19th Int. Conf. High Energy Physics, Tokyo, 1978*, ed. S.Homma, M Kawaguchi, and H. Miyazawa (Phys. Soc. of Japan, Tokyo, 1979), 53-62.

[32] R. Adair, "Diffraction-Disassociation Model of Very-High-Energy Nucleon-Nucleon Interactions and the Diffusion of Cosmic Rays through the Atmosphere", Phys. Rev. **172**, 1370-1380 (1968).

[33] L. Bertocchi *et al.*, "Integral Equation for High-Energy Pion-Pion Scattering", Nuovo Cimento **25**, 626 (1962).

[34] A. Mueller, "Multiplicity Distributions in Regge-Pole-Dominated Inclusive Reactions", Phys. Rev. **D4**, 150-155 (1971).

[35] R. Hwa and C. Lam, "Flat Proton Spectrum and Its Implications", Phys. Rev. Lett. **27**, 1098-1101 (1971).

[36] J. Benecke *et al.*, "Hypothesis of Limiting Fragmentation in High-Energy Collisions", Phys. Rev. **188**, 2159-2169 (1969).

[37] E. Fermi, "High Energy Nuclear Events", Prog Theor Phys. **5**, 570-583 (1950).

[38] E. Berger *et al.*, "Correlations in High-Energy Production Processes", Phys. Rev. **D6**, 2580 (1972).

[39] R. Avery, private communication, to be published as a DØ Note.

[40] S. Azimov *et al.*, "Multiplicity of Charged Particles in π^--Carbon Interactions from 4 to 40 GeV/c", Nucl. Phys. **B107**, 45-64 (1976).

[41] J. Elias *et al.*, "Experimental Study of Multiparticle Production in Hadron-Nucleus Interactions at High-Energy", Phys. Rev. **D22**, 13-35 (1980).

[42] M. Faessler, "Inelastic Hadron-Nucleus Interactions at 20 and 37 GeV/c", Nucl. Phys. **B157**, 1-22 (1979).

[43] M. Perl, *High Energy Hadron Physics*, (John Wiley & Sons, New York, 1974), 24-51.

[44] R.J. Glauber, "High-Energy Collision Theory", in *Lectures in Theoretical Physics*, edited by W.E.Brittin and L.G.Dunham, (Interscience, New York, 1959), 315-414.

[45] A.S. Carroll *et al.*, "Absorption Cross Sections of $\pi^\pm$, $K^\pm$, p, and $\overline{p}$ on Nuclei Between 60 and 280 GeV", Phys. Lett. **80B**, 319-322 (1979).

[46] H.R. Blieden *et al.*, "Measurement of Small-Angle Elastic Scattering of Pions and Protons by Nuclei", Phys. Rev. **D11**, 14-28 (1975).

[47] G. Bellettini *et al.*, "Proton-Nuclei Cross Sections at 20 GeV", Nucl. Phys. **79**, 609-624 (1966).

[48] V.D. Apokin *et al.*, "Elastic Scattering of π^- Mesons and Protons by Nuclei in the Region of the Diffraction Peak at Momenta $30 - 50\,GeV$", Sov. J. Nucl. Phys. **25**, 297-299 (1977).

[49] A. Schiz *et al.*, "Hadron-Nucleus Elastic Scattering at 70, 125, and 175 GeV/c", Phys. Rev. **D21**, 3010-3022 (1980).

[50] J. Bantly, "Fast and Simple DØ Forward Drift Chamber Level 2 Trigger for High Multiplicity Events", Internal DØ Note 1418 (1992) (unpublished).